

Star Formation Histories of Early-Type Galaxies. I: Higher Order Balmer Lines as Age Indicators

Nelson Caldwell

Smithsonian Astrophysical Observatory, 60 Garden Street, Cambridge, MA 02138

and

James A. Rose and Kristi Dendy Concannon

Department of Physics and Astronomy, CB #3255, University of North Carolina, Chapel Hill, NC 27599

caldwell@cfa.harvard.edu, jim@physics.unc.edu, kdconcan@kings.edu

ABSTRACT

We have obtained blue integrated spectra of 175 nearby early-type galaxies, covering a wide range in galaxy velocity dispersion, and emphasizing those with $\sigma < 100$ km s⁻¹. Galaxies have been observed both in the Virgo cluster and in lower-density environments. The main goals are the evaluation of higher order Balmer lines as age indicators, and differences in stellar populations as a function of mass, environment and morphology. In this first paper our emphasis is on presenting the methods used to characterize the behavior of the Balmer lines through evolutionary population synthesis models. Lower- σ galaxies exhibit a substantially greater intrinsic scatter, in a variety of line strength indicators, than do higher- σ galaxies, with the large intrinsic scatter setting in below a σ of 100 km s⁻¹. Moreover, a greater contrast in scatter is present in the Balmer lines than in the lines of metal features. Evolutionary synthesis modeling of the observed spectral indices indicates that the strong Balmer lines found primarily among the low- σ galaxies are caused by young age, rather than by low metallicity. Thus we find a trend between the population age and the central velocity dispersion, such that low σ galaxies have younger luminosity-weighted mean ages. We have repeated this analysis using several different Balmer lines, and find consistent results from one spectral indicator to another.

Subject headings: galaxies:early-type—galaxies:abundances—galaxies:stellar content

1. INTRODUCTION

With the exception of galaxies within a few Mpc, efforts to determine the star formation and chemical enrichment histories of galaxies must be based on observations of their integrated

starlight, and of the modeling of that integrated spectrum. Unfortunately, establishing reliable luminosity-weighted mean ages and chemical compositions for early-type galaxies has been difficult to achieve, due primarily to the degeneracy between age and metallicity on the integrated spectra of galaxies (e.g., Worthey 1994), and, secondarily, to the non-solar abundance ratios in most early-type galaxies (e.g., O’Connell 1976, Worthey et al. 1992, Vazdekis et al. 1997, Trager et al. 2000a, Kuntschner et al. 2001). Nevertheless, recently improved population synthesis models and higher quality of spectra of galaxies have led to a surge of results in this field (Trager et al. 2000a,b, Kuntschner 2000, Kuntschner et al. 2001, Vazdekis et al. 2001, Terlevich & Forbes 2002, Proctor & Sansom 2002, Kuntschner et al. 2002).

The need for accurate information on galaxy ages and metallicities has been underscored by rapid developments in cosmological simulations of the evolution of structure in the universe. Large-scale numerical simulations of structure formation within the context of the Λ CDM (i.e., cold dark matter plus substantial contribution from a cosmological constant) scenario, when coupled with parametrized baryonic physics, now make clear predictions as to the formation histories of early-type galaxies as a function of mass and environment (Kauffmann 1996; Kauffmann & Charlot 1998; Somerville & Primack 1999; Benson et al. 2001). Hence a comprehensive database of mean ages and metallicities of early-type galaxies covering a range in mass and environment can provide crucial constraints on the hierarchical evolution scenario that is a key component of the Λ CDM picture.

We have recently completed a large database of integrated spectra of 175 early-type galaxies which serves two main objectives. The first goal is to observe early-type galaxies covering a large range in mass, environment, and early-type morphology. The hierarchical galaxy formation models now make predictions for the star formation and chemical enrichment histories of galaxies as a function of their mass and environment. In addition, there is an important distinction to be made between elliptical galaxies (those galaxies without apparent ongoing star formation and without a stellar disk) and lenticulars (S0s: those galaxies without apparent ongoing star formation, but which do have stellar disks). Whether these two types of galaxies have had similar origins and star formation histories, and whether there is a continuum of properties between them, is a subject of longstanding debate. A second goal is to investigate the blue spectral region, which covers the higher order Balmer lines, as a promising spectral region for obtaining better decoupling between age and metallicity effects.

There are two aspects in which our survey departs from previous work. The first is an emphasis on low-mass galaxies, as characterized by their low central velocity dispersion, σ . While previous surveys have tended to emphasize galaxies with $\sigma > 100 \text{ km s}^{-1}$, our survey contains a substantial emphasis on galaxies with lower σ . Second, we have obtained wavelength coverage down to $\lambda 3600 \text{ \AA}$, at the relatively high spectral resolution of 3.1 \AA FWHM , which allows us to evaluate the usefulness of higher order Balmer lines for age and metallicity determinations.

This paper is the first in a series that will evaluate the ages and chemical compositions of early-

type galaxies as a function of both mass and environment. In this paper the primary emphasis is on establishing the techniques that we use to extract luminosity-weighted mean ages and metallicities from the galaxy integrated spectra, particularly in regard to the higher order Balmer lines. We present an extensive comparison between ages derived from different Balmer line measurements, to test whether robust results are obtained from galaxy population synthesis. The main scientific results presented here relate to the dependence of the mean age and metallicity of early-type galaxies on the central velocity dispersion. We reserve more extensive discussions of the influence of environment and morphology for subsequent papers in the series. A brief description of the sample of galaxies and the observational data is given in §2, while a discussion of the spectral indices used in the study is given in §3. The techniques used to model the integrated spectra of galaxies are described in §4. In §5 we discuss the dependence of galaxy age and metallicity on velocity dispersion, and in §6 we evaluate the results obtained from different Balmer and metal features.

2. Observational Data

To fully investigate the star formation histories of early-type galaxies, we have chosen our sample to cover a range in mass, morphological classification, and environment. Our data sample consists of 175 early-type galaxies, 59 of which are in the Virgo cluster and 116 of which are in the field or other low-density environments. The galaxies cover a central velocity dispersion range of $50 < \sigma < 320$ km/s, with an emphasis on low- σ galaxies, and have been previously classified as either E, S0, dS0, or dE as indicated by their ground-based morphology. A more detailed discussion of the sample selection is given in Paper II, for the Virgo galaxies, and in Paper III, for the field sample.

Long slit spectra of all galaxies in the sample have been obtained at the F. L. Whipple Observatory (FLWO) with the 1.5m Tillinghast telescope, the FAST spectrograph and a Loral 512 x 2688 pixel CCD (Fabricant et al. 1998) during twelve observing runs between 1997 September and 2002 May in seeing conditions of 2" or better. The instrumental setup was identical on all but two occasions. The dispersing element is the 600 line/mm grating which produces a spectral coverage of $\sim 2000\text{\AA}$ from 3500 \AA to 5500 \AA at 0.75 \AA pixel⁻¹ dispersion. Using a 3" slit, four pixel resolution is typically achieved, hence the data have a spectral resolution of 3.1 \AA FWHM. On two of the observing runs, the above setup differed in that a 2" slit was used, resulting in a spectral resolution of 2.14 \AA FWHM. These observations have been smoothed to the same intrinsic resolution as the remainder of the data.

Spectra were extracted using a variance weighting scheme which included data along the slit down to 10% of the peak flux at a given wavelength. Thus the resultant spectra represent the global spectra and refer to an isophotal area, but with larger weight given to the brighter, central regions. Discussion of radial variations in the derived stellar populations will be taken up in Paper II. The data were then fluxed using standard stars observed during the same nights.

Radial velocities and velocity dispersions were determined for each galaxy, using the IRAF package FXCOR and K0III template stars. These are used to deredshift the spectra and to broaden them to a common resolution. The velocities and errors are listed in Table 1, where the errors are the internal errors produced by FXCOR, and averaged from the multiple observations. A comparison with the literature values of Smith et al. (2000) for 25 galaxies in common gives a mean difference of 13 km s^{-1} and rms of 58 km s^{-1} . Our measured velocity dispersions are in good accord with the literature values compiled by McElroy (1995). The dispersion errors contained in Table 1 are the rms errors among repeated observations, but with a lower limit of 7 km s^{-1} enforced.

For the low σ galaxies ($\sigma < 80 \text{ km s}^{-1}$), our values tend to be systematically higher by about 50% than the recent values determined by Simien & Prugniel (2002), Pedraz et al. (2002), and Geha et al. (2002). The discrepancy is due in general to our lower velocity resolution than the cited studies ($\sim 80 \text{ km s}^{-1}$ versus $\sim 25 \text{ km s}^{-1}$), and in certain specific cases because of our inclusion in the extracted spectra of outer parts of galaxies that are rotating, leading to broadened absorption lines. The cited works measured central broadenings, whereas we measured global broadenings. For most of our purpose, the discrepancy does not matter, since we smooth all spectra to a common velocity broadening of 230 km s^{-1} , and instrumental/observational effects below this value are of no concern. High resolution dispersions for all the smaller galaxies would be desirable for the study of relations between dispersions and our derived stellar population parameters, but are not yet available. Table 1 gives the log of the galaxy observations as well as basic derived parameters.

Although the galaxies were chosen to be free of emission contamination as based on the low S/N spectra of the CfA I redshift survey (Huchra et al. 1983), a significant fraction of the absorption line spectra were found to suffer from the effects of emission in the Balmer lines. The contamination is not completely unexpected since previous surveys have shown that 40-50% of E/S0 galaxies have at least small amounts of ionized gas (Caldwell 1984; Phillips et al. 1986), but we do need to correct for this emission. To determine the quantitative impact of the fill-in on the spectral line strengths, we obtained spectra in the red, centered near $H\alpha$, for 40% of the galaxies in the sample (24 Virgo, 45 Field). The red spectra were taken during observing runs in 2000 February-April and 2000 September-October using a similar setup as the blue spectra, with a $3''$ slit, covering a spectral range of $5500\text{--}7500\text{\AA}$ and overlapping the blue spectra by $\sim 50\text{\AA}$. Typically, 1-2 exposures, each 700-1200 sec in duration, were taken for each galaxy. The red spectra were reduced in the same manner as the blue spectra.

The galaxies observed in the red are so indicated in column 9 of Table 1 and were chosen from two subsets of our original data – (i) those galaxies with suspected emission at $[OII] \lambda 3727$ and (ii) those galaxies whose spectra appear to be emission-free. An emission-free spectrum can be normalized and subtracted from an emission-contaminated spectrum to yield the flux in $H\alpha$ and in the neighboring $[NII]$ lines. The $H\alpha$ information that is gained from the red spectrum can then be used to correct the bluer Balmer line indices employed in the age-dating analysis. A discussion of the method used to correct for emission contamination is given in Appendix A.

3. Spectral Indices

In studying the integrated light of galaxies, our goal is to determine the distribution in age and chemical composition of the stellar populations present. Given that each population of a given age and metallicity itself is a composite of stars covering a wide range in the HR diagram, the interpretation of integrated spectra has been plagued by problems of non-uniqueness. In addressing this, observers have naturally been driven in two conflicting directions. One is to observe the entire spectral energy distribution, hence at low resolution and with a wide slit, to best sample the contributions from all types of stars. The other is to work at higher spectral resolution and a narrow slit, to measure the strengths of specific absorption features which, by having primary sensitivity to one particular atmospheric parameter (e.g., T_{eff}), can help solve the non-uniqueness problem. Both methods supply important constraints to the analysis of integrated light. In what follows we exclusively rely on higher resolution spectroscopy, with emphasis on specific spectral features relevant to resolving non-uniqueness issues.

3.1. Index Definitions

In measuring the strengths of specific absorption features there is again a tradeoff between low and high resolution approaches. To obtain a robust result for the equivalent width of an absorption line requires a determination of the continuum at a sufficient distance from the line center so that the wings of the feature are excluded, while the measurement of the feature itself must include both the line core and wings. Such an approach forms the basis of the Lick index system (e.g., Faber et al. (1985) and described in detail in Worthey et al. (1994)), in which indices are defined by measuring the flux in the line bandpass and subtracting it from a continuum formed by connecting a straight line between the average flux in red and blue sidebands. While the traditional Lick indices primarily concentrate on prominent metal features in the red and on $H\beta$ (see Worthey et al. (1994) for a complete list), several new Lick-style indices were defined in Worthey & Ottaviani (1997) which concentrate on the higher order Balmer lines of $H\gamma$ and $H\delta$.

The disadvantage of the relatively broad bandpass system is the contamination of both the line and continuum bandpasses with unwanted features which can complicate the interpretation of the resultant spectral index. Hence an alternative approach is to narrow both line and continuum bandpasses sufficiently to obtain the cleanest possible measurements of both line and (pseudo)-continuum. This approach has been utilized in Rose (1994) and Jones & Worthey (1995) in defining indices that are narrowly focussed on, e.g., $H\gamma$ or the Fe I $\lambda 4045$ iron feature. While minimizing the contribution from unwanted features, this method has two disadvantages. First, by narrowing the line measurement, only the core is included, hence the method loses sensitivity if significant wings are present. Moreover, a decrease in spectral resolution, due to instrumental or velocity broadening effects, will redistribute the flux deficit in the line core out into the wings, where the pseudocontinuum “sidebands” are defined. The result is that slight changes in spectral

resolution can lead to large changes in the measured strength of the line feature, thereby making it critical to determine and account for this spectral resolution effect. More recently, Vazdekis & Arimoto (1999) and Vazdekis et al. (2001a,b) have addressed this problem in the case of a narrow band $H\gamma$ index in which the location of the line and pseudocontinuum bandpasses have been carefully selected so as to minimize the effect of spectral resolution on the index measurement. The result is a more robust definition of $H\gamma$, but which also requires high precision in the wavelength scale so as to measure the correct line and continuum intervals.

A third approach to the problem, originally formulated in Rose (1984), and used subsequently in, e.g., Rose (1985) and Rose (1994), is to maximize the contribution from the feature of interest by measuring the residual central intensity in the line, and that in a neighboring reference line, and forming the ratio of these two quantities. By using the deepest part of the spectral lines in the two features, the maximum contrast with other contaminating absorption lines is achieved. In addition, the line ratio index is defined without reference to the (pseudo)-continuum level, which is generally problematic to locate, especially at bluer wavelengths where line crowding is such a problem. Moreover, since both line centers tend to be similarly affected by a change in spectral resolution, the line ratio indices are not strongly sensitive to resolution effects. A disadvantage to this method is that the index loses sensitivity if one of the lines saturates in the core, a problem that is a particular issue in younger populations, where the Balmer lines become strong. A further problem is that the indices all consist of relative measurements of one feature against another, and thus cannot provide the equivalent width measurement of a single feature that is ideal for resolving the degeneracy between age and metallicity effects.

In this paper we utilize the well-studied Lick index system for the red spectral region, in particular for characterizing the strength of $H\beta$. Although we use the standard Lick index definitions (Worthey et al. 1994), our index measurements *have not been calibrated to the Lick/IDS system*, since that would require further smoothing of our data as well as transformation onto the Lick/IDS instrumental response system. For the higher order Balmer lines in the blue, where the line crowding is more extreme, we switch primarily to the line ratio indices of Rose (1994). In particular, we make extensive use of the Hn/Fe index¹ which has the advantage of averaging three higher-order Balmer line to nearby iron line ratios, and which was first shown to be an effective age indicator in Concannon, Rose, & Caldwell (2000). Altogether, we measure a total of 30 spectral indices – 15 Lick equivalent width indices, 3 high-resolution equivalent width indices, and 12 line ratio indices. We do not utilize the Vazdekis et al. (2001a) $H\gamma_{\sigma < 130}$ index in this paper, due to the high velocity dispersion of many of the galaxies in our sample, but reserve it for a future paper, in which we examine the low velocity dispersion Virgo galaxies.

To readily compare the observed galaxy spectral indices with those produced by the evolutionary synthesis models, we broadened all of the galaxy spectra to a common effective velocity dispersion of 230 km s^{-1} . Consequently, we have excised from the discussion in this paper all

¹ $Hn/Fe = < H\delta/Fe4045 + H\gamma/Fe4325 + H8/Fe3859 >$

galaxies with $\sigma > 230 \text{ km s}^{-1}$ and leave them for a future discussion. This somewhat arbitrary cutoff was arrived at as a compromise between desiring to preserve as much dynamic range as possible in the blue indices while also including as many galaxies as possible in the discussion. The removal of the high σ galaxies reduces our sample to 56 Virgo galaxies and 97 field galaxies.

3.2. Errors in the Spectral Indices

The spectral indices discussed above are all measured with a single, convenient FORTRAN program written by Alexandre Vazdekis and publicly available on his website². To determine the uncertainties in each spectral index, we use a weighted combination of the rms in the individual galaxy measurements as outlined in Paper I; a brief review of the process is given here. First, the spectral index is measured for each of the individual galaxy exposures, typically 2-4 for each object, and the standard deviation of these values is determined. Since the rms among individual exposures is particularly unreliable for those galaxies which have only two observations, we utilize the standard deviations in all indices for all galaxies in the following manner. For a particular galaxy, i , the error Λ_{ij} in index j , where there are a total of m indices and n galaxies, is given by:

$$\Lambda_{ij} = \frac{\sum_{i=1}^n \varepsilon_{ij} \sum_{j=1}^m \varepsilon_{ij}}{\sum_{i,j=1}^{m,n} \varepsilon_{ij}} \quad (1)$$

where $\sum_{i=1}^n \varepsilon_{ij}$ is the average over all galaxies of the standard deviation in the j^{th} index, $\sum_{j=1}^m \varepsilon_{ij}$ is the average of the standard deviations of all indices of the same type (i.e., all Lick indices or all line ratios indices) for the i^{th} galaxy, and $\sum_{i,j=1}^{m,n} \varepsilon_{ij}$ is the average standard deviation in all indices of the same type for all galaxies in the sample. Thus, in effect, by using all of the spectral index error information, we have found the average error for each index, and weighted those errors by the relative mean error in all indices for a particular galaxy compared to the mean error over the whole sample. For the two galaxies in our sample for which we have only one observation, the above process is still followed, except that the standard deviation in each index is taken to be the mean rms in that index for galaxies with comparable signal-to-noise ratios.

3.3. Correcting for Emission Contamination

Early-type galaxies normally contain much less ionized gas and dust than spiral galaxies. However, spectroscopic surveys have revealed that nearly 40-50% of ellipticals do have at least some weak optical emission (Caldwell 1984; Phillips et al. 1986). If emission lines *are* present in

²<http://www.iac.es/galeria/vazdekis/models.html>

the galaxy spectrum – from either ionized gas in HII regions, active galactic nuclei (AGN) and/or planetary nebulae – the measured absorption line indices may be severely affected. In the case of the Balmer lines, emission fill-in can weaken the line strength and lead to older derived ages. Thus, a potential source of systematic error in the measurement of the spectral line indices comes from the contamination of the absorption feature by fill-in from emission lines. The method that we follow to detect and remove contamination of the absorption features from superimposed emission is discussed in Appendix A.

3.4. Compilation of Spectral Index Data

In Table 2 we list all of the spectral indices measured by us for each galaxy. In the first column the spectral index is given, and in the second column a reference is given to the paper in which the index is defined. The full table of spectral indices, and the errors in those indices, is listed electronically in Table 3. To clarify matters, in the third column of Table 2 we list the column number in Table 3 in which a particular index appears. Each index in Table 3 is followed by its $\pm 1\sigma$ error. Many of the indices in Table 3 have been corrected for emission contamination (in the Balmer lines) and/or for the effects of non-solar abundance ratios (see §4.5). As a guide to the amount of correction that has been applied, in the second to last column in Table 3 we give the correction that has been made to the Lick $H\beta$ index for emission fill-in, and in the last column we give the correction applied to the $H\beta$ index to account for non-solar abundance ratios.

4. Evolutionary Synthesis Models

The information extracted from the spectral indices defined in the previous Section must still be translated into mean ages and metallicities of the integrated stellar population through the use of population synthesis models. In these models, a theoretical stellar evolutionary isochrone is computed for a given population representing a unique age and metallicity, hereafter referred to as a simple stellar population (SSP). Each point along the isochrone represents a specific star of known temperature, luminosity and surface gravity which produces a specific set of absorption lines. The spectral line strengths for each point along the isochrone are weighted by the stellar luminosity and the number of stars expected at that point (from the computed luminosity function) and then added to derive the total line strength for the integrated population. By computing the expected integrated line strength for SSPs covering a range of ages and metallicities, the spectral indices from the galaxies can be compared to the predicted values, and, the luminosity-weighted mean age and metallicity of the galaxy can be determined.

While the sophistication of the evolutionary population synthesis models that supply the framework for interpreting the integrated light of galaxies has increased substantially in the last few years, the current generation of models still has its uncertainties. There are a variety of issues including:

uncertainties in the model isochrones (with inadequate understanding of convection and of mass loss being the chief culprits), uncertainties in transforming from the theoretical H-R diagram into an observational plane (with the T_{eff} scale providing a major problem), inadequate coverage in empirical stellar libraries, uncertainties in the accuracy of model stellar atmospheres and synthetic spectra, and uncertainties in the treatment of non-solar abundance ratios. Additionally, the population models assume a single age and metallicity for the entire galaxy stellar population while a galaxy is most likely a composite of different populations. As a result of the uncertainties in the models, we place primary emphasis on using the models to determine the *relative* ages of galaxies, rather than their *absolute* ages. In the present section, the components and implementation of the population models are described, followed by a comparison of the models used in this work to other available synthesis models.

4.1. The Worthey Population Models

For our analysis, we use a modified version of the population synthesis models originally introduced in Worthey (1994). The Worthey (1994, hereafter W94) models depend on two adjustable parameters – the metallicity and single-burst age of the stellar population – and one fixed parameter, the IMF exponent, here chosen to be the Salpeter value. The basic ideas behind the models are reviewed briefly, and the reader is referred to W94 for more details.

To assemble the theoretical integrated spectrum, the models incorporate three ingredients: stellar evolutionary isochrones, a stellar SED library, and a library of absorption line strengths. For the evolutionary information, the modified W94 models use the isochrones of the Padova group (Bertelli et al. 1994) which have been computed for six metallicities in the range $-1.7 < [Z/H] < +0.4$ and for 29 ages from 0.004 to 19 Gyr. The stellar SED library was constructed using the model atmospheres and synthetic spectra of Kurucz (1993, 1994) for stars hotter than 3750K and the model SEDs of Bessell et al. (1989, 1991) and observed SEDs from Gunn & Stryker (1983) for cooler M giants. Ideally, the spectral line strengths should be determined from a single observed library of stellar spectra which fully sample the entire range of atmospheric parameters (T_{eff} , $\log g$, and $[Z/H]$). Since the Galactic star formation and chemical enrichment history excludes some regions of the atmospheric parameter space, especially metal-poor high-gravity stars, we have chosen to combine libraries of both empirical and synthetic spectra to fully cover the line strengths along each isochrone.

4.1.1. The Empirical Stellar Library

For the empirical spectral library, we use a set of high-resolution stellar spectra compiled by L. Jones (1999; see also Leitherer et al. 1996), which are well-suited for stellar population analysis. The library consists of two spectral regions — one in the blue covering the wavelength range $\lambda 3820\text{--}4509\text{\AA}$

and one in the red covering $\lambda 4780\text{--}5469\text{\AA}$ — for each of 684 stars. The spectra³ were taken with the KPNO Coudé Feed telescope and spectrograph and have a pixel sampling of $0.62\text{\AA pixel}^{-1}$ with a spectral resolution of 1.8\AA FWHM . Because the stellar library is primarily drawn from the local solar neighborhood, all areas of the $\log g\text{--}[\text{Fe}/\text{H}]\text{--}\log T_{eff}$ grid are not equally covered. Specifically, the grid is relatively well-populated for cool stars ($T_{eff} < 6000$), but at higher temperatures, it has a much more limited coverage due to the lack of hot, metal-poor and hot, low-gravity stars. To ensure adequate sampling throughout the parameter space, we restrict our use of the empirical library to stars in the temperature range $3750\text{--}6300\text{K}$. Further stars were eliminated from the library if they are observed to have chromospheric emission (which contaminates the absorption line indices) or if their atmospheric parameters are either undetermined or are in striking disagreement with their measured spectral indices. In all, 547 stars are used from the empirical library.

The empirical spectral library is incorporated into the population synthesis models through polynomial fitting functions which describe how the absorption line strength varies as a function of the effective temperature, gravity and metallicity of the stars. To produce the fitting functions, we employed a FORTRAN program kindly provided by G. Worthey. The program uses a series of least-squares regressions to fit a third order polynomial in $\Theta=5040/T_{eff}$, $[\text{Fe}/\text{H}]$, and $\log g$. Through an iterative procedure, the terms in the polynomials are either included or excluded until no systematic trends appear in the residuals of atmospheric parameters versus the fit. Stars with very deviant index values are excluded from the fits, unless they are in regions of particularly poor coverage (e.g., very low metallicity). Each absorption line used in the spectral indices is fitted with one polynomial across the entire temperature range, $3500\text{--}6300\text{K}$.

4.1.2. *The Synthetic Spectral Library*

Due to the lack of hot, unevolved metal-poor stars in the Galaxy, the Coudé Feed spectral library (CFSL) only has adequate metallicity coverage for temperatures less than 7000K . To compensate for this shortcoming in the Coudé Feed library, the empirical spectra are augmented with 2103 synthetic spectra generated with the R. Kurucz SYNTH program using the Kurucz ATLAS model atmospheres (Kurucz 1993, 1994), both kindly provided by R. Kurucz. A complete description of the construction of the synthetic spectra is given in Leonardi & Rose (2002). Briefly stated, the SYNTH program generates a synthetic spectrum at high resolution (0.1\AA pix^{-1}) from a given model atmosphere and line list. The SYNTH spectrum is then rebinned and smoothed to match that of the observations. The synthetic library covers the wavelength range $\lambda 3500\text{--}5500\text{\AA}$ and covers the 3-dimensional parameter space of $\log g$, $[\text{Fe}/\text{H}]$ and T_{eff} (see Table 4 of Leonardi & Rose (2002) for the specific coverage). Because the synthetic spectra are subject neither to observational errors nor to uncertainties in the atmospheric parameters, the calculated line strengths

³The complete Coudé Feed spectral library is publicly available from the NOAO ftp archive at <ftp://ftp.noao.edu/catalogs/coudelib/>.

of the SYNTHE stars evolve systematically with the atmospheric parameters, and there is no need to fit them with polynomial functions. Instead, the synthetic spectra are incorporated into the population synthesis models through linear interpolation between the grid points for a given set of atmospheric parameters. For points outside the SYNTHE parameter grid, the line strength corresponding to the nearest grid point is used.

It is, of course, important that there be no strong discontinuity in line strength across the 6000K boundary in temperature between the empirical cool star spectra and the synthetic hot star spectra. The agreement between the empirical and the synthetic data is in general reasonably good in the region of overlapping temperature. We plot an example of the interface between synthetic and empirical spectra for the $H\delta$ feature in Figure 1.

4.2. Putting It All Together

Before using the population models to interpret the integrated light of the galaxies, it is important to ensure that all of the model ingredients are smoothed to the same spectral broadening as the galaxy data. The spectra in the Coudé Feed library were observed at an intrinsic spectral resolution of $\sim 1.8 \text{ \AA}$ FWHM whereas the FLWO galaxy spectra are at a resolution of $\sim 3.1 \text{ \AA}$. To put the two datasets on the same scale, the Coudé spectra are convolved with a Gaussian of $\sigma = 0.97 \text{ \AA}$. To determine the amount of broadening required to match the SYNTHE and FLWO spectra, a synthetic spectrum was chosen with the appropriate atmospheric parameters of a star observed with the same configuration as the galaxy spectra. The SYNTHE spectrum was then broadened by various Gaussians ranging from 0.2 to 6.0 pixels, each of the broadened spectra were cross-correlated with the original spectrum, and the relationship between the FWHM of the cross-correlation peak and the amount of smoothing was determined. Using this relationship, the amount of broadening required to match the SYNTHE spectra with the FLWO spectra was found to be $\sigma = 0.24 \text{ \AA}$. After both stellar libraries were smoothed to the same intrinsic spectral resolution as the galaxy data, they were then smoothed by an additional amount to match the effective galaxy broadening of 230 km s^{-1} (recall that all final galaxy spectra are broadened to a common velocity dispersion of 230 km s^{-1}). At this point, both the empirical and synthetic libraries and the galaxy data are all at a common spectral resolution.

Upon implementation, the population synthesis models combine the information from the Padova isochrones, the Kurucz SED fluxes and the library line strengths to create a theoretical integrated population of a specified age and metallicity. To assemble the integrated spectrum, the absorption line strengths are weighted by the number and luminosity of stars at that isochrone point and are superposed on the continuum that has been formed by the appropriate weighting of each SED. As the models integrate along the distribution of stars, the line strengths for isochrone points cooler than 6000K are calculated from the empirical fitting functions (where the Coudé Feed library coverage is complete) and from interpolating in the SYNTHE line strength grid for stars hotter than 6000K.

4.3. Comparison with Other Models

The ultimate results of the W94 population models are integrated absorption line strengths, which can be translated into the various spectral indices described in §3. For each spectral index we calculate a grid of model values at a series of ages and metallicities. By choosing an appropriate pair of indices, the galaxy data can be over-plotted on the index-index model grids, and the age and metallicity of the stellar population can be determined. Since the derived ages depend on the model grids against which they are measured, an important gauge is to compare the index-index grids produced by different synthesis models. Thus, as a check of our implementation of the W94 models, and hence our interpretation of the early-type galaxy spectra, we compare our model grids to those produced by the publicly available⁴ population synthesis models of A. Vazdekis (Vazdekis 1999, V99). The Vazdekis models are similar to the updated W94 models in that they both use the set of evolutionary isochrones produced by the Padova group (e.g, Bertelli et al. 1994), although the V99 models supplement these isochrones with the stellar tracks of Pols et al. (1995) for low mass stars ($M < 0.6 M_{\odot}$). Both models make use of the CFSL in constructing the integrated stellar population. However, an important difference in the two models is the method in which the stellar spectra are utilized in the computation of the integrated line strengths. As described in the previous section, the W94 line strengths are formed by interpolation in the synthetic spectral grid for hot stars, and through the use of empirical fitting functions for the cooler CFSL stars ($T_{eff} < 6000\text{K}$). The V99 models, on the other hand, rely solely on the CFSL (with slightly modified stellar parameters), and for each point in the H-R diagram choose a CFSL stellar spectrum with closely matching atmospheric parameters.

Figure 3 shows a comparison of the two sets of models for four different spectral index pairs that are used extensively in this paper. M32 is once again shown alone in all the plots as a visual aid. For clarity, we plot only a limited number of discrete ages, and only the two chemical compositions $[\text{Fe}/\text{H}] = 0.0$ and $[\text{Fe}/\text{H}] = -0.4$. Figure 3 indicates that there is good agreement between the predictions of the W94 models and the V99 models in the $\text{H}\beta$ versus Fe 4383 diagram. Agreement is satisfactory, as well, in the Hn/Fe versus Fe 4383 diagram. For the Mg b versus $\text{H}\beta$ and the Mg b versus Hn/Fe plots, however, the agreement is less satisfactory. The discrepancies highlight the problems inherent in determining the absolute mean ages of the galaxies. On the other hand, the *relative* ages of the galaxies, which are the primary concern of this paper, are less vulnerable to modeling issues. A more detailed comparison of the two models has been carried out by Kuntschner (2000) and Terlevich & Forbes (2002).

⁴<http://www.iac.es/galeria/vazdekis/models.html>

4.4. Determining Galaxy Ages and Metallicities

The goal of the population synthesis modeling is to compare the grid of computed model indices to those of our galaxy sample, and thereby to derive ages and metallicities of the galaxies in our data set. To do so, a primarily metallicity sensitive index (e.g., Fe5270) is plotted against a primarily age sensitive index (e.g., $H\beta$) for a range of SSP model predictions producing a largely orthogonal grid of ages and metallicities. By over-plotting the galaxy data, the SSP equivalent age and metallicity can be determined (Figure 2) through interpolation in the index grid. However, because the age-metallicity degeneracy is not completely broken, the lines of the model grids are not perpendicular. This fact complicates the reliable extraction of age and metallicity information when observational errors are included. An additional complication in deriving the galaxy ages and metallicities is that, as seen in Figure 2, not all galaxies lie within the model predictions. This may be due to observational errors, residual emission contamination in the Balmer line indices (see §3.3), differing abundance ratios in the galaxies and the model components (addressed in §4.5), and/or zero-point offsets in the population models.

To extract the age and metallicity of a galaxy from a particular index-index diagram, the four model grid points which form a box encompassing the data point are found. Using the four corners of the surrounding box, the lines of constant age and metallicity which pass through the data point are determined, and the age and metallicity values are interpolated along the constant metallicity and age lines. For galaxies which lie outside the model grids, the population values are extrapolated only in the cases where the extrapolation is small and reliable. Because the metallicity tracks tend to be evenly spaced, extrapolation of the galaxy metallicity is relatively stable. On the other hand, the constant age tracks are not evenly spaced and are, in fact, packed closer together for older ages. This makes a linear extrapolation of the galaxy age uncertain for data points which lie far from the model grids, particularly at old ages. Thus we do not attempt an age extrapolation for those galaxies which lie beyond the oldest age line in the diagram.

4.5. Non-Solar Abundance Ratios

In the previous section we have seen how spectral line-strength indices and population synthesis models can be used to circumvent the age-metallicity degeneracy, allowing us to derive the SSP age and metallicity for a galaxy. However, there is an additional complication to consider in making these determinations. Since the late 1970s, evidence has mounted that the abundance ratios in early-type galaxies are often non-solar and that the Mg/Fe abundance ratio, in particular, is larger in more luminous early-type galaxies than in solar-neighborhood stars (O’Connell 1976, Peletier 1989; Worthey, Faber & Gonzalez 1992; Vazdekis et al 1997). The population synthesis models are built using spectral databases of Solar Neighborhood stars, which reflect the specific pattern of the chemical enrichment of our Galaxy. In addition, the theoretical isochrones that are used as the backbone of evolutionary synthesis modeling are based on solar abundance ratios. Hence for

galaxies with elemental abundance ratios deviating from that found in the Solar Neighborhood, there are additional corrections to be made in modeling their luminosity-weighted mean ages and chemical compositions. Recent population synthesis modeling is now beginning to simulate the effect of non-solar abundance ratios (NSAR) (Trager et al. 2000a; Kuntschner et al. 2001; Vazdekis et al. 2001a; Proctor & Sansom 2002), based on theoretical isochrones incorporating non-solar abundance ratios (Salaris & Weiss 1998; Vandenberg et al. 2000; Salasnich et al. 2000) and on the synthetic spectral modeling of key spectral indicators carried out by Tripicco & Bell (1995). In Appendix B we describe how the effects of NSAR are accounted for, following the prescriptions developed by Trager et al. (2000a) and Kuntschner et al. (2001).

5. Results on Ages of Early-Type Galaxies

We are now in a position to combine the galaxy spectral index data, described in §3, with the modeling procedures, described in §4, to determine luminosity-weighted mean ages and metallicities for our early-type galaxy sample. There will be two main goals for the discussion in this Section and in §6. First, in this Section we demonstrate that there is a trend in the mean ages of early-type galaxies with velocity dispersion, in the sense that low- σ galaxies have younger mean ages than their higher- σ (i.e., more massive) counterparts. In establishing this result we will evaluate several potential sources of systematic error in age determinations, namely, “contamination” from a metal-poor population and/or from a red horizontal branch (RHB) population, “contamination” from emission lines, and the effect of non-solar abundance ratios. The second goal, discussed in §6, is to compare results obtained from different Balmer and metal line indicators, and to evaluate whether robust and consistent ages and abundances emerge when different diagnostic spectral features are employed.

5.1. Spectral Variations as a Function of Velocity Dispersion

We begin by illustrating the large range in spectral behavior that is evident in our galaxy sample. In Fig. 4, we plot representative examples of low- σ and high- σ galaxies, concentrating on the spectral region containing H δ at 4101 Å and H γ at 4340 Å, as well as H8 at 3888 Å. These spectra are shown at their observed spectral broadenings. From their appearance, it is clear that the low σ galaxies have a much wider range in Balmer line strength, and that the increase in Balmer line strength in the galaxies from top to bottom in the figure is systematic across all Balmer lines.

Hereinafter, the data we discuss, either in the form of spectra or indices, have been smoothed to a common velocity dispersion of 230 km s^{-1} , emission corrected (see appendix A), and corrected for NSAR where applicable (see appendix B). A quantitative representation of the variation in line strength among our early-type galaxy spectra is given in Fig. 5, where the behavior of four spectral indicators as a function of galaxy velocity dispersion is plotted. The two right hand panels

characterize the behavior of the metal features Mg *b* and Fe5270 from the Lick system. The upper and lower left hand panels plot the behavior of the Balmer-sensitive indices $H\beta$ and Hn/Fe . Note that for the two Balmer line strength indices the Balmer strength is plotted so as to increase from top to bottom. As defined in §3, the Hn/Fe index is an average value for the line ratios of $H\gamma$, $H\delta$, and $H8$ (at 3888 Å) to neighboring metal lines. Plotted with the galaxy data in Fig. 5 are the regression line fits to the indices as a function of $\log \sigma$. The fits were determined using the BCES (bivariate correlated errors and intrinsic scatter) method of Akritas & Bershady (1996) for the higher σ galaxies (with $\log \sigma > 2.0$, the outliers were excluded from the fit), and then extrapolated to lower σ . The application of the BCES method is further described in Concannon, Rose, & Caldwell (2000).

There are two key features to note in Fig. 5. First, while the metal-sensitive Mg *b* and Fe 5270 indices exhibit a relatively constant and symmetric scatter at all velocity dispersions, the two Balmer line indices show a striking increase in scatter for $\log \sigma < 2$. Second, the large scatter at low $\log \sigma$ is asymmetric, with many galaxies having high Balmer line strengths. As is previously described in Concannon, Rose, & Caldwell (2000), we have extracted the *intrinsic* scatter in the indices from the *observed* scatter, and the intrinsic scatter at high and low $\log \sigma$ is denoted by the two vertical arrows in the lower right corner of each plot. The results of the intrinsic scatter measurements are summarized in Table 4. There we have divided the galaxy sample into low- and high- σ bins. For each index we give the derived intrinsic scatter in the index as well as the $\pm 1\sigma$ uncertainty in the intrinsic scatter, first for the uncorrected indices, then for emission-corrected indices, and finally for indices corrected both for emission and for NSAR. The number in parentheses below the uncorrected value represents the median observational error for the index. Since different indices are measured in different ways, the ratio in intrinsic scatter between low- and high- σ samples provides the clearest assessment of the dependence of spectral index behavior on velocity dispersion. While that ratio is only 1.8 and 2.0 for Mg *b* and Fe5270, respectively, in the final (i.e., emission-corrected and NSAR-corrected) indices, it is 2.8 and 4.0 for $H\beta$ and Hn/Fe , thus underscoring that the large intrinsic scatter in low- σ galaxies is more pronounced in the Balmer lines. While the scatter in indices at low σ is large, a clearly measurable intrinsic scatter is also evident at high σ . We return to this fact in §6.3.

We have recalculated the statistics using the lower velocity dispersions from the literature, where available (§2.), and found no significant change. Perhaps when all of these lower mass galaxies have precise dispersions measured some of the details of the scatter calculations may change, but the main results that the scatter is due to age variations will likely not change. Concannon, Rose, & Caldwell (2000) proposed that the large intrinsic scatter in the Balmer lines is due primarily to a range in age that is particularly pronounced among the lower σ galaxies. With the population synthesis models and technique established in the previous sections, we now evaluate that assertion.

5.2. Variations in Age as a Function of Velocity Dispersion

The distribution of galaxies in luminosity-weighted mean age and metallicity can be assessed by plotting the combination of a primarily age-sensitive Balmer index versus a primarily metal-sensitive index. To begin, we plot the metal-sensitive Fe4383 index from the Lick system versus the Balmer-sensitive H α /Fe index in Fig. 6. The galaxy data have been corrected for emission, and have been subdivided into four different velocity dispersion bins. The data are superposed on grid lines of SSPs of constant age and metallicity as determined from the Worthey models described in §4. For comparison with more familiar plots of this kind, Fig. 6 is similar in nature to the log H β versus log \langle Fe \rangle plot in, e.g., Figure 1(b) of Trager et al. (2000b), except that here the Balmer index is on the x-axis. A striking feature of Fig. 6 is that the two groups with low σ have a lower mean age than does the highest σ group ($\log \sigma \geq 2.2$), while the galaxies with $2.0 < \log \sigma < 2.2$ show an intermediate distribution in age. In short, the increased scatter in H α /Fe seen among the low σ galaxies (in Fig. 6) is indeed reflected in an increased trend towards younger ages. In Table 5 we summarize data on the mean age, and dispersion in age, for each of the four log σ groups. The age dispersions listed there have not been corrected for observational error. Note that the rms scatter in age is actually *lower* among the low σ galaxies than for the high σ galaxies, which may seem surprising, given the greatly *increased* rms scatter in Balmer line strength for the low σ galaxies. This result simply reflects the highly non-linear dependence of Balmer line strength on age, coupled with the pronounced trend to younger mean ages among the low σ galaxies.

Another important aspect of Fig. 6 is the fact that 47 Tuc lies separated from virtually all galaxies in the diagram. Clearly, no galaxy in our sample is similar to 47 Tuc, which supplies a well-defined empirical anchor point at an age of ~ 12 -13 Gyr (Liu & Chaboyer 2000; Zoccali et al. 2001; Grundahl, Stetson, & Andersen 2002) and $[\text{Fe}/\text{H}] \sim -0.7$ - -0.8 ((Brown & Wallerstein 1992; Carretta & Gratton 1997)). The large discrepancy between isochrone-based SSP models and the location of 47 Tuc has been pointed out in previous work (Gibson et al. 1999). Through a combination of the inclusion of α -element enhancement and diffusion to the models (Vazdekis et al. 2001a), along with adjustments to the T_{eff} scale for metal-poor giants and, most importantly, to the failure of model isochrones to produce sufficient numbers of stars above the HB level (Schiavon et al. 2002a,b), the most recent models now reproduce the position of 47 Tuc in many diagnostic diagrams. However, the key point is that, independent of zero-point problems with the models, no galaxies are found with the old age and low metallicity of 47 Tuc. Despite the fact that 47 Tuc shares the same B-V color as a typical E/S0 galaxy (e.g., M32) their mean ages and chemical compositions are quite distinct. The systematic differences in absorption line indices between 47 Tuc and M32 have been previously analyzed by Rose (1994) and Rose & Deng (1999).

While the mean age and the scatter in age vary substantially with velocity dispersion, there is, on the other hand, relatively little change in metallicity, as designated by the iron-sensitive Fe5270 feature. It is also worthy of note that M32 (designated by the large square) is found among the highest $[\text{Fe}/\text{H}]$ objects in the sample. One should bear in mind that in M32 we are sampling only the central ~ 10 pc of the galaxy, thus it is not clear how relevant the comparison is with the more

widespread central region spectra of the other galaxies in the sample.

To quantify the appearance of different mean ages for the four $\log \sigma$ groups in Fig. 6, we have applied the Kolmogorov-Smirnoff two-sample test to various combinations of the four $\log \sigma$ bins. The results are summarized in Table 6. The two discrepant data points in the $2.0 < \log \sigma < 2.2$ group have been excluded from the test. With the one exception of the two lowest σ groups, the likelihood that the age distributions of any two $\log \sigma$ groups are drawn from the same parent population is small. In the case of the two lowest σ bins, the probability is high that their age distributions are similar.

To further emphasize that the intrinsic scatter in Balmer line strength found in Fig. 5, especially at low $\log \sigma$, is primarily due to a spread to younger ages, we have replotted the correlation between Hn/Fe and $\log \sigma$ and that between $\text{Mg } b$ and $\log \sigma$ in Figs. 7 and 8, respectively. In the left hand panels we have subdivided the galaxies into different age bins, where the ages come directly from interpolating each galaxy data point between the age-metallicity grid lines in the Fe4383 versus Hn/Fe diagram (Fig. 6). The right hand panels show the galaxies coded by metallicity, where the $[\text{Fe/H}]$ values also come from interpolation in Fig. 6. It is certainly evident from Fig. 7 that the low σ galaxies with strong Balmer lines (low Hn/Fe) have young ages as well. In contrast, there is no clear trend with metallicity. In the case of the $\text{Mg } b$ index, plotted in Fig. 8, a trend still exists in the sense that at a given $\log \sigma$, a lower $\text{Mg } b$ correlates with lower age. However, the effect is now subtler for this metallicity feature than for the more age-sensitive Balmer index. Although we do not show them here, similar results are found for plots of both $\text{H}\beta$ and Fe5270 versus $\log \sigma$, in that $\text{H}\beta$ closely follows the trends seen in Hn/Fe while the behavior of Fe5270 is similar to that of $\text{Mg } b$.

While the above discussion strongly indicates that there is a considerable spread in age among early-type galaxies, in particular a trend to young ages at low σ , two questions need to be addressed at this point. First, could some type of systematic effect lead to a spurious conclusion of young ages in galaxies? Second, the ages we have presented are based on a single pair of spectral indices; are consistent results obtained with other spectral indicators? We first consider several systematic effects that could, in principle, lead to incorrect age determinations, and then in §6 we evaluate the degree to which different Balmer and metal features produce consistent results.

5.3. Systematic Effects on the Integrated Spectra of Galaxies

5.3.1. A Metal-Poor Component in Early-Type Galaxies?

It has been pointed out in the past that the inability to model the integrated spectrum of early-type galaxies such as M32 with a single old-age SSP does not necessarily imply the existence of intermediate-age stars. Instead, one can argue for multiple metallicity components in these galaxies.

This approach has been advocated most recently by Maraston & Thomas (2000), who propose that the enhanced Balmer absorption lines found in many early-type galaxies can be reproduced by adding in an old metal-poor population, rather than resorting to intermediate-age populations. Since it is indeed crucial to distinguish between the intermediate-age and metal-poor population scenarios, we now address that degeneracy.

As has been described in Rose (1985, 1994), Leonardi & Rose (1996), Leonardi & Worthey (2000), and Leonardi & Rose (2002), the line ratio index composed of the Ca II H + H ϵ and Ca II K lines (hereafter referred to as the Ca II index) provides a sensitive test for the presence of early-type stars in an integrated spectrum, whether they come from young upper main sequence stars, blue stragglers, horizontal branch stars, or main sequence turnoff stars from a metal-poor population. The key idea is that for all cool stars the Ca II H and K line cores are saturated and insensitive to temperature, thus the line ratio is constant in cool stars. Only in stars hotter than early F does this ratio change, once the line cores are no longer saturated, and, once H ϵ , whose line center coincides with Ca II H, also begins to make a significant contribution. Thus the Ca II index provides a sensitive lever for detecting small amounts of hot stars in the integrated light.

In Fig. 9 we plot the Ca II index versus Hn/Fe, for the highest and lowest σ galaxies in our sample (in the previous references, Ca II has been plotted against H δ /Fe4045, rather than Hn/Fe), along with the model age and metallicity grid lines. Note that the Worthey models all arrive at an asymptotic value of ~ 1.2 for old age populations, independent of metallicity. The globular cluster 47 Tuc indeed lies just slightly below this old age value, which is consistent with a ~ 1 -2% contribution from blue stragglers at 4000 Å predicted by the color-magnitude diagram of its core region (Howell, Guhathakurta, & Gilliland 2000; Ferraro et al. 2001). On average, even the oldest galaxies in our sample are displaced by ~ 0.05 below the old-age value, and the previously identified young galaxies have low Ca II indices, consistent with ages below 2 Gyr.

As was pointed out by Rose (1985) in the case of M32, the ~ 0.05 discrepancy between the Ca II index of M32 and the cool star value can be accounted for by introducing either a small component of very young stars, blue stragglers, or a metal-poor component. In the latter case, which appears to be most plausible, given the inevitable existence of a metal-poor component in a chemically enriched galaxy, the Ca II discrepancy in M32 can be reproduced by adding in a $\sim 7.5\%$ contribution to the integrated light at 4000 Å from a metal-poor globular cluster spectrum. In fact, such a contribution is expected in the case of a closed box model (Rose 1985) and is in concert with the near-UV synthesis of M32 performed by Kjaergaard (1987). We reproduce the effect of this metal-poor contribution in Fig. 9. The large squares show the result of subtracting off varying amounts of light from M32 in the form of an integrated spectrum of the metal-poor Galactic globular cluster M15, smoothed to the same resolution as the FAST data. Specifically, the sequence of squares, moving away from the open square representing M32, are the results of subtracting 5%, 10%, 20%, and 30% of the light respectively. The key point is that if one tries to weaken the Balmer lines of M32 by removing the metal-poor component, one very quickly comes into conflict with the old-age value of the Ca II index. That is, the Ca II index is quickly affected

by the subtraction of hot stars, because those stars have unsaturated Ca II lines.

Removing $\sim 7\text{--}8\%$ of the light of M32 in the form of an M15 spectrum brings the Ca II index in concert with that of 47 Tuc, but only reduces the Hn/Fe index by a small amount (0.009). To displace M32 in Hn/Fe by the amount required to give it an old age in the Fe4383 versus Hn/Fe diagram of Fig. 6, i.e., ~ 0.08 in Hn/Fe, requires well in excess of 30% of the light coming from an M15 component, which is in strong violation of the Ca II criterion.

It has also been proposed recently that the strong Balmer lines in M32 and some other early-type galaxies can be reproduced by adding in a component of extreme horizontal branch (HB) stars, other hot stars in advanced evolutionary stages (De Propris 2000), and/or a population of hot blue stragglers. Again, either scenario avoids the necessity for intermediate ages. While we do not reproduce the specifics here, Rose (1985) placed upper limits of only a few percent of the light in M32 coming from *any* type of hot population, again based on the observed Ca II index. In short, the stringent limit on hot star light placed by the Ca II index definitely rules out the possibility that the enhanced Balmer lines in galaxies such as M32 can be ascribed to a population of hot stars, rather than to an intermediate age population.

In short, a small metal-poor contribution to the integrated light of early-type galaxies is indicated by the position of these galaxies in the Ca II versus Hn/Fe diagram. Removal of this apparently uniform contribution of $\sim 7\%$ at 4000 \AA will slightly increase the derived ages for all of the galaxies. However, the inferred age increase is small, and does not account for the galaxies, such as M32, with intermediate and young ages. The amount of age adjustment, naturally, is a function of the age of the galaxy, since the age lines crowd together at higher age, and also the contribution of the underlying metal-poor component will vary with age, due to the systematically brighter main-sequence turn off (MSTO) of a younger component. In the case of M32, the adjustment amounts to ~ 1 Gyr. Because the emphasis in this paper is on the age *distribution*, rather than *zero point*, and because correcting for a uniform metal-poor component will result in a systematic age shift, thus hardly affecting the age distribution, we do not choose to make that correction here.

5.3.2. Contamination from Red Horizontal Branch Stars?

The enhanced Balmer lines which lead to young age estimates for galaxies such as M32 in metal versus Balmer line diagrams can in principle be due to a population of red horizontal-branch (RHB) stars. These stars would be cool enough to have the Ca II index of a typical late-type star, but hotter than the MSTO of an old population. For example, the bluest RHB stars in 47 Tuc approach these characteristics. To assess this possibility, we rely on spectral indices, described extensively by Rose (1985, 1994), which are sensitive to surface gravity, and hence can be used to determine the relative contribution of dwarf and evolved stars to the integrated spectrum of a galaxy. Specifically, the two spectral indices used form the ratio of the singly ionized Sr II $\lambda 4077$

feature to the neutral $\lambda 4063$ Fe I feature (the SrII $\lambda 4077$ index) and the ratio of H δ to Fe I $\lambda 4063$ (the H $\delta/\lambda 4063$ index). In Fig. 10 we plot a sub-sample of galaxies in the surface gravity dependent SrII $\lambda 4077$ versus H $\delta/\lambda 4063$ diagram. The solid and dashed lines represent the mean relations for dwarfs and giants respectively, determined from the behavior of stars in the Coudé Feed spectral library. As has been discussed in Rose (1985, 1994) the separation of dwarfs and giants in this diagram is independent of metal-abundance, except in the case of the most metal-deficient stars ($[\text{Fe}/\text{H}] < -1.5$). As can be seen in Fig. 10, the Galactic globular cluster 47 Tuc lies between the dwarf and giant sequences, in fact close enough to the giant sequence to indicate that $\sim 2/3$ of its integrated light at 4000 \AA comes from evolved stars, which is in accord with its observed color-magnitude diagram (Schiavon et al. 2002a,b). In contrast, M32 lies close to the dwarf sequence, thereby ruling out the possibility that RHB stars are making a significant contribution. Hence the enhanced Balmer lines are indeed due to an intermediate age population. It is also evident in Fig. 10 that the other galaxies in the sample are clustered around the dwarf relation, thus the same conclusion should be drawn that RHB stars are not an important issue in early-type galaxies. Note that since the Fe I $\lambda 4063$ line is used in both indices, we can expect the galaxy index errors in the plot to be correlated. The left arrow in the plot shows the expected direction of the correlated errors.

5.3.3. The Effect of Emission Corrections

Contamination of the stellar absorption spectrum by emission is clearly a potential source of systematic error in age determinations. The most serious effect of a superposed emission spectrum is to fill in the Balmer absorption lines, thereby causing the galaxy age to be overestimated. Thus, varying amounts of emission fill-in, if not accounted for, can lead to a spurious spread in derived ages, in the sense that an emission-induced spread to older ages is produced. Note that this effect will only produce younger ages if an *overcorrection* is made for emission.

In §3.3 and in Appendix A we discussed the strategy for identifying and removing the effect of emission in our sample of early-type galaxy spectra. As described there, we either remove the emission, based on a determination of H α emission from supplementary red spectra, or use the [OII] $\lambda 3727$ line, along with an assumed [OII] $\lambda 3727/\text{H}\alpha$ ratio, to estimate the emission correction. The results of removing emission contamination of the Balmer line indices are plotted in Fig 11, where the galaxy data is plotted both before and after emission correction for both H β (left panel) and Hn/Fe (right panel) indices. As expected from the steep Balmer decrement in emission, the average emission correction is larger in H β than for the Hn/Fe index, but the corrections are modest in both cases, and certainly do not explain the young ages seen at low σ . An important point, to which we return in §6.3, is that at the high $\log \sigma$ end, both the mean H β at a given $\log \sigma$ and the scatter in H β are significantly affected by the emission corrections. Hence making the H β emission corrections accurately is crucial for determining the intrinsic scatter in age for the high σ galaxies from that index.

5.3.4. The Effect of NSAR Corrections

As was mentioned in §4.5 and fully described in Appendix B, the chemical composition of early-type galaxies deviates from the element abundance ratios found in the Galactic stars that comprise our empirical stellar database. The effects of non-solar abundance ratios (NSAR) on the various spectral indices used to characterize the galaxy integrated spectrum must be accounted for if reliable ages and heavy element abundances are to be extracted. In Figure 12, the effects of applying NSAR corrections to the Fe5270 versus $H\beta$ plot are shown. We have followed the prescription described in Appendix B, which follows that of Trager et al. (2000a) and Kuntschner et al. (2001). The primary effect, as expected, is to increase the overall heavy element abundance derived from the Fe5270 index, since iron is found to be underabundant, relative to magnesium, in early-type galaxies. We do not have prescriptions for correcting either the Fe4383 or Hn/Fe indices for NSAR effects. For both of these indices, the primary metal sensitivity is due to an Fe I absorption line, hence the derived abundances from the Fe4383 versus Hn/Fe diagram are primarily $[Fe/H]$. Therefore, we will use this index pair to measure only $[Fe/H]$, and not $[Z/H]$. On the other hand, the abundances derived from the NSAR-corrected Fe5270 versus $H\beta$ diagram reflect overall heavy element composition, thus are $[Z/H]$.

Hereinafter, we will explicitly use the term $[Z/H]$ (derived from the grid of Fe5270 vs Hn/Fe or $H\beta$) to refer to the mean abundance of all the heavy elements, which have the solar abundance pattern. We will use $[Fe/H]$ to refer specifically the iron abundance (derived from the grid of Fe4383 vs Hn/Fe), which may not reflect $[Z/H]$ precisely, because of the presence of NSAR. We will continue to use *metallicity* in a looser fashion, to refer either to $[Fe/H]$ or $[Z/H]$, depending on the context.

In Table 7 we summarize the effects on the derived mean ages and metallicities for our galaxy sample of both emission and NSAR corrections. For ages derived using the Hn/Fe index, the age shifts due to emission are fairly small, with the mean of the total sample changing from 8.9 to 8.2 Gyr. For $H\beta$ derived ages, the mean shift in age due to emission correction is somewhat larger, from 11.1 to 9.3 Gyr. The change in the metallicity determinations due to the emission correction is +0.03 dex in the $H\beta$ -Fe5270 grids, and is negligible (+0.002 dex) in the Hn/Fe versus Fe4383 grids. As expected, the NSAR corrections change the mean derived metallicity from the Fe5270 versus $H\beta$ diagram, from $[Fe/H]=-0.15$ to $[Z/H]=-0.03$, while the derived mean age is essentially unaffected by the NSAR corrections. In addition, the mean galaxy age extracted from the emission-corrected, but not NSAR-corrected, Hn/Fe versus Fe4383 (8.3 Gyr) is quite consistent with that derived from the emission and NSAR-corrected $H\beta$ versus Fe5270 (9.3 Gyr). Hence we infer that the lack of NSAR correction to Hn/Fe and Fe4383 does not produce a large bias in derived ages.

6. Consistency of Age and Abundance Determinations

At this point, a case has been made that the luminosity-weighted mean ages of early-type galaxies are substantially younger for low- σ galaxies, particularly those with $\log \sigma \leq 2.0$. In addition, an intrinsic scatter in several key spectral indicators, including those measuring Balmer line strength, appears to be present at *all* σ . We have considered and eliminated a variety of effects, other than mean age variations, that can explain the large variation in Balmer line strength observed in the low σ galaxies. In this section we take up the issue as to whether consistent age and metal abundance determinations are obtained from a variety of different spectral indicators. We are especially concerned with whether the higher order Balmer lines ($H\gamma$, $H\delta$, and $H8$) give similar results to that obtained with the Lick $H\beta$ index, whose characteristics as an age indicator have been well established.

In the preceding section we showed that early-type galaxies cover a large range in age when compared with model grids in the Fe4383 versus Hn/Fe diagram. To demonstrate that the basic results are not strictly dependent on the choice of metal feature, in Fig. 13 we plot the Lick Fe5270 index versus Hn/Fe. As can be seen by comparing with Fig. 6, the basic characteristic of the Fe4383 versus Hn/Fe diagram, i.e., a trend to young ages among the lower σ galaxies, is reproduced in the Fe5270 versus Hn/Fe diagram. Again, M32 is located among galaxies of the highest abundance.

6.1. Comparison Between Higher Order Balmer Lines and $H\beta$

A more stringent test of the age-metallicity determinations is to repeat the analysis for different Balmer lines, as well as for alternative measurements of a given Balmer feature. A natural starting point is to compare the results obtained from the higher order Balmer lines, as measured by the Hn/Fe index, with that obtained from the Lick $H\beta$ index, which has been extensively modeled and utilized in the literature (e.g., Trager et al. 2000a,b), and hence represents a benchmark for all age determinations. The galaxy data is compared with model grids in the Fe4383 versus $H\beta$ and Fe5270 versus $H\beta$ diagrams in Figs. 14 and 15, respectively. The $H\beta$ data has been corrected both for emission and NSAR effects, and Fe5270 has been corrected for NSAR. There are several aspects of the $H\beta$ plots which are noteworthy. First, the same qualitative features found in the higher order Balmer lines, as represented by Hn/Fe, are clearly present in both $H\beta$ plots. Most important, the general trend to young ages for lower σ galaxies is reproduced. Second, the model grid lines in $H\beta$ plots, especially in the Fe5270 versus $H\beta$ diagram, show a better orientation of isochrone and iso-metallicity lines along the index axes. This is due to the fact that the Lick $H\beta$ index is an equivalent width measure of that feature, while Hn/Fe is a relative measure of a Balmer line depth relative to an Fe line depth. Hence the $H\beta$ index more directly disentangles age from metallicity effects. A third feature of the $H\beta$ diagrams is that we find a greater number of galaxies lying outside the model grids lines at the oldest ages, which is strictly a zero point issue in the modeling. However, as a result it is easier to define a complete sample of ages and metallicities

from the Hn/Fe diagrams, especially for 4383 versus Hn/Fe, in which only four galaxies lie in a region of the diagram for which no age/metallicity extrapolation is possible.

From the four combinations involving the two metal lines, Fe4383 and Fe5270, and the two Balmer line indices, Hn/Fe and H β , we have produced four ages and metallicities for each galaxy. The results of these age and metallicity determinations are compiled in Table ???. The first column gives the galaxy ID, while columns (2) - (5) give the ages determined from Fe4383 *vs* Hn/Fe, Fe5270 *vs* Hn/Fe, Fe4383 *vs* H β , and Fe5270 *vs* H β , respectively. Columns (6) - (10) give the metal abundances determined from those same four combinations of indices. Errors in the ages and abundances are listed for the parameters derived from only the Fe4383 *vs* Hn/Fe diagram, since those for the other index combinations will be similar. These errors were derived by finding the maximum age and metallicity differences implied by the index errors & model grids.

To illustrate the degree to which these individual age and metallicity estimates correlate with each other, in Figs. 16 and 17 we show correlation plots for several combinations of age and metals determinations. The very tight correlation between ages derived from Fe5270 versus H β and those determined from Fe4383 versus H β again reflect the fact that age and metallicity are so nearly decoupled in these diagrams. Thus inconsistencies between Fe4383 and Fe5270 do not translate into corresponding age uncertainties. A more interesting comparison can be seen in the correlation between the H β -Fe5270 ages and the Hn/Fe-Fe4383 ages, since these ages come from completely independent sets of spectral indicators, with rather different measurement techniques. The correlation between the derived ages is quite good, with an rms scatter around a straight line fit of 3.4 Gyr. It is also clear that the age scale for Fe5270 versus Hn/Fe determinations is systematically lower at large age than for the other determinations. In the metallicity correlation plots, the best correlation is achieved, not surprisingly, when the same metal line is plotted versus the different Balmer indices. Note, however, that the correlation is still good between the [Fe/H] values extracted from Fe4383 versus Hn/Fe and the [Z/H] values derived from Fe5270 versus H β . In short, we find good overall consistency between age and abundance determinations based on the two distinct measures of Balmer line strength.

The previous results have demonstrated that the ages and chemical compositions of galaxies are reasonably well reproduced from one Balmer and metal feature to another. Specifically, we have made a detailed comparison between ages and metallicities derived from the H β and Hn/Fe Balmer line indices and the Fe4383 and Fe5270 metal line indices. We have also carried out a comparison between different methods for measuring specific Balmer lines. For instance, in the Rose line ratio index system, H γ is characterized by the index ratio H γ /Fe λ 4325. On the other hand, Worthey & Ottaviani (1997) defined an equivalent width measure of H γ , namely H γ_F . To compare the results obtained from these and other Balmer indices, we calculated the mean indices for the four different log σ groups for a variety of different indices. We then extracted mean ages and metallicities for these groups for various index combinations. The results for a variety of two-index diagrams are given in Table ???. These results are summarized as follows:

(1) The overall trend of younger to older mean age with increasing $\log \sigma$ is reproduced regardless of which Balmer and metal line combination is used.

(2) The mean ages and metallicities are particularly insensitive to the specific Fe feature used, as can be seen by comparing the Fe4383 results to the Fe5270 results.

(3) There are significant differences in zero point (and scale) in the ages that are derived from different Balmer lines, *particularly in the case of $H\delta$* . We note that while Schiavon et al. (2002a,b) are able to obtain consistency between the spectroscopic age for 47 Tuc, as derived from its integrated spectrum using both $H\beta$ and $H\gamma$, and the age based on its observed color-magnitude diagram, they are unable to obtain satisfactory agreement in the case of $H\delta$. The problem appears to reside in the contamination of the red wing of $H\delta$ by the CN 4216 band. This effect can be seen in the right panel of Fig. 4, where the spectra of several high σ galaxies with relatively old ages are plotted. Note that the pseudo-continuum peak redward of $H\delta$ is substantially lower than its counterpart on the blueward side of the line. Because the details of the CN feature are still not fully reproduced at the 1 Å level, it is difficult to assess to what extent the $H\delta$ line core may be contaminated by CN in the case of α -element enhanced galaxy spectra. Since the stellar spectra used in the SSP modeling come from solar neighborhood stars, the population models will not reproduce the enhanced CN features that are evident in, e.g., 47 Tuc and other Galactic globular clusters, and in the integrated spectra of globular clusters in M31 (Burstein et al 1984; Tripicco 1989).

(4) The derived ages from Balmer lines are reasonably insensitive to the method of quantifying the line strengths. Note that for both $H\gamma$ and $H\delta$ the derived ages are quite consistent between the line ratio indices ($H\gamma/4325$ and $H\delta/4045$) and the pseudo-equivalent width indices ($H\gamma_F$ and $H\delta_F$).

6.2. Comparison with Other Studies

With the large number of galaxies in our sample and the existence of stellar population studies similar to ours (Jorgensen 1999; Trager et al. 2000a; Kuntschner et al. 2001; Terlevich & Forbes 2002), it is worthwhile to compare our derived ages and metallicities with those published by other groups. Unfortunately, because our study has focused on the lower luminosity galaxies, our overlap with other groups is small. However, there are three studies for which we have galaxies in common. For the Gonzalez sample of primarily field ellipticals analyzed by Trager et al. (2000a) we have 9 galaxies in common; from the cluster and field sample of Kuntschner et al. (2001), we have 9 galaxies in common; and from the study of the Virgo cluster by Vazdekis et al. (2001b) we have 4 galaxies in common. The ages and metallicities determined in these studies are listed in Table 10 along with our values for comparison, and are shown graphically in Figure 18. The agreement is good between our determinations and those published by Trager et al. (2000a) and Vazdekis et al.

(2001b), and less so with the Kuntschner et al. (2001) study. There are four galaxies which are in common between three of the four studies, NGC 2778, NGC 4473, NGC 4478, and NGC 5831. With the exception of single “discordant” values for NGC 2778 and NGC 5831, the agreement for these multiply determined ages is good. As expected, the agreement is better in relative ages and metallicities than in the zero points between one study and another.

On the matter of the enhancement ratios (see appendix B), we can make a comparison only with the published Trager et al. Recall that we have avoided in this paper the massive galaxies, which would have the largest enhancement ratios, and hence the derived average ratios for the nine galaxies we have in common will not be large. For those galaxies, the mean $[E/Fe]$ ratio (the ratio of all “enhanced elements” to iron) found by Trager et al. is 0.11, while our value for $[Mg/Fe]$ is 0.04.

6.3. Intrinsic Scatter in Age and Metallicity

While there is little doubt from the previous discussion that the low- σ galaxies exhibit a pronounced trend towards lower luminosity-weighted mean age, a more subtle question regards the possibility of an intrinsic age spread among the higher- σ galaxies as well. Before considering the question from the perspective of age, i.e., a modeled parameter, we first revisit the issue as to whether intrinsic scatter is present among the Balmer line indices at high σ . The results of Table 4 indicate, at face value, that there is a significant intrinsic scatter present in all indices at high σ . Given, however, that emission and NSAR corrections do produce a significant change in the assessment of the scatter, it is worthwhile to consider the role played by these corrections. Of greatest significance is the effect of emission on Balmer line indices. Returning to Fig. 11 it is apparent that emission corrections are important for accurately assessing the high σ galaxies in $H\beta$, while they are substantially less important for Hn/Fe . More specifically, we previously found that the mean change in age that results from applying emission corrections to $H\beta$ is 1.8 Gyr (and 0.7 Gyr for Hn/Fe). This figure is actually an underestimate, since for many galaxies no age determination can be made before the correction is made, because the emission-contaminated indices lie outside the age-metallicity grid lines. Note that the observational error used in extracting the intrinsic scatter in §5 only includes the actual uncertainties in the observations, and does not include the uncertainty introduced in making the emission correction. Hence part of the intrinsic scatter found for the emission-corrected Balmer indices could in principle be due to errors in correcting for emission.

We now take a closer look at the issue of age scatter as determined from the Hn/Fe index. An inspection of Fig. 6 indicates that, even among the higher- σ galaxies, there is a sizable spread in that diagram, particularly in age. We discuss two ways to demonstrate that a true age spread is apparent even in the high σ galaxies. First, we show that the more extreme examples of younger and older galaxies are indeed reproducibly different in their spectra, i.e., are not simply due to observational scatter from low S/N ratio. We then show that the distribution of high σ galaxies in

the Fe4383 versus Hn/Fe diagram has a scatter in excess of that expected from the observational errors.

To show that there is a systematic change in the spectra from the youngest to oldest galaxies in the high σ sample, in Fig. 19 we plot the spectra of five high- σ galaxies, ranging in derived age from 2.8 Gyr to 12.3 Gyr, based on their location in Fig. 6. Note that as one proceeds from the bottom (oldest) spectra, to the top (youngest) spectrum, a systematic change can be seen in the three higher order Balmer lines, H γ , H δ , and H8, relative to their neighboring metal lines. Specifically, in the bottom two spectra H γ is weaker than Fe4325, while in the top spectra it is stronger. Likewise, H δ is slightly weaker than the neighboring blended feature at 4063 Å in the bottom spectra, while in the top spectrum it is distinctly stronger than that feature. Finally, while H8 is buried in the CN3883 band in the bottom spectrum, it clearly emerges at 3888 Å in the top spectra. The systematic trend in all three Balmer lines, from younger to older galaxies, coupled with the reproducible nature of the metal lines from one galaxy to another, indicates the reality of the changing Balmer line strengths along the age sequence. However, the changes in Balmer line strength from 12.3 Gyr to 2.8 Gyr is indeed quite subtle, i.e., high S/N ratio is required to discriminate such age changes from integrated spectra.

To further demonstrate the degree of intrinsic age and metallicity scatter among the higher σ galaxies, we have simulated the expected observational scatter in the Fe4383 versus Hn/Fe diagram under different assumptions regarding the intrinsic age and metallicity scatter in the galaxies. The results of these simulations are displayed in Fig. 20. In the upper left panel, (a), we have assumed a single mean age and metallicity for all of our simulated galaxies, hence only observational errors, and interpolated the Hn/Fe and Fe4383 indices corresponding to that age and [Fe/H]. We then randomly sampled 150 times from Gaussian error distributions having rms scatters of ± 0.014 and ± 0.21 , which correspond to the median observational errors in Hn/Fe and Fe4383, respectively. In each case we added the observational errors to the mean indices corresponding to the selected mean age and metallicity of 9.5 Gyr and [Fe/H]=-0.07. In Fig. 20(a) we have plotted both the actual galaxy observations for the high- σ galaxies ($\log \sigma > 2.2$), as asterisks, and the simulated data, as unfilled circles. The large filled square represents the observed data for M32. As usual, we plot the age and metallicity grid lines determined from the modeling. It is evident that the observed data has a significantly larger scatter than the simulations. Hence we conclude that some intrinsic scatter in age and/or metallicity must be present in the high- σ galaxies.

In Fig. 20(b) we have included an intrinsic scatter in age of ± 2 Gyr. To simulate such an age spread, we first randomly selected 150 times from an age distribution with an rms dispersion of ± 2 Gyr and a mean of 9.5 Gyr. In all cases the metallicity was held fixed at [Fe/H]=-0.07. For each realization, we interpolated the Hn/Fe and Fe4383 indices for the given age and [Fe/H]. We then randomly selected observational errors in Hn/Fe and Fe4383 for each trial galaxy following the prescription above. It is evident that the simulated galaxy data more closely follows the observed data than in the case of Fig. 20(a). As a further test, we held the age fixed at 9.5 Gyr and randomly selected in [Fe/H] with an rms dispersion of ± 0.1 around a mean value of -0.07. After adding in

observational error, we find the distribution of points plotted in Fig. 20(c). The correspondence with the actual galaxy data is noticeably better in the case of Fig. 20(b), where an age scatter is introduced, rather than a metallicity scatter. Finally, in Fig. 20(d) we have introduced a correlated age and metallicity scatter. We first randomly selected 150 ages with an rms scatter of 2 Gyr around the mean age of 9.5 Gyr. Then for each age we calculated a metallicity according to the prescription:

$$[\text{Fe}/\text{H}] = -0.3 \log(\tau/9.5) - 0.07,$$

where τ is the age, in Gyr, of the simulated galaxy. Then we perturbed the metallicity by randomly sampling from a distribution with an rms of ± 0.05 , and finally added in a randomly sampled observational error. The results of this simulation can be compared to the observed galaxy data in Fig. 20(d). This correlated age-metallicity prescription appears to provide a closer representation to the observed galaxy data than either a scatter in age or metallicity alone.

In short, while the higher- σ galaxies clearly form a systematically older sample in age than their lower- σ counterparts, there are signs of an intrinsic spread in age even among these more massive galaxies. We return to this issue in more detail in Papers II and III.

7. Discussion & Conclusions

While the previous sections have focused on establishing the reliability of the ages and metallicities derived in our study, here we emphasize our principal results for the E/S0 stellar populations and then briefly examine the implications for hierarchical models of galaxy evolution. We begin by showing the trend of mean age in our sample as a function of the measured velocity dispersion in Fig. 21. Different symbols distinguish the field and Virgo samples (discussion of those samples will be taken up in the succeeding papers). In addition to the scatter seen at all velocity dispersions discussed above, a clear trend is seen, such that lower σ galaxies have younger ages. We have again used our velocity dispersions for consistency even though some values for low mass galaxies are higher than literature values. The overall sense of this figure does not change if we use the smaller dispersions. The ages in this figure come from the H γ /Fe-Fe 4383 diagram; if we use the H β -Fe 5270 diagram, which is corrected for NSAR, the same basic character of the data is found.

There are then three principal conclusions to arise from the work presented in this paper. First, there is a large intrinsic spread in Balmer line strength at low σ (Table 4), and it appears that a small intrinsic spread is present at high σ as well. This spread in Balmer line strength has been extensively modeled and shown to be due primarily to a spread in age. Second, the mean age of galaxies increases with increasing velocity dispersion, leading to an age- σ trend, shown in Figure 21. Although no age- σ trend was observed in the samples of Kuntschner (2000) or Terlevich and Forbes (2001), our observed age- σ trend is in accordance with the results of Trager et al. (2002a,b), who suggest that large Es are older, on average, than smaller Es. It is not clear from Figure 21 whether there exists a continuous age- σ correlation, or whether there are two distinct populations — a

sample of younger, low- σ galaxies ($\log \sigma \leq \sim 2.1$) and a sample of older, high- σ galaxies. With the available information, we cannot reliably distinguish between these two scenarios. Third, the trend in $[Z/H]$ with σ is modest, as seen in Fig. 22, where the $[Z/H]$ values derived from the NSAR-corrected Fe5270 and $H\beta$ indices are plotted versus $\log \sigma$. A fit to the relation in Fig. 22 yields a slope of 0.32, such that $[Z/H]$ increases by only ~ 0.2 over the observed range of $1.6 < \log \sigma < 2.4$.

Can our results place key constraints on age distributions predicted by numerical simulations of structure formation in the universe? The most extensively modeled scenario is the cold dark matter picture, in which structure evolves through a hierarchical sequence of mergers (e.g., Davis et al. 1985). Two basic features of all hierarchical models provide testable predictions. First, it is expected that the merger process will lead to a significant scatter in the ages of assembly of the present epoch dark matter halos. Second, the merger sequence naturally leads to an earlier assembly epoch (and hence older age) of the dark matter halos in lower mass galaxies, while the assembly of the higher mass galaxies occurs more recently, on average. Consequently, the hierarchical models tend to predict that more massive early-type galaxies should have younger mean ages than low mass galaxies (Kauffmann 1996; Kauffmann & Charlot 1998; Somerville & Primack 1999). Our results do indeed indicate a substantial scatter in the ages of early-type galaxies, consistent with a hierarchical scenario. On the other hand, we find the lower mass galaxies to be younger, which reverses the trend of the hierarchical predictions. We reserve a more extensive discussion of this apparent discrepancy to Paper III, but refer the reader to a discussion of this point in Terlevich & Forbes (2002).

The emphasis of this first paper has been to describe the techniques used to measure key spectral indicators and to model them through evolutionary population synthesis. We have demonstrated that spectral indicators which measure Balmer lines from $H\beta$ through $H8$, and measured using different techniques, give consistent results for the luminosity-weighted mean ages of early-type galaxies. Our principal conclusion then is that a significant trend is present between galaxy mean age and mass in the sense that galaxies with velocity dispersions below 100 km s^{-1} are younger on average than their higher σ counterparts.

We wish to thank G. Worthey for generously providing his evolutionary synthesis code, which has been resident at UNC for many years now. We are also grateful to R. Kurucz for making available his stellar atmosphere models and SYNTHE code. In addition, we thank A. Leonardi for updating the Worthey models by producing and incorporating the Kurucz synthetic spectra for hotter stars and for other updates to the original Worthey models. H. Kuntschner kindly supplied us with the ages and abundances of the galaxies in his sample. We thank the Mount Hopkins observers, Perry Berlind and Michael Calkins for obtaining some of the data reported here. Lastly, we thank the referee for comments that helped us to improve the presentation of this paper. This research was partially supported by NSF grant AST-9900720 to the University of North Carolina.

A. Emission Corrections

The detection of an emission spectrum superimposed on an absorption spectrum is a non-trivial task. In the case of the age-sensitive Balmer lines, the task is particularly problematic, since the extracted emission line strength will depend strongly on the assumed character of the underlying absorption spectrum. Naturally, the properties of the absorption spectrum are themselves strongly dependent on the presumed age and metallicity of the galaxy, yet these are the quantities that we wish to determine. The problem is less severe for most of the forbidden metal lines, which tend to be superimposed on regions of the absorption spectrum that are less sensitive to assumptions about the stellar population. However, unless the temperature, chemical composition, and emission mechanism for the ionized gas can be independently determined, the ratio of emission in the forbidden metal lines to that in the Balmer lines is not well constrained. To correct for the effects of emission on the absorption line strengths, we have obtained spectra in the red, centered near $H\alpha$ for 40% of the galaxies in our sample. A description of those observations is given in §2.2.2. The observed galaxies are indicated in column 9 of Table 1, where a “y” designation indicates that emission is detected in the galaxy and the $[NII]/H\alpha$ emission line intensity ratio is reliably measured, a “n” indicates that emission was not detected, and a “u” indicates that emission is probably detected, but no reliable value can be determined for the $[NII]/H\alpha$ ratio.

A.1. Measuring the Flux in $H\alpha$

To evaluate the emission contamination of the Balmer lines, we exploit two basic advantages of $H\alpha$ for this purpose. First, while the equivalent widths of the Balmer absorption lines are relatively constant along the Balmer sequence, the emission decrement is steep. Thus at $H\alpha$ we maximize the contribution of emission relative to the underlying absorption. Second, at $H\alpha$ the sensitivity to the age and chemical composition of the underlying absorption spectrum is minimized (compared with the higher order Balmer lines). This is due to the fact that at $H\alpha$ the light is preferentially dominated by the giant branch, thus relatively insensitive to age when compared to the higher order Balmer lines (where the main sequence turnoff light provides a higher contribution).

The emission contamination was detected and removed in the following manner. Of the 69 galaxies in our sample for which we have spectra at $H\alpha$, 29 of those have no detected emission in the $[OII]\lambda 3727$ line and are consequently considered to be emission free. From this sample of 29 emission free galaxies we have measured the relation between the Hn/Fe index (which measures higher order Balmer line absorption strength) and the $H\alpha$ absorption. A linear regression yields the relationship:

$$H\alpha_{absorption} = -2.15(Hn/Fe) + 3.94 \quad (A1)$$

with an rms scatter around the mean relation of ± 0.14 , after eliminating two discrepant galaxies. Since none of the galaxies are plagued by strong emission, we make the assumption that the emission is small enough in the $H\gamma$ and higher order Balmer lines so that the observed Hn/Fe indices for

our galaxy spectra provide a good indicator of the true underlying absorption spectrum and a reliable predictor of the strength of $H\alpha$ absorption. For a given emission-contaminated galaxy, we select from our sample of 29 emission-free galaxies a galaxy whose Hn/Fe index closely matches that of the contaminated galaxy and preferably has a lower velocity dispersion. From the velocity dispersion information determined from the blue spectra, we then smooth the red spectra of both the contaminated galaxy and the emission-free template to a common resolution, normalize the continuum of the template spectrum to that of the contaminated spectrum in the vicinity of $H\alpha$ and then subtract off the template. From the difference spectrum the flux of $H\alpha$ emission is measured, using the IRAF *splot* routine. Then, assuming the emission follows the expected Case B Balmer decrement (Osterbrock 1989), the expected $H\beta$ emission flux is determined.

To translate the estimated $H\beta$ emission flux into corrected absorption line indices in the blue, a spectrum of the Balmer decrement must be subtracted from the contaminated blue spectrum. We have produced a spectrum of the Balmer decrement covering $H\beta$ through $H8$ from a flux-calibrated observation of the Orion nebula taken with the same instrumental set-up as the galaxy spectra. The individual relative hydrogen line strengths are adjusted to the Case B recombination spectrum values. This spectrum, hereafter referred to as the Balmer decrement spectrum, is then smoothed to the velocity dispersion of the emission-contaminated galaxy and normalized to have the same $H\beta$ emission flux as that expected from the $H\alpha$ emission for the galaxy. The blue contaminated spectrum is then normalized to match the flux level of the red spectrum by utilizing the $\sim 50\text{\AA}$ of overlap between the blue and red spectra at $\lambda 5500\text{--}5550$. Finally, the Balmer decrement spectrum is subtracted from the normalized blue spectrum, which yields the “corrected” Balmer absorption line strengths. The Hn/Fe index is re-measured and the process is repeated, usually only once, until the corrected Hn/Fe converges to a stable value.

Errors in this correction could result from a lack of spatial correspondence of the blue spectra and the $H\alpha$ spectra, which is the case for some of the galaxies. If the emission distribution is not uniform (which is usually the case), then spectra taken at different position angles will have different amounts of emission contribution to the absorption spectrum. However, in general the emission found in E/S0 galaxies is highly concentrated (Buson et al. 1993), and the extraction of our blue and red spectra was heavily weighted towards the central few arcseconds. Thus we feel that any associated errors are minor.

A.2. Measuring the $H\alpha$ Flux via the $[OII]\lambda 3727$ Flux

The method described above for correcting the emission contamination constitutes our preferred technique, since the corrections are based directly on the amount of $H\alpha$ emission observed on an individual galaxy basis. However, we do not have red spectra, and hence the $H\alpha$ emission information, for all of the galaxies in the sample. Rather than leave the line indices uncorrected for the remaining 60% of the galaxies, we have opted to correct the indices by inferring the $H\alpha$ emission flux from the emission present at the $[OII]\lambda 3727$ doublet. In this method, the assumption

is that the excitation mechanism for emission in early-type galaxies shows little variation from one galaxy to another.

Measuring the emission flux in the [OII] λ 3727 line first requires subtracting off the underlying continuum. To do this, an emission-free template galaxy is chosen, VCC1279, and all galaxies are normalized to match the continuum level near λ 3727 for that galaxy. The template galaxy is then subtracted from each normalized galaxy spectrum, and the residual emission flux at [OII] is measured. For the galaxies *with* emission information at $H\alpha$, the red spectra are re-normalized to match the overlap with their blue counterparts, and the flux in the [NII] λ 6584 line is measured. A comparison between the two emission line fluxes yields a median $\log([NII]/[OII])$ ratio of -0.45 (Figure 23). Thus, for each galaxy *without* information in the red, the [OII] emission flux can be measured, and, from the median of the flux ratio, an estimate of the flux at [NII] can be made. Since the ultimate goal is to correct the Balmer line indices, the flux in [NII] must now be related to the expected flux in the Balmer lines. For the galaxies in our sample that have observed emission lines in their red spectrum, we have measured the ratio of the flux at [NII] compared to the flux at $H\alpha$ (Figure 23) and find a median $\log([NII]/H\alpha)$ value for the sample of 0.1. Assuming that all galaxies have the same emission mechanism and the same ratio, (which is not true, of course, but only an approximation), the expected flux in the $H\alpha$ emission line can be estimated. Finally, using the Case B Balmer decrement, the emission flux in $H\beta$ is determined.

To translate the $H\beta$ emission flux estimated for each galaxy into spectral index corrections, we first evaluate the effects of a range of emission fluxes on two individual galaxies, VCC1279, an old galaxy, and VCC1912, a young galaxy. The Balmer decrement spectrum is scaled to reflect the range of expected $H\beta$ emission fluxes ($0.5\text{--}5.0 \times 10^{-15}$) for the galaxy sample and subtracted from the two template galaxies. The index values are measured for each of the Balmer-subtracted galaxy spectra and the change in the index values as a function of the removed emission flux is determined from a linear fit. The coefficients of these fits are given in Table 11.

In summary, for each galaxy in the sample that has not already been corrected for emission contamination, the flux in the OII line is measured. The OII flux is related to the NII flux, and in turn, the $H\alpha$ flux and the $H\beta$ emission flux. Once the $H\beta$ flux is estimated, corrections to the line indices are made using the linear relations in Table 11. For the two main age indicators used in this work – the Lick $H\beta$ index and the Rose Hn/Fe index – the mean index corrections are 0.15 and 0.012, respectively. For a stellar population with an age of 8 Gyr, these corrections correspond to an age difference of 0.5-1 Gyr, depending on the metallicity. To gauge the reliability of using the OII emission line flux to correct the spectral indices, we have compared the corrected index values for both this method and the more robust method using the $H\alpha$ emission flux from the red spectra (§3.3.2). Figure 24 shows that the results of the two methods agree quite well, with an rms scatter about the unity line of 0.25.

B. Correction for Non-Solar Abundance Ratios

As mentioned in §4.5, the analysis of the integrated light of galaxies is plagued by the fact that both the current models and the empirical stellar spectral libraries are based on stars having solar abundance ratio patterns. Below we describe how corrections are made for NSAR. These corrections are entirely based on the extensive work carried out by Trager et al. (2000a) and by Kuntschner et al. (2001).

B.1. Evidence for NSAR

Shown in Figure 25 are three index-index grids – Fe 5270 vs. $H\beta$, Mg b vs. $H\beta$, and Fe 5270 vs. Mg b – with our galaxy data over-plotted. Of interest in these diagrams is the fact that the mean age and metallicity of the galaxy sample changes from diagram to diagram. Specifically, the galaxies appear to be older and more metal-poor in the Fe5270- $H\beta$ diagram than they do in the Mg b - $H\beta$ diagram. The different metallicity (and age, to a lesser extent) predictions can be most easily seen in the upper left panel of Figure 25 in which the bulk of the galaxies lie offset from the Mg-Fe population grids. This discrepancy between the metal abundances derived from the two different indices is further demonstrated in Fig. 26, and is now widely accepted to be caused by non-solar abundance ratio effects. Namely, the models predict too little Mg at a given Fe-absorption line strength, since the massive early-type galaxies have an enhancement of Mg (and other α elements) relative to the solar-abundance stars which comprise the population synthesis models. Recently, Trager et al. (2000a) have argued that rather than considering Mg and other α -elements to be enhanced in massive early-type galaxies, one should consider the Fe-peak elements to be underabundant.

B.2. Scaling the Galaxies to Solar-Abundance

The overabundance of certain elements compared to Fe (or more appropriately, the underproduction of Fe compared to the α elements) has a profound effect on the use of age/metallicity index diagrams if the model predictions reflect only solar abundance ratios. As noted above, the Mg-derived metal abundances will be greater than those derived using an Fe-index. In addition, since the age-metallicity degeneracy has not been completely broken (the age and metallicity tracks are not perpendicular in the model grids), the age estimates derived using Mg and Fe line indices will differ as well. Thus, trends in the intrinsic abundance ratios of the galaxies can lead to artificial trends in metallicity and/or age if the galaxies are not scaled to reflect the same elemental abundance ratios.

Recently, Trager et al. (2000a) carried out an extensive investigation of the effects of NSAR in early-type galaxies and tabulated corrections for a selection of important Lick indices based

on the work of Tripicco & Bell (1995) and the Worthey models. We use their preferred Model 4 (enhancement in both C and O) corrections (given in their Table 5) and the method of Kuntschner et al (2001) to correct a subset of our indices for the effects of NSAR. The first step in the correction process is to estimate the galaxy age using the program described in §4.4, using $H\beta$ -Fe5270 model index grids (Figure 25). Galaxies which lie outside the grids are assigned an age of 19 Gyr. Each galaxy is then shifted in the Mg b -Fe5270 index grid, along the ratio vector defined from Table 5 of Trager et al. (2000a), until it reaches the age predicted by the $H\beta$ index. The amount that the galaxy is shifted in the Mg-Fe index grid determines the scaling factor for that galaxy, which is then used to correct the other indices with δ s listed in Table 5 of Trager et al. (2000a), including $H\beta$. The galaxy age is then redetermined using the corrected index values on the $H\beta$ -Fe5270 index grid, and shifted further in the Mg-Fe diagram until the corrected age estimate is reached. The remaining indices are then corrected for the new scaling factor and the entire process is reiterated one final time. The mean changes in all NSAR-corrected indices, $\Delta\text{Index} = \text{Index}(\text{NSAR}) - \text{Index}(\theta)$, are -0.038 for $H\beta$, -0.307 for Mg b , and 0.178 for Fe 5270.

B.3. Calculating the Abundance Ratios

A measure of the Mg/Fe enhancement ratio in the galaxies can be estimated by comparing the metallicity derived from a non-NSAR-corrected $H\beta$ -Fe diagram to that measured in a non-corrected $H\beta$ -Mg b diagram (e.g, Figure 25). Determining the metallicity from these diagrams is complicated by the large number of galaxies that lie outside the model grids whose metallicities must be extrapolated. Recent studies have found a mean enhancement ratio of $\text{Mg/Fe} \approx +0.3$ dex in luminous E’s (e.g., Trager 2000a, Kuntschner 2001), yet the mean value for our sample is found to be half of this value. Because our sample is dominated by lower mass systems which tend to have solar or only mildly enhanced abundance ratios, the difference is not unexpected.

REFERENCES

- Akritas, M. G., & Bershad, M. A. 1996, *ApJ*, 470, 706
- Baldwin, J. A., Phillips, M. M., & Terlevich, R. 1981, *PASP*, 93, 5
- Benson, A. J., Pearce, F. R., Frenk, C. S., Baugh, C. M., & Jenkins, A. 2001, *MNRAS*, 320, 261
- Bertelli, G., Bressan, A., Chiosi, C., Fagotto, F., & Nasi, E. 1994, *A&AS*, 106, 275
- Bessell, M. S., Brett, J. M., Wood, P. R., and Scholtz, M. 1989, *A&A*, 213, 209
- Bessell, M. S., Brett, J. M., Wood, P. R., and Scholtz, M. 1991, *A&AS*, 89, 335
- Brown, J. A., & Wallerstein, G. 1992, *AJ*, 104, 1818
- Burstein, D., Faber, S. M., Gaskell, C. M., & Krumm, N. 1984, *ApJ*, 287, 586
- Buson, L. M., Sadler, E. M., Zeilinger, W. W., Bertin, G., Bertola, F., Danzinger, J., Dejonghe, H., Saglia, R. P., & de Zeeuw, P. T. 1993, *A&A*, 280, 409
- Caldwell, N. 1984, *PASP*, 96, 287
- Carretta, E., & Gratton, R. G. 1997, *A&AS*, 121, 95
- Concannon, K. D., Rose, J. A., & Caldwell, N. 2000, *ApJ*, 536, L19
- Davis, M., Efstathiou, G., Frenk, C. S., & White, S. D. M. 1985, *ApJ*, 292, 371
- De Propris, R. 2000, *MNRAS*, 316, L9
- de Vaucouleurs, G., de Vaucouleurs, A., Corwin, H. G., Buta, R. J., Paturel, G., & Fouque, P. 1991, “Third Reference Catalogue of Bright Galaxies, Version 3.9”
- Dopita, M. A., & Sutherland, R. S. 1995, *ApJ*, 455, 468
- Faber, S. M., Friel, E. D., Burstein, D., & Gaskell, C. M. 1985, *ApJS*, 57, 711
- Fabricant, D., Cheimets, P., Caldwell, N., & Geary, J. 1998, *PASP*, 110, 79
- Falco, E. E., Kurtz, M. J., Geller, M. J., Huchra, J. P., Peters, J., Berlind, P., Mink, D. J., Tokarz, S. P., & Elwell, B. 1999, *PASP*, 111, 438
- Ferland, G. J., & Netzer, H. 1983, *ApJ*, 264, 105
- Ferraro, F. R., D’Amico, N., Possenti, A., Mignani, R. P., & Paltrinieri, B. 2001, *ApJ*, 561, 337
- Gabel, J. R., & Bruhweiler, F. C. 2002, *AJ*, 124, 737
- Geha, M., Guhathakurta, P., & van der Marel, R. P. 2002, *AJ*, 124, 3073

- Gibson, B. K., Madgwick, D. S., Jones, L. A., Da Costa, G. S., & Norris, J. E. 1999, *AJ*, 118, 1268
- Grundahl, F., Stetson, P. B., & Andersen, M. L. 2002, *A&A*, 395, 481
- Gunn, J. E., & Stryker, L. L. 1983, *ApJS*, 52, 121
- Howell, J. H., Guhathakurta, P., & Gilliland, R. L. 2000, *PASP*, 112, 1200
- Huchra, J. P., Davis, M., Latham, D., & Tonry, J. 1983, *ApJS*, 52, 89
- Jones, L. A. 1999, Ph.D. Thesis, University of North Carolina
- Jones, L. A., & Worthey, G. 1995, *ApJ*, 446, L31
- Jorgensen, I. 1999, *MNRAS*, 306, 607
- Kauffmann, G. 1996, *MNRAS*, 281, 487
- Kauffmann, G., & Charlot, S. 1998, *MNRAS*, 294, 705
- Kauffmann, G., Colberg, J., Diaferio, A. & White, S. D. M. 1999a, *MNRAS*, 303, 188
- Kauffmann, G., Colberg, J., Diaferio, A. & White, S. D. M. 1999b, *MNRAS*, 307, 529
- Kjaergaard, P. 1987, *A&A*, 176, 210
- Kuntschner, H. 2000, *MNRAS*, 315, 184
- Kuntschner, H., Lucey, J. R., Smith, R. J., Hudson, M. J., & Davies, R. L. 2001, *MNRAS*, 323, 615
- Kuntschner, H., Smith, R. J., Colless, M., Davies, R. L., Kaldare, R., & Vazdekis, A. 2002, *MNRAS*, 337, 172
- Kurucz, R.L. 1993, *SYNTHE Spectrum Synthesis Programs and Line Data* (Kurucz CD-ROM No 18)
- Kurucz, R.L. 1994, *Solar Abundances Model Atmospheres for 0,1,2,4,8 km s⁻¹* , (Kurucz CD-ROM No19)
- Leitherer, C., et al. 1996, *PASP*, 108, 996
- Leonardi, A. J., & Rose, J. A. 1996, *AJ*, 111, 182
- Leonardi, A. J., & Rose, J. A. 2002, *AJ*, (submitted)
- Leonardi, A. J., & Worthey, G. 2000, *ApJ*, 534, 650
- Liu, W. M., & Chaboyer, B. 2000, *ApJ*, 544, 818

- Maraston, C., & Thomas, D. 2000, *ApJ*, 541, 126
- McElroy, D. B. 1995, *ApJS*, 100, 105
- O’Connell, R. W. 1976, *ApJ*, 206, 370
- Osterbrock, D. E. 1989, *Astrophysics of Gaseous Nebulae and Active Galactic Nuclei*, (Mill Valley, CA: University Science Books)
- Pedraz, S., Gorgas, J., Cardiel, N., Sanchez-Blazquez, P., & Guzman, R. 2002, *MNRAS*, 332, L59
- Peletier, R. F. 1989, Ph.D. Thesis, University of Groningen
- Phillips, M. M., Jenkins, C. R., Dopita, M. A., Sadler, E. M., & Binette, L. 1986, *AJ*, 91, 1062
- Proctor, R. N., & Sansom, A. E. 2002, *MNRAS*, 333, 517
- Rose, J. A. 1984, *AJ*, 89, 1238
- Rose, J. A. 1985, *AJ*, 90, 1927
- Rose, J. A. 1994, *AJ*, 107, 206
- Rose, J. A., & Deng, S. 1999, *AJ*, 117, 2213
- Salaris, M., & Weiss, A. 1998, *A&A*, 335, 943
- Salasnich, B., Girardi, L., Weiss, A., & Chiosi, C. 2000, *A&A*, 361, 1023
- Simien, F., & Prugniel, Ph. 2002, *A&A*, 384, 371
- Smith, Russell J., Lucey, John R., Hudson, Michael J., Schlegel, David J., & Davies, Roger L. 2000, *MNRAS*, 313, 469
- Somerville, R. S., & Primack, J. 1999, *MNRAS*, 310, 1087
- Terlevich, A. I., & Forbes, D. A. 2002, *MNRAS*, 330, 547
- Terlevich, R., & Melnick, J. 1985, *MNRAS*, 213, 841
- Trager, S., Faber, S., Worthey, G., & Gonzalez, J. 2000a, *AJ*, 119, 1645
- Trager, S., Faber, S., Worthey, G., & Gonzalez, J. 2000b, *AJ*, 120, 165
- Tripicco, M. J. 1989, *AJ*, 97, 735
- Tripicco, M. J., & Bell, R. A. 1995, *AJ*, 110, 3035
- VandenBerg, D. A., Swenson, F. J., Rogers, F. J., Iglesias, C. A., & Alexander, D. R. 2000, *ApJ*, 532, 430

- Vazdekis, A., Peletier, R. F., Beckman, J. E., & Casuso, E. 1997, *ApJS*, 111, 203
- Vazdekis, A., & Arimoto, N. 1999, *ApJ*, 525, 144
- Vazdekis, A., Salaris, M., Arimoto, N., & Rose, J. A. 2001a, *ApJ*, 549, 274
- Vazdekis, A., Kuntschner, H., Davies, R. L., Arimoto, N., Nakamura, O., & Peletier, R. 2001b, *ApJ*, 551, L127
- Worthey, G. 1994, *ApJS*, 95, 107
- Worthey, G., Faber, S. M., & Gonzalez, J. J. 1992, *ApJ*, 398, 69
- Worthey, G., Faber, S. M., Gonzalez, J. J., & Burstein, D. 1994, *ApJS*, 94, 687
- Worthey, G., & Ottaviani, D. L. 1997, *ApJS*, 111, 377
- Zoccali, M., et al. 2001, *ApJ*, 553, 733

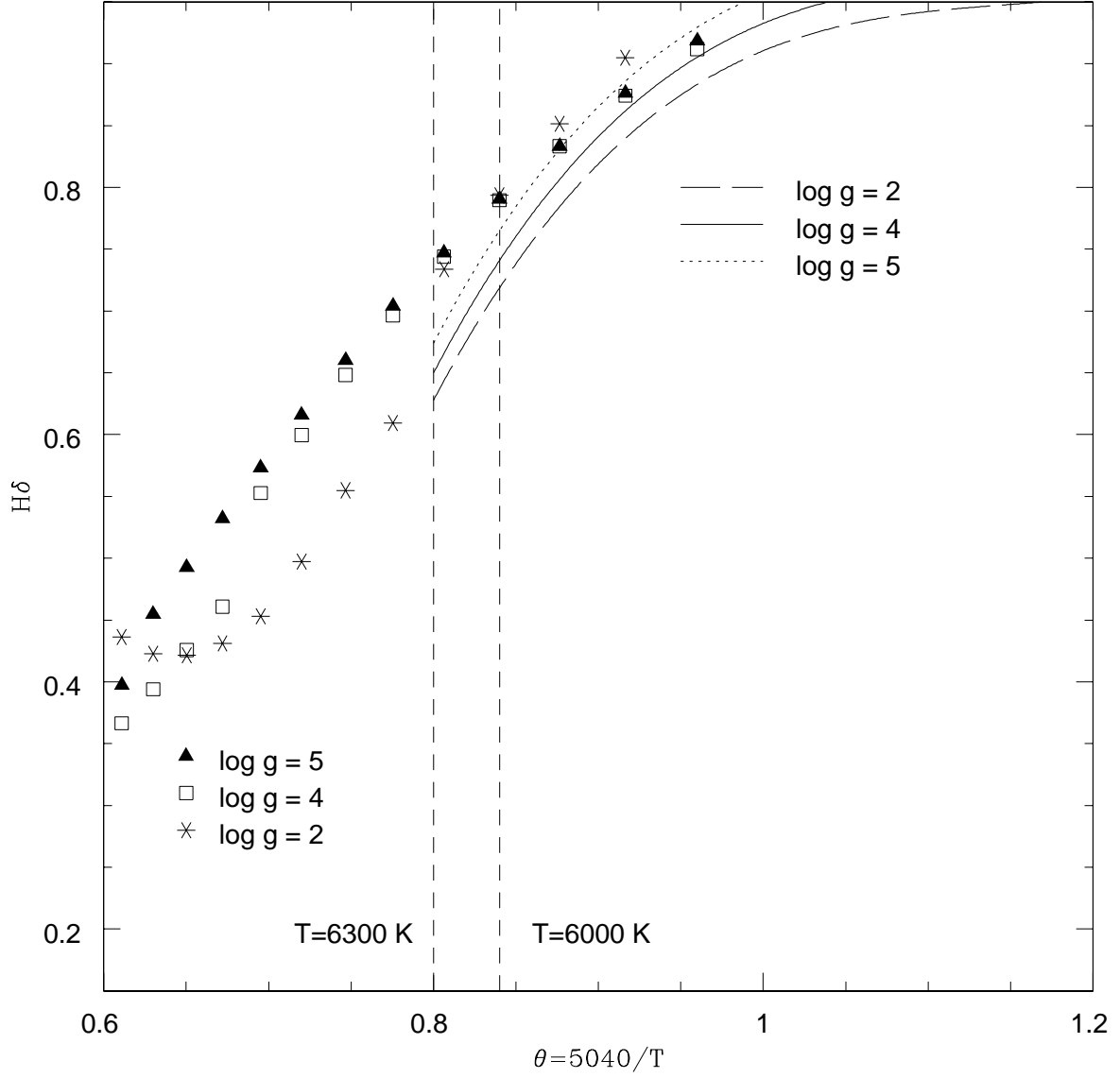


Fig. 1.— Comparison between the empirical $H\delta$ line strength fitting function (curves) and the synthetic library stars (symbols) for solar metallicity and three different surface gravities. The region of overlap is indicated by the vertical dashed lines. The fitting functions are calculated for $T < 6300 \text{ K}$ and used for $T < 6000 \text{ K}$.

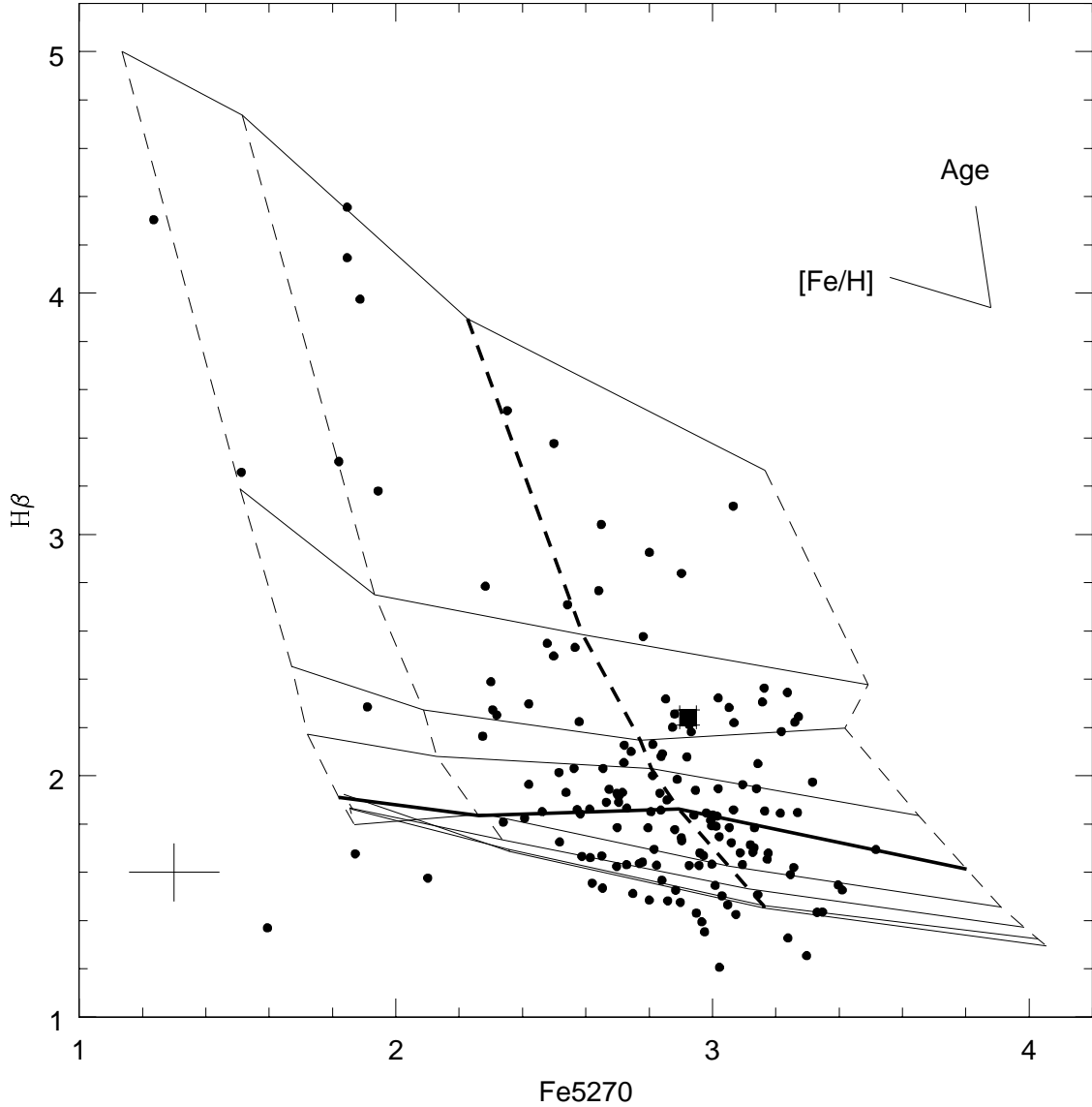


Fig. 2.— A sample of the galaxy distribution (filled circles) on an iron versus Balmer line index grid. The Fe 5270 indices have been corrected for NSAR, while the $H\beta$ indices have been corrected for NSAR and emission. Tracks of constant age are denoted by solid lines, with ages, increasing from top to bottom, of 1.00, 2.00, 3.16, 5.01, 7.94 (shown in bold), 12.02, 15.13, 17.38, and 19.05 Gyr. Tracks of constant metallicity are denoted by dashed lines, with $[Fe/H]$, increasing from left to right, of -0.7, -0.4, 0.0 (shown in bold), and +0.4. The average $\pm 1\sigma$ error bars for the observed indices are shown in the lower left corner. M32 is plotted for reference as a solid square. The units of the axes, and indeed all Lick indices in subsequent plots, are in \AA . Line ratios used in other plots are of course unitless.

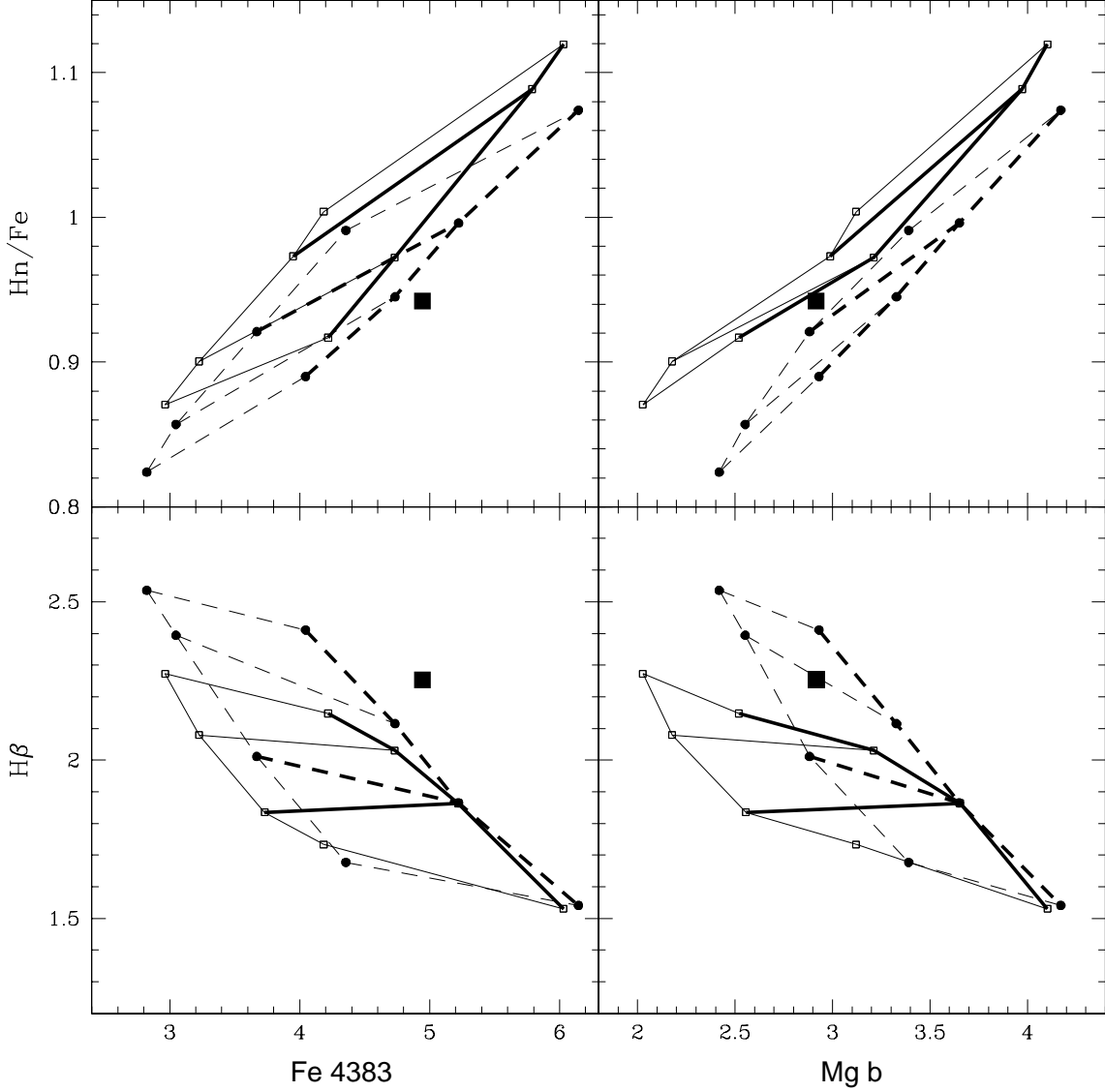


Fig. 3.— A comparison between the grids formed from the W94 models used here (solid lines), and the Vazdekis et al. 2001b models (dashed lines). Shown are grids for 4 line indices: Hn/Fe , $H\beta$, $Mg\ b$, and $Fe\ 4383$. The grid points in age occur at 15.13, 7.94, 5.01 and 3.12 Gyr; in metallicity they occur at -0.4 and 0.0. Bold lines show the solar abundance line, and the 7.94 Gyr age line. The index values for M32 are plotted as squares. The left two panels show good agreement, while the panels on the right with $Mg\ b$ have some discord.

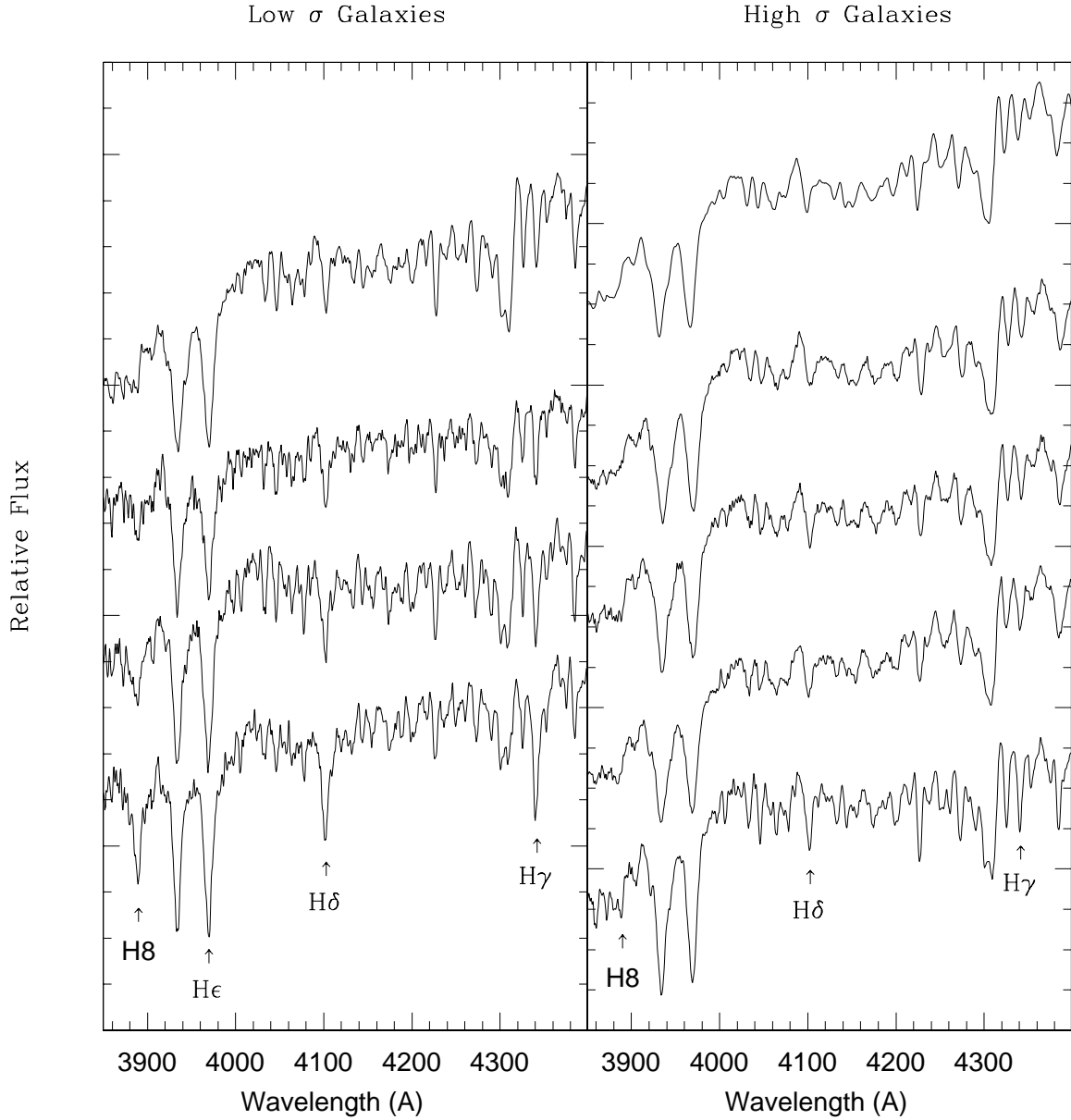


Fig. 4.— Representative spectra of low- σ (left panel) and high- σ (right panel) galaxies are plotted, at their observed broadenings. The effect of increasing Balmer line strength can be seen by looking from top to bottom in the panels. The effect of increased line broadening can be seen by comparing the lowest two galaxies in the right panel. The increase in Balmer strength is more pronounced in the low- σ galaxies. The spectra plotted in the left hand panel are of, from top to bottom, NGC 770, VCC140, VCC523, and VCC1912. In the right hand panel the spectra are of, from top to bottom, VCC685=NGC 4350, NGC 821, NGC 938, NGC 2954, and VCC1475.

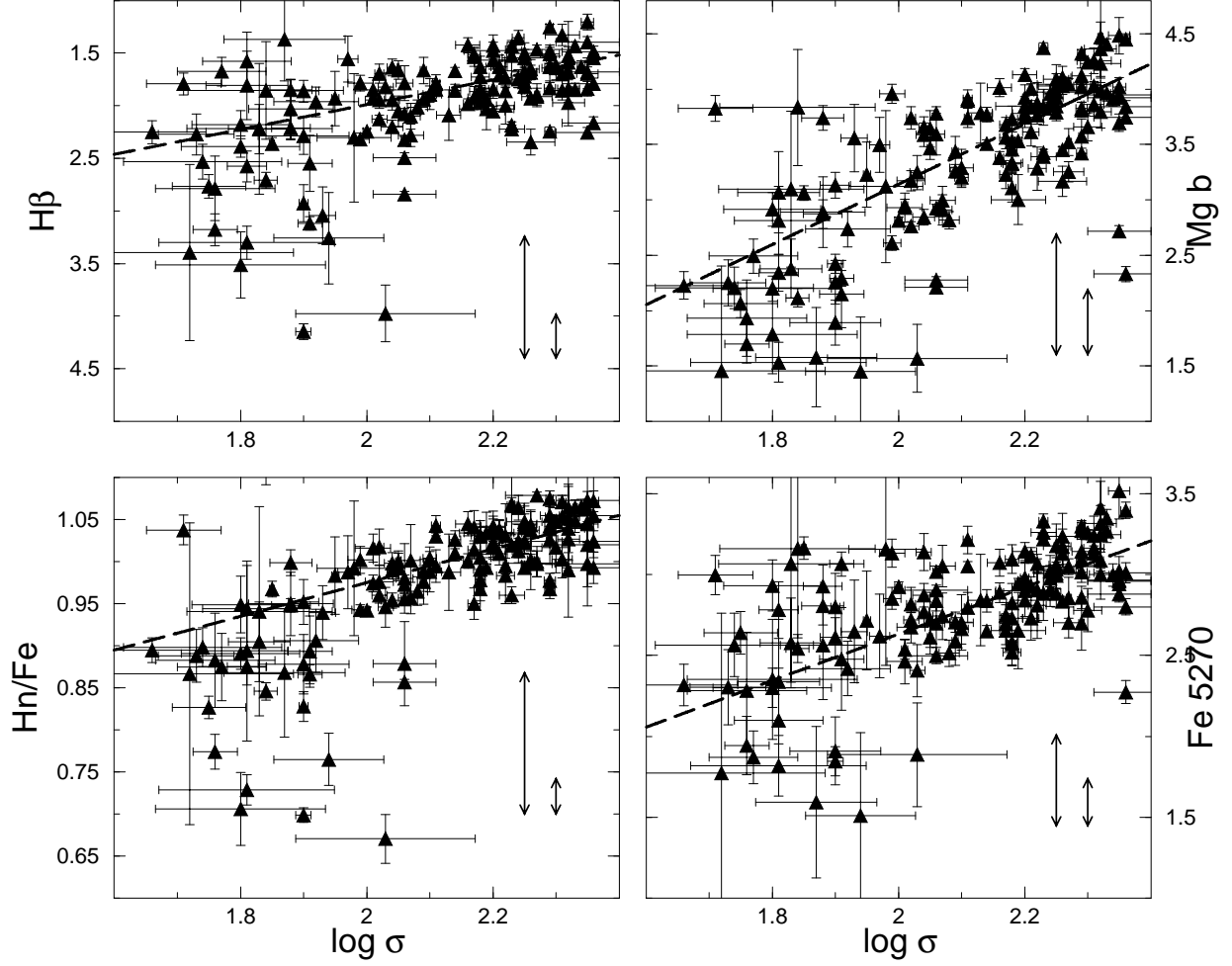


Fig. 5.— Four spectral indices are plotted versus $\log \sigma$. All indices have been emission corrected, and all except the Hn/Fe index have been NSAR corrected. Note that the vertical axis of the H β plot has been inverted to mirror the relation in the other three indices. The long-dashed line is the BCES regression fit to the data with $\log \sigma > 2.0$, excluding outliers. The vertical arrows in the lower right corner of each panel is a representation of the measured intrinsic scatter in the high σ galaxies ($\log \sigma > 2.0$, right) and the low σ galaxies ($\log \sigma < 2.0$, left).

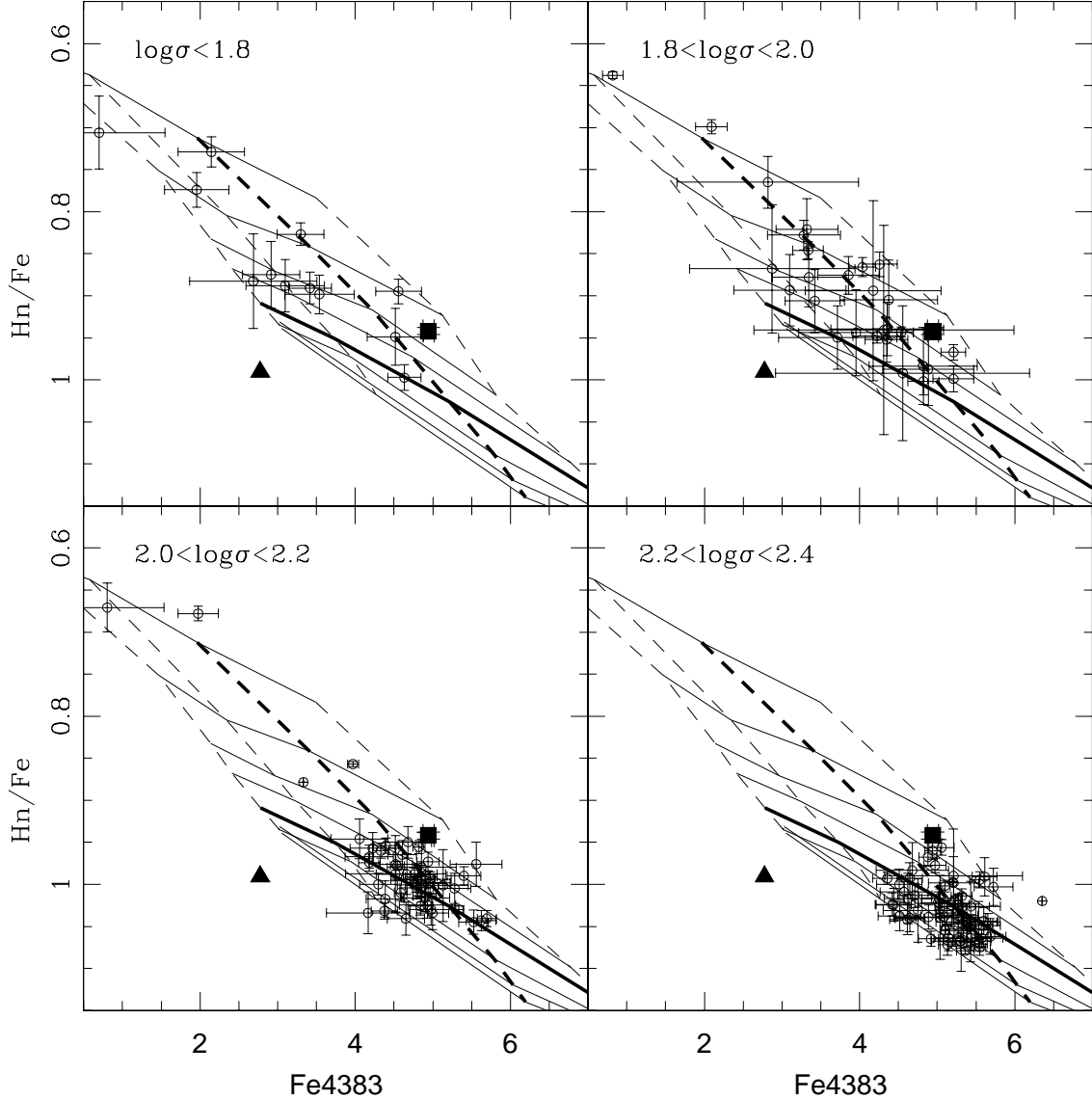


Fig. 6.— The Lick Fe4383 index is plotted versus the Hn/Fe index for all galaxies in our sample with $\sigma \leq 230 \text{ km s}^{-1}$. Note that *low* values of Hn/Fe indicate strong Balmer line strength relative to the neighboring metal lines. The galaxies have been subdivided into four different velocity dispersion bins in the four panels of the Figure. The large square denotes the elliptical galaxy M32, while the large triangle denotes the globular cluster 47 Tuc. The grid lines connect the simple stellar populations from the Worthey models of various ages and metallicities. Solid lines connect models of constant age; the ages (in Gyr), from top to bottom, are: 1.00, 2.00, 3.16, 5.01, 7.94 (shown in bold), 12.02, 15.13, 17.38.. Dashed lines connect models of constant metal-abundance; the [Fe/H] values, from left to right, are: +0.4, 0.0 (shown in bold), -0.4, and -0.7. The galaxy data for this plot have been corrected for emission only.

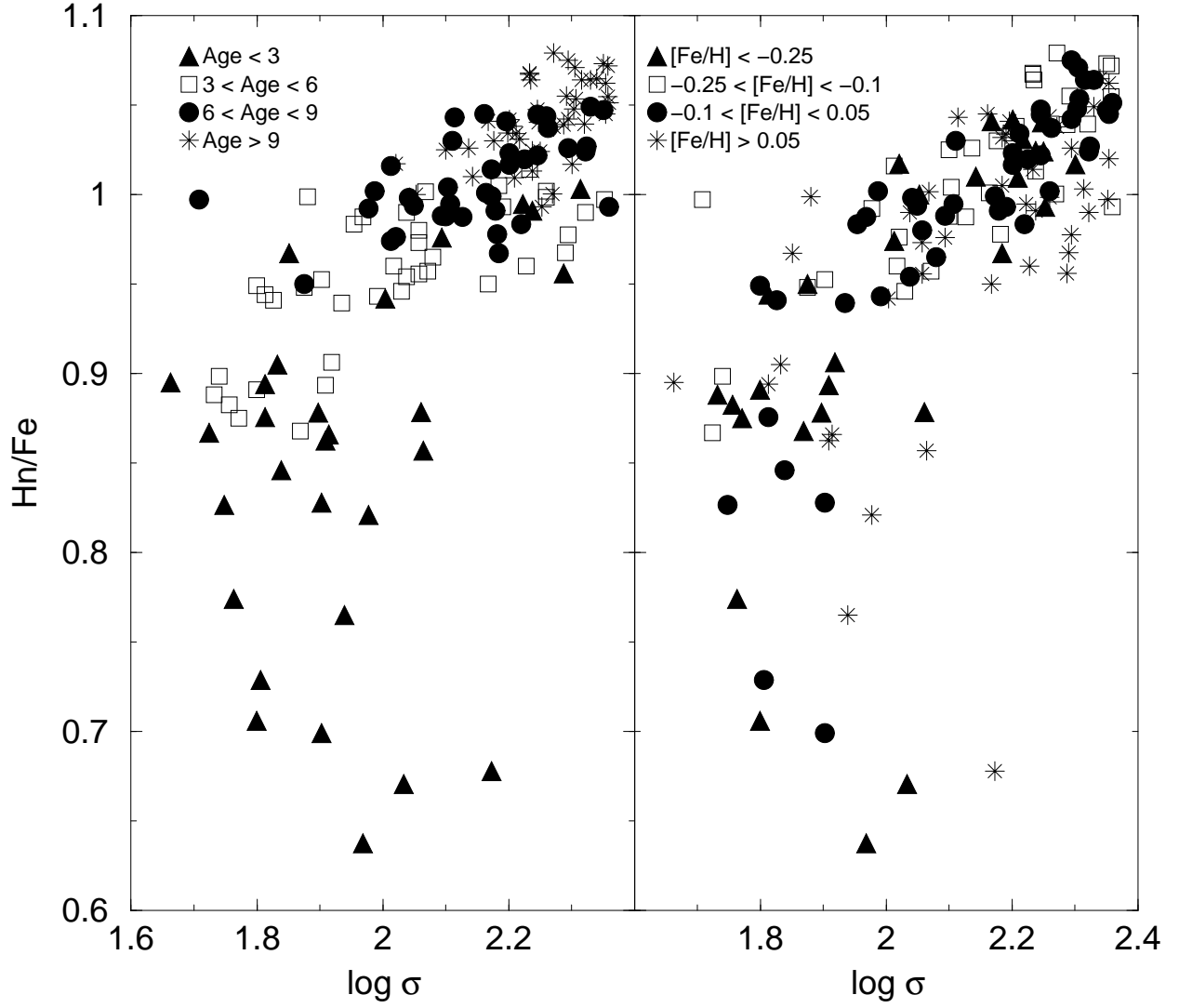


Fig. 7.— The derived ages of galaxies in the Hn/Fe - $\log \sigma$ diagram. The left panel shows galaxies coded by age intervals. In the right panel, the coding is by $[Fe/H]$.

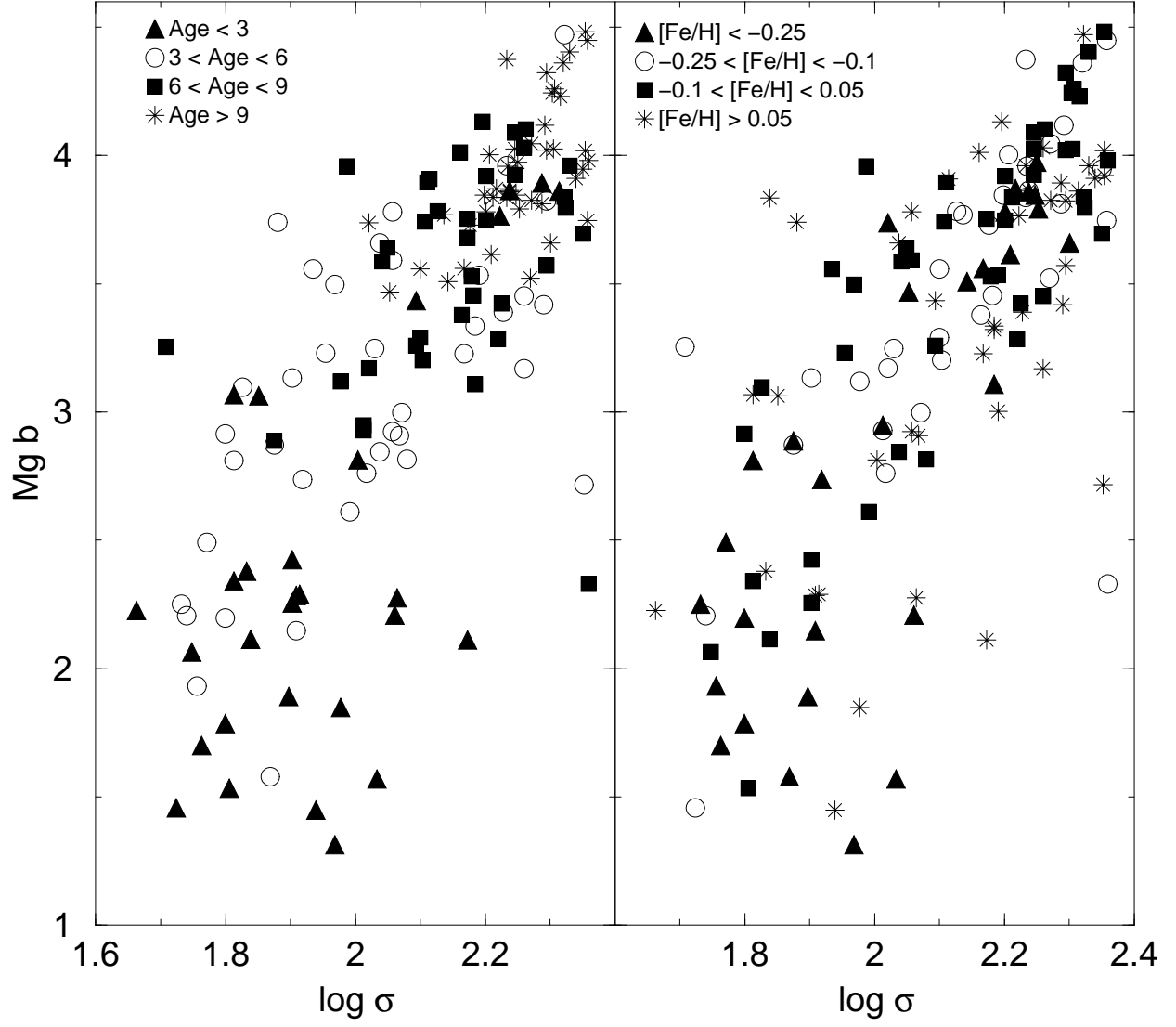


Fig. 8.— The derived ages of galaxies in the $\text{Mg } b$ - $\log \sigma$ diagram. The symbols are the same as in Fig. 7

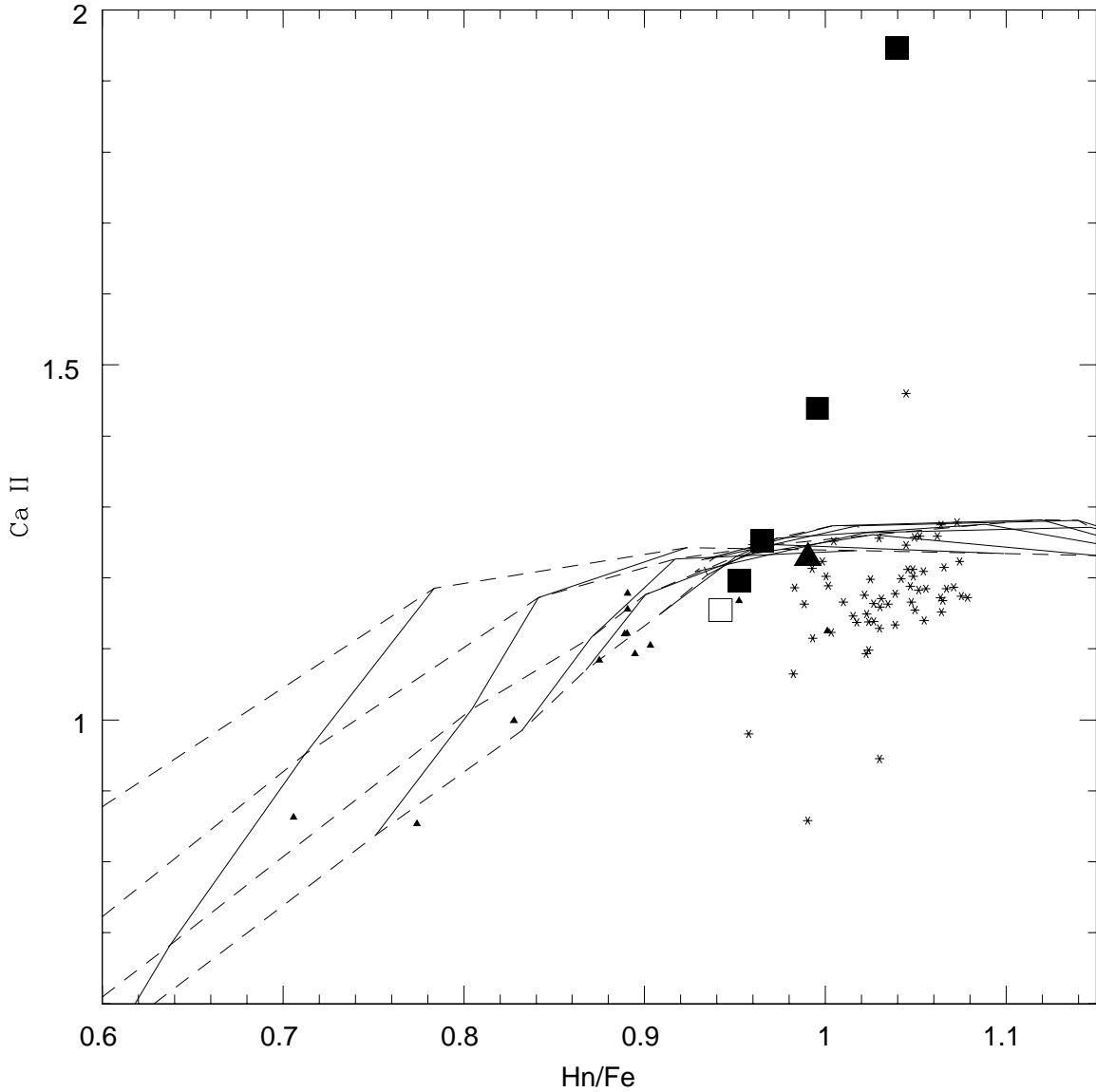


Fig. 9.— The Ca II index is plotted against the Hn/Fe index. The highest and lowest σ galaxies are plotted as small asterisks and filled triangles, respectively. M32 and 47 Tuc are plotted as a large open square and a large filled triangle, respectively. The filled squares, at increasing distance from M32, represent the resultant indices when the spectrum of M15 is subtracted from that of M32 with contributions of 5%, 10%, 20%, and 30% at 4000 Å. See text for details. The grid lines connect the simple stellar populations from the Worthey models of various ages and metallicities. Solid lines connect models of constant age; while dashed lines connect models of constant metal-abundance. Note that both axes place the strong Balmer absorption at low index values, and are plotted in the same manner as in our previous papers that used these indices.

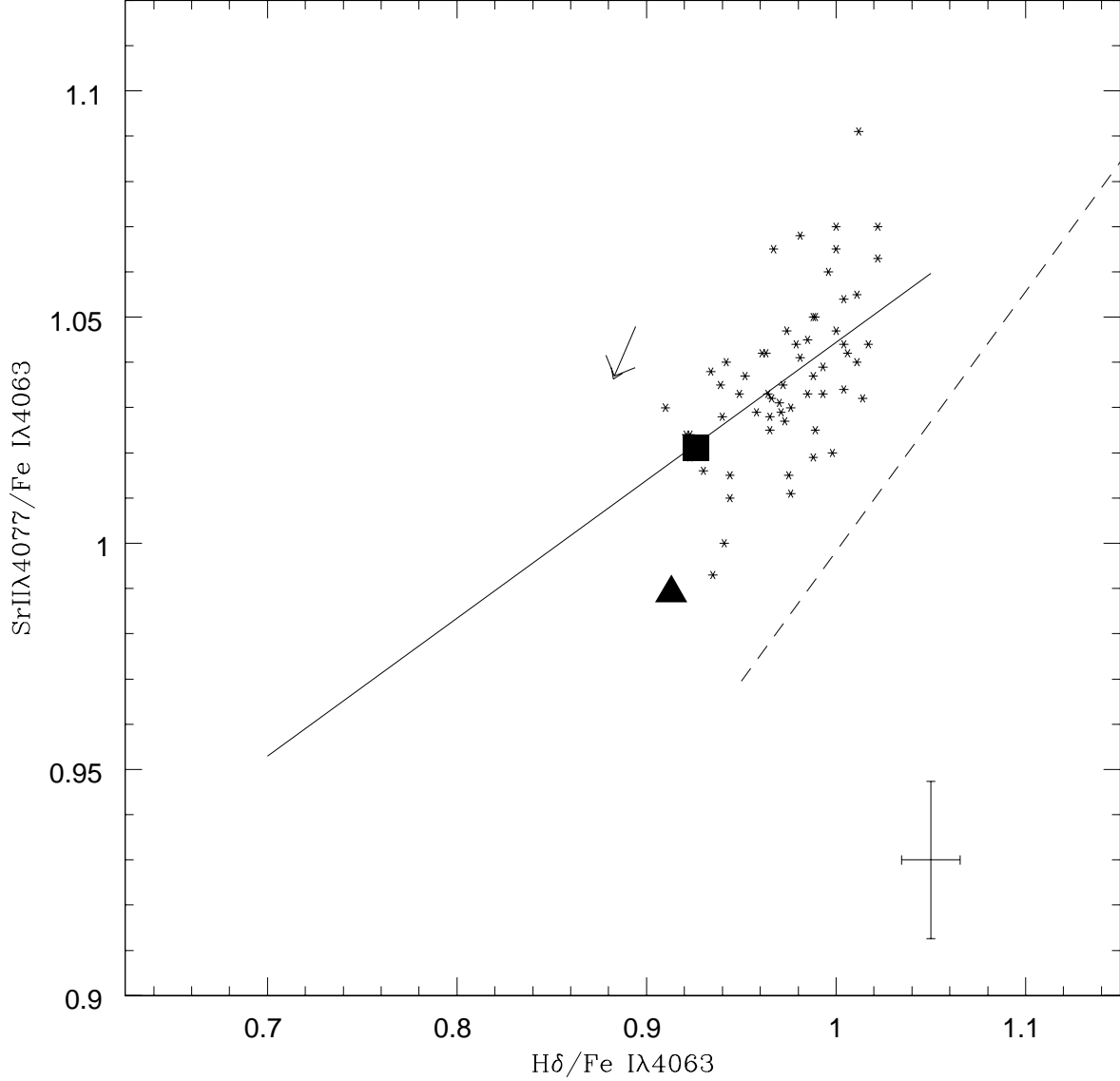


Fig. 10.— The SrII4077/FeI4063 index is plotted versus the H δ /4063 index. High- σ galaxies are plotted as small asterisks, while M32 and 47 Tuc are plotted as a large filled square and triangle, respectively. The solid line represents the mean relation for dwarf stars, while the dashed line represents the mean relation for giants. The left arrow indicates the direction of correlated errors in the plot. The error bars in the lower right corner indicate the average $\pm 1\sigma$ errors in the galaxy indices. Note that the lower values of the Balmer sensitive H δ /4063 index, as well as the gravity sensitive index SrII4077/FeI4063 indicate early stellar spectral types. The diagram is plotted in the same manner as previous papers.

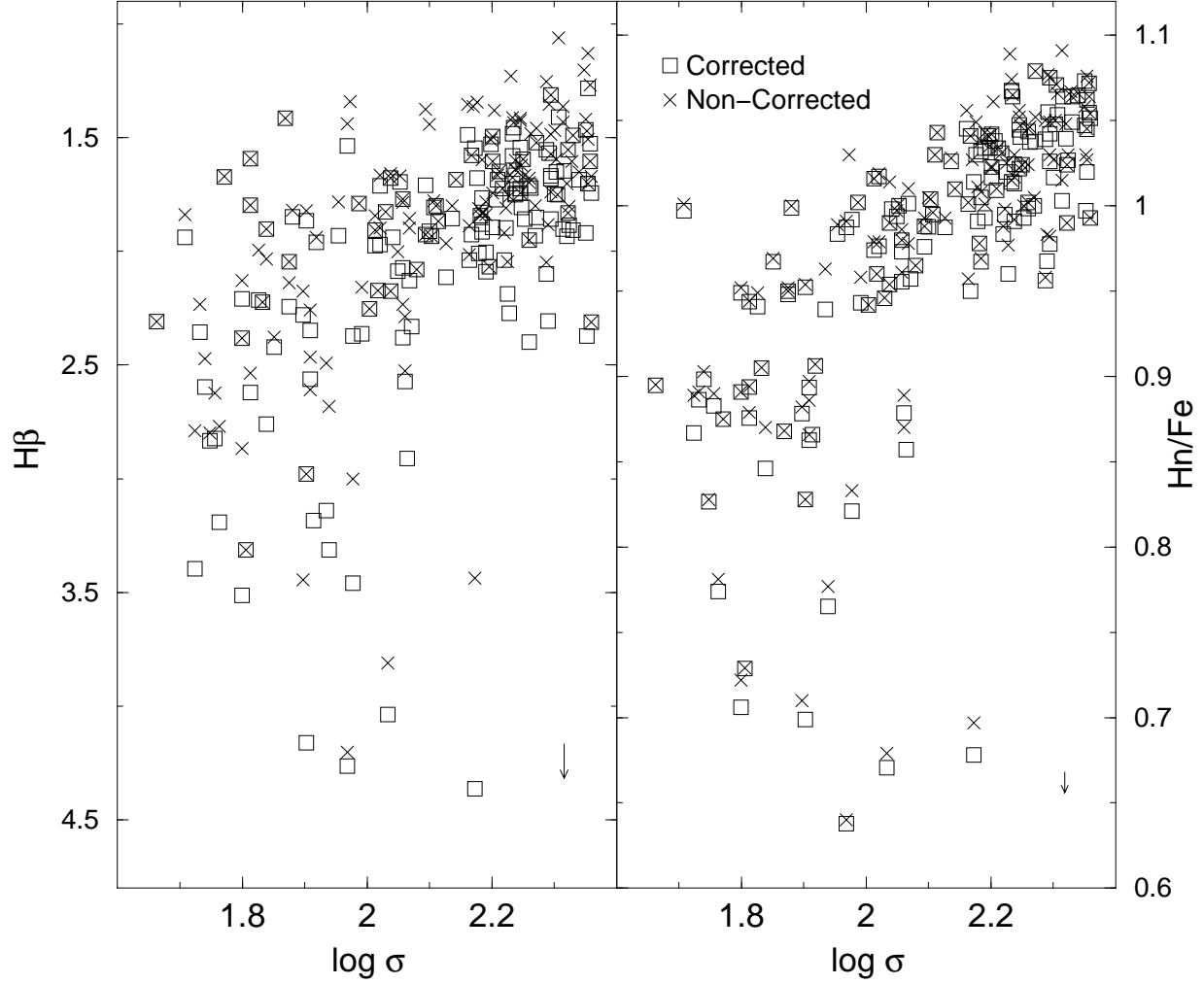


Fig. 11.— The effects of correcting the spectral indices for emission fill-in, shown for two Balmer line indices, the Lick $H\beta$ index (left panel, note that $H\beta$ is plotted so that strong absorption is at the bottom) and the Hn/Fe line ratio index (right panel), both plotted versus $\log \sigma$. The original index values are shown as x's and the corrected values are shown as open squares. The mean index corrections are 0.15 for $H\beta$ and 0.012 for Hn/Fe , and are denoted by arrows in the lower right corners of the panels.

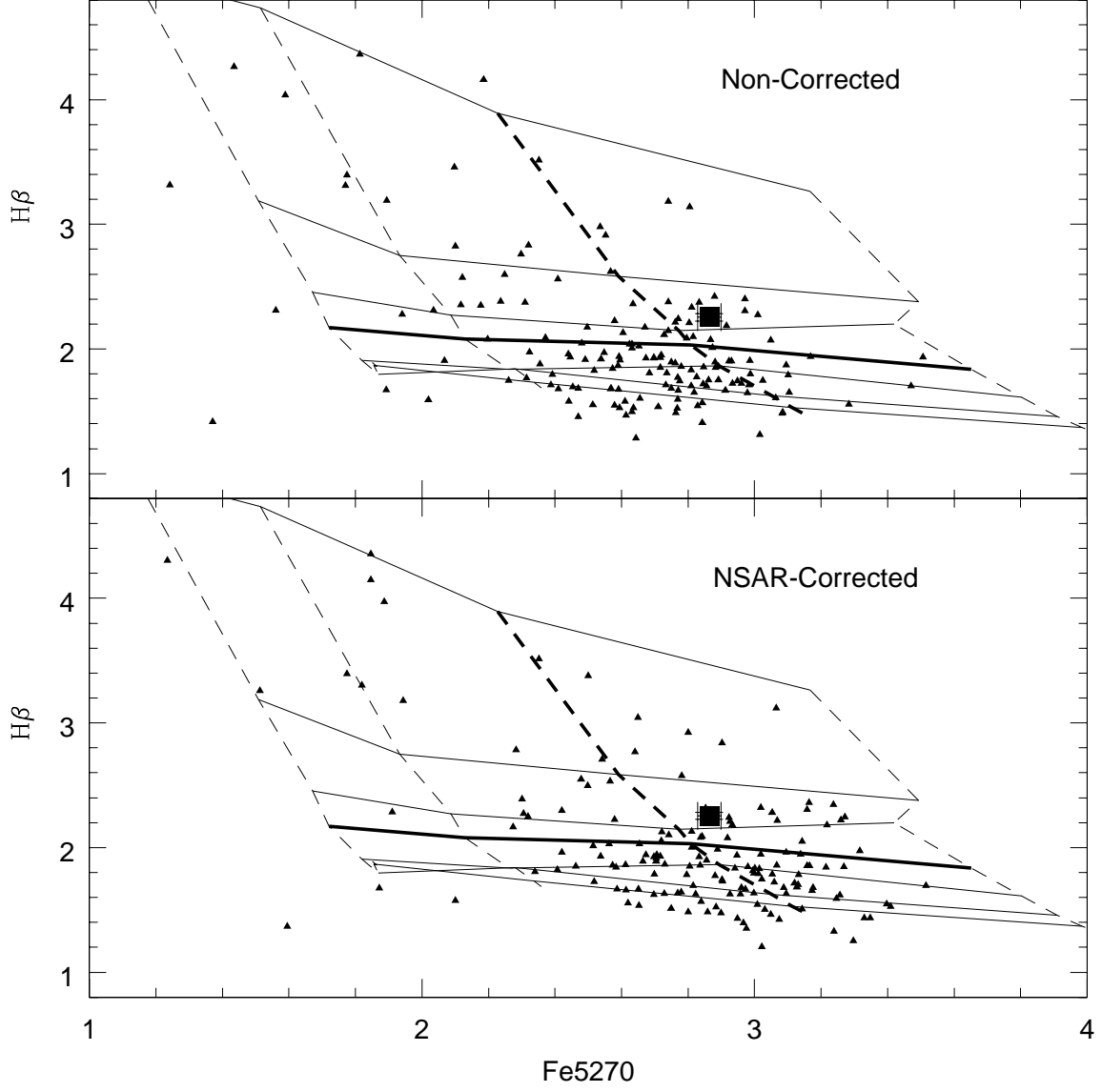


Fig. 12.— The effects of correcting the $H\beta$ and Fe5270 indices for NSAR. The upper and lower panels show the galaxy data (filled triangles) before and after NSAR corrections, respectively. In both panels the data have already been corrected for emission. The large square with error bars represents M32. The lines of constant age and metallicity are the same as in Fig. 6.

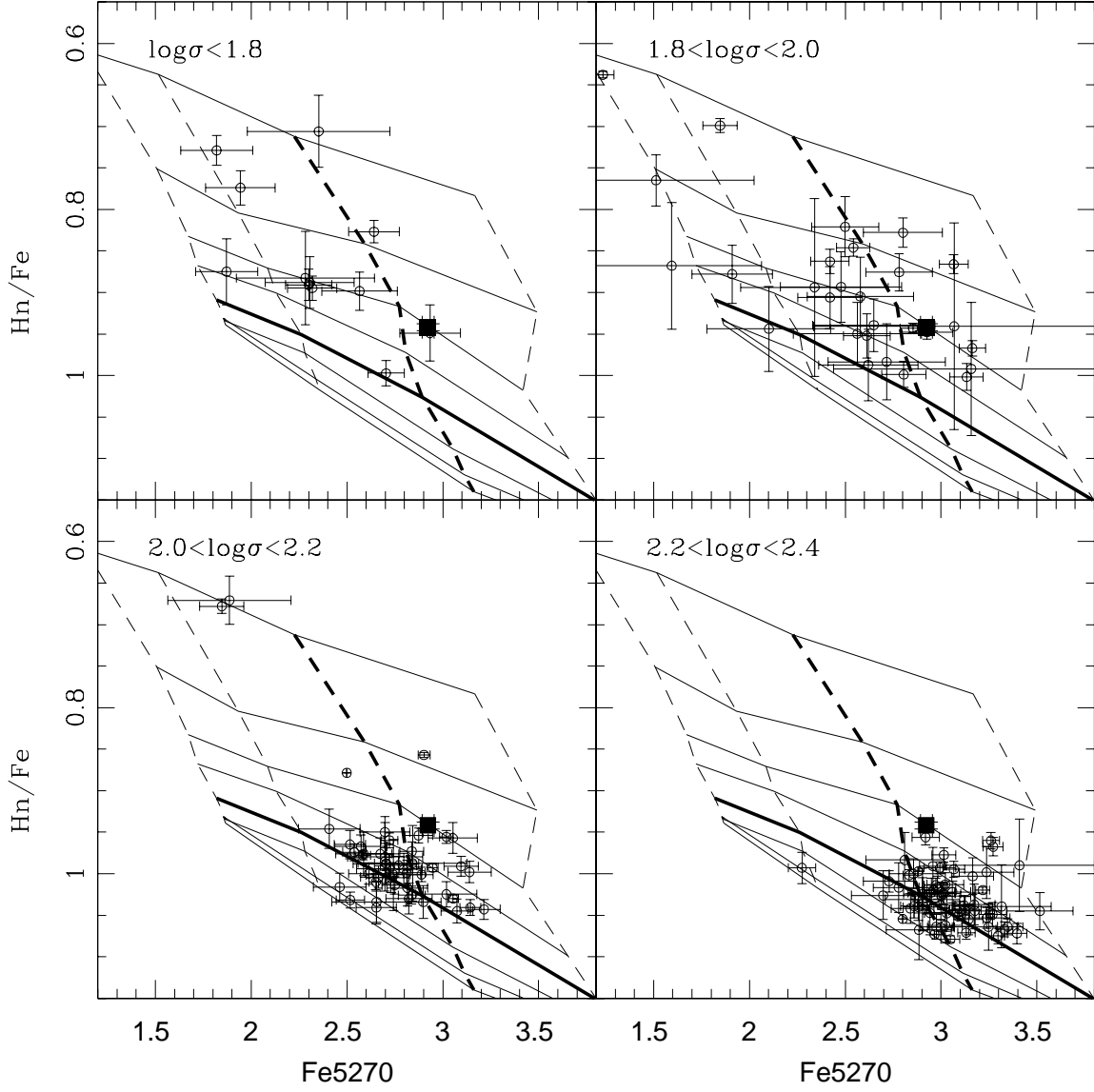


Fig. 13.— The emission corrected Hn/Fe Balmer line index is plotted versus the Lick Fe5270 index (which has been NSAR corrected). Symbols and grid lines are the same as in Fig. 6.

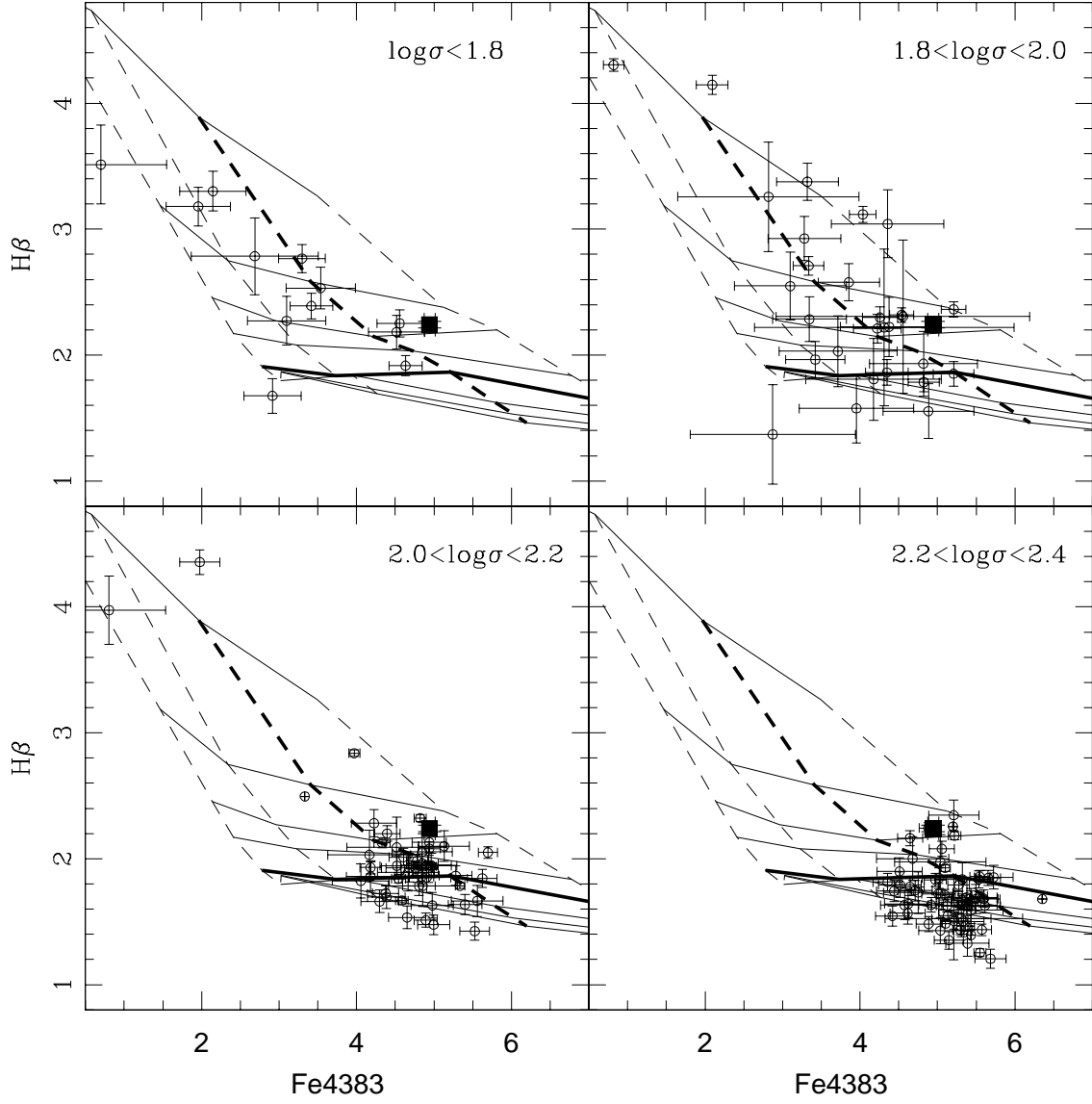


Fig. 14.— The Lick $H\beta$ index is plotted versus the Lick Fe4383 index. $H\beta$ has been corrected for NSAR and emission. Symbols and grid lines are the same as in Fig. 6.

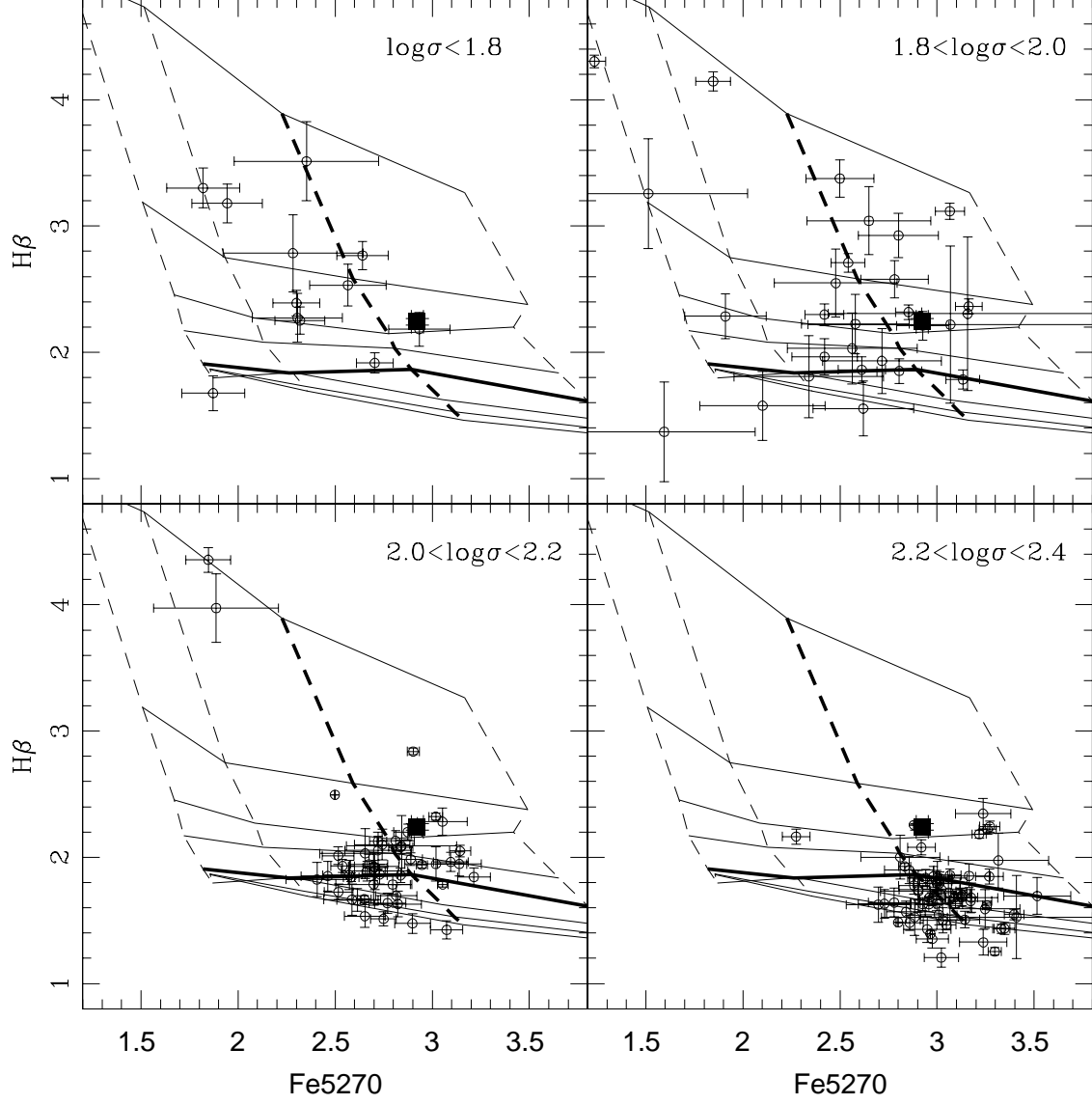


Fig. 15.— The Lick $H\beta$ index is plotted versus the Lick Fe5270 index. $H\beta$ has been corrected for emission, and both indices have been NSAR corrected. Symbols and grid lines are the same as in Fig. 6.

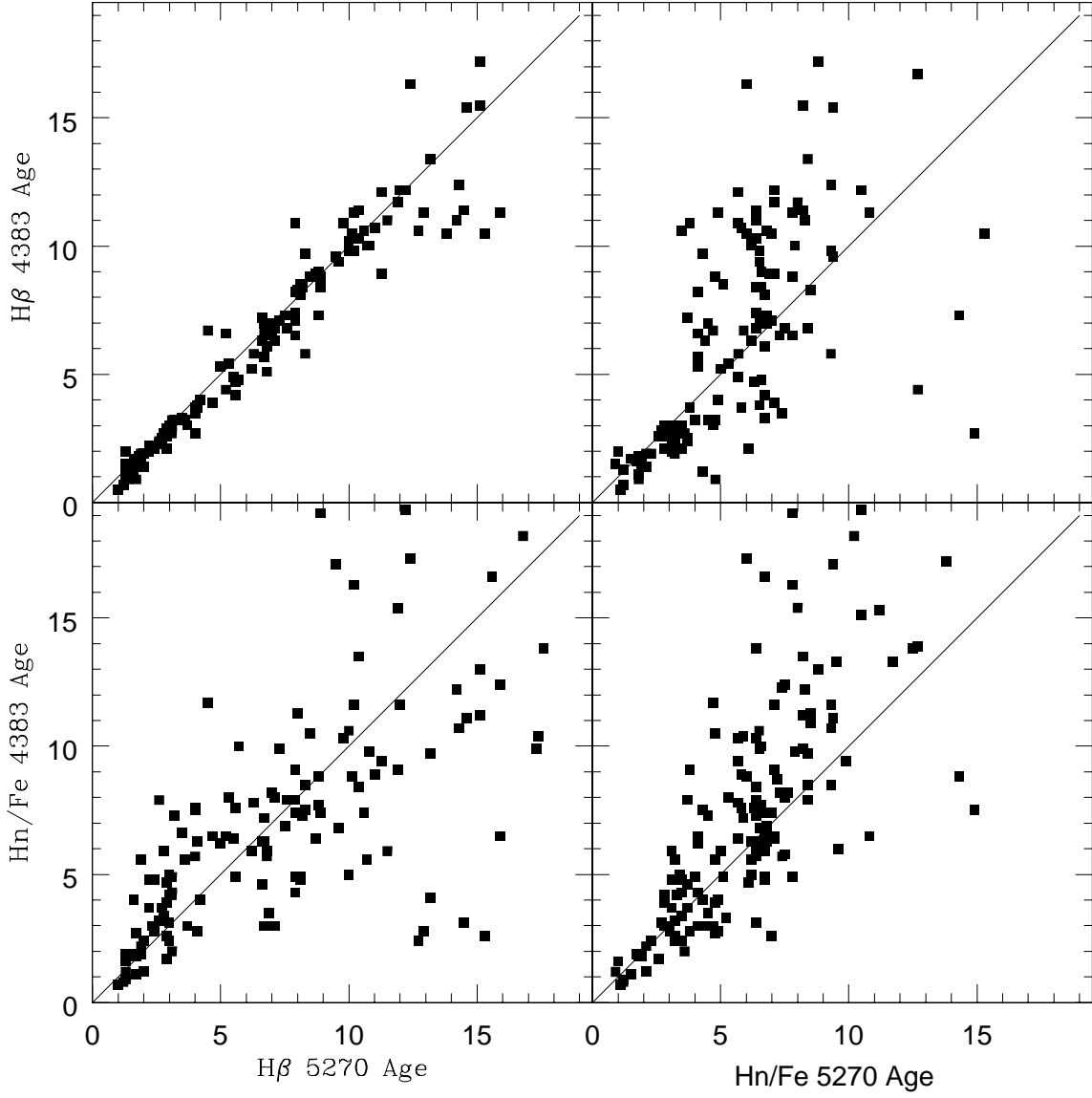


Fig. 16.— A comparison is made between the derived ages for our galaxy sample from four different model grids. The unity line is shown as a visual aid.

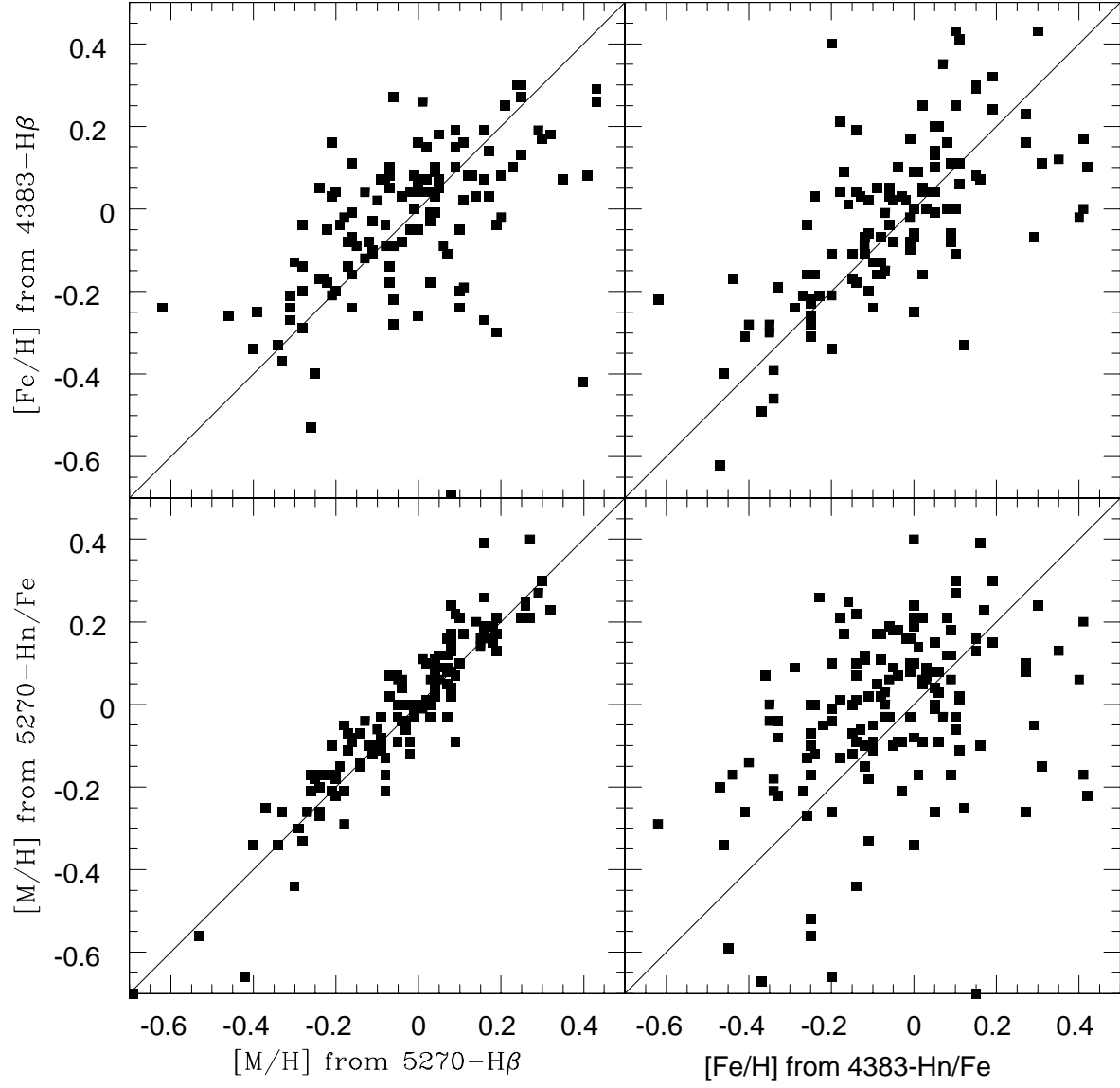


Fig. 17.— A comparison is made between the derived metallicities for our galaxy sample from four different model grids. The unity line is shown as a visual aid.

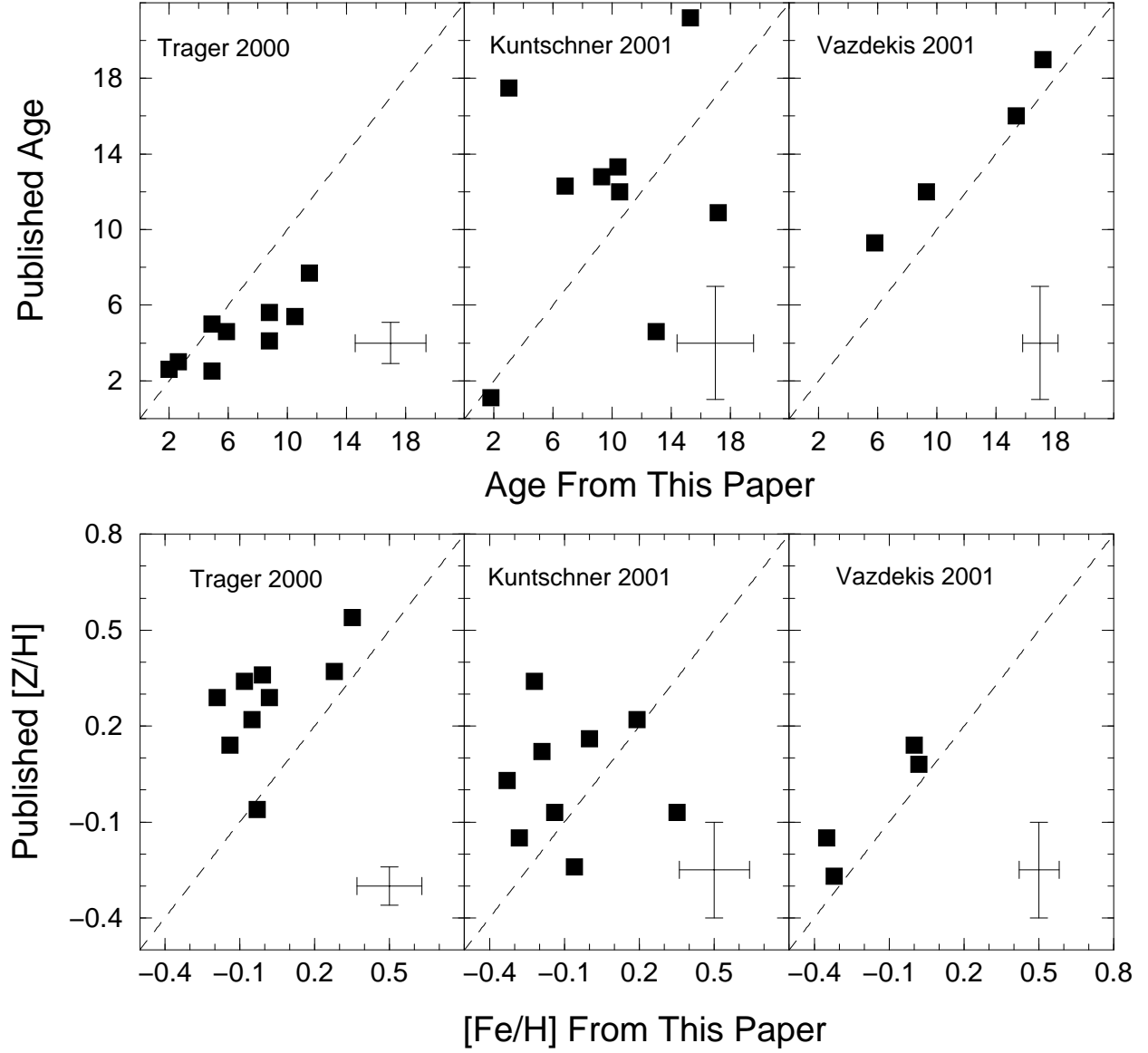


Fig. 18.— A comparison of our derived ages and metallicities to determinations from the literature. Mean errors *for the specific data plotted* are shown as an error cross in the lower right corner of each plot. The unity line appears as a dashed line. The same age and $[\text{Fe}/\text{H}]$ scale applies in all panels.

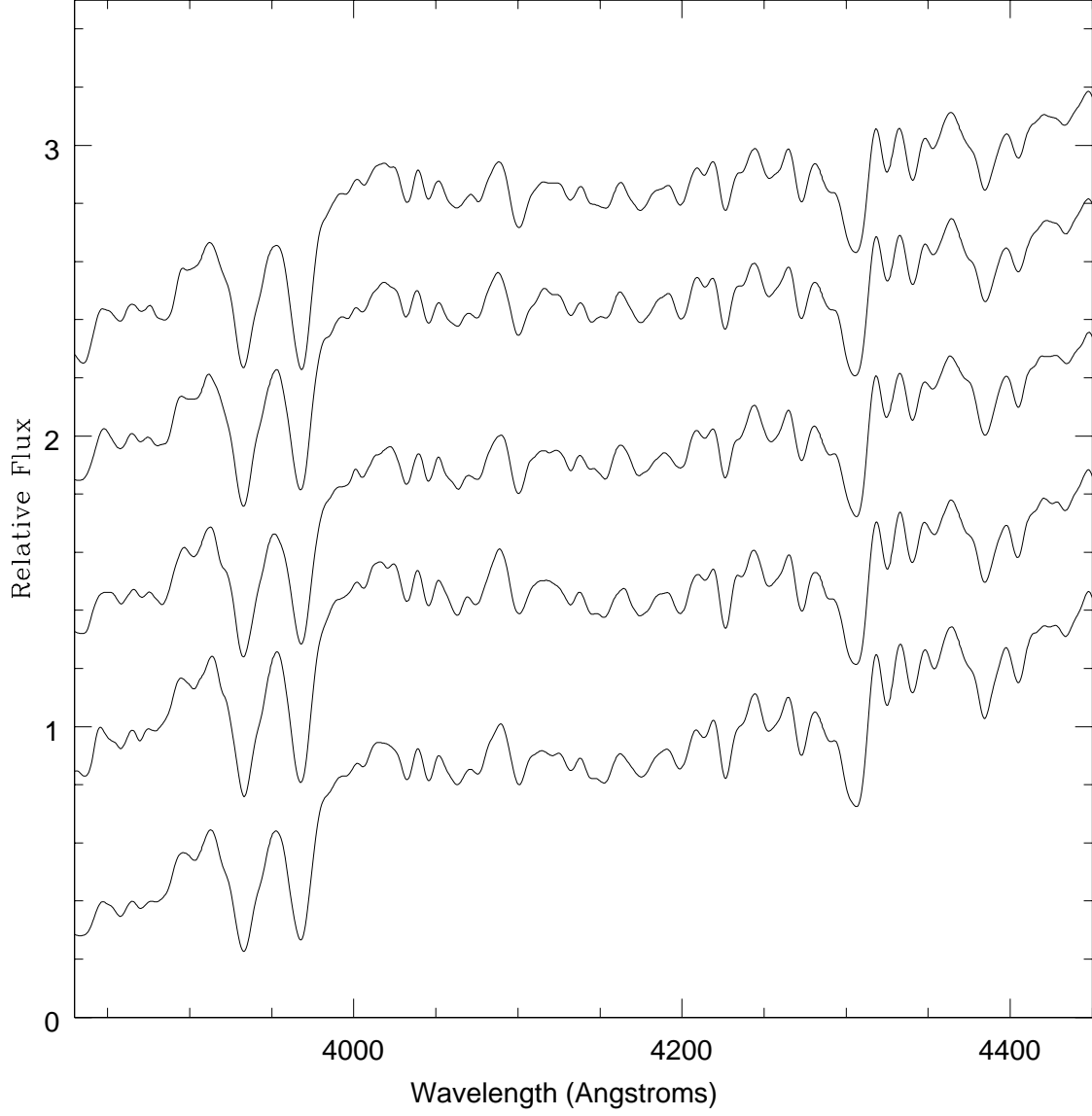


Fig. 19.— The spectra of five high- σ galaxies are plotted to show the correlated trend in all Balmer lines from older to younger galaxies. Plotted from top to bottom are: NGC 7611, NGC 7612, NGC 2954, NGC 821, and NGC 4442 (VCC1062), which have ages of 2.8, 2.8, 3.9, 11.6, and 12.3 Gyr respectively.

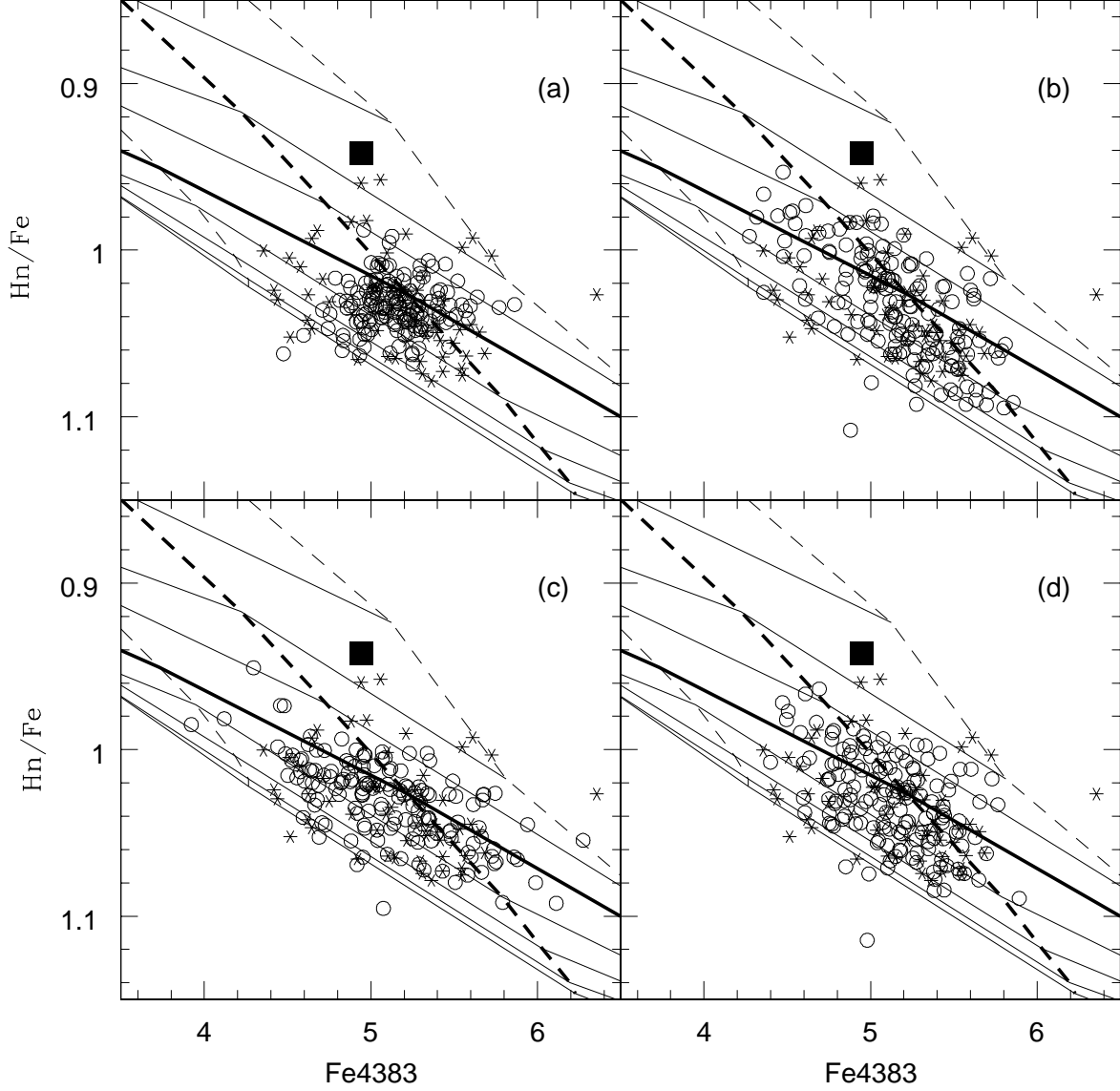


Fig. 20.— The observational data for the high- σ galaxies (asterisks) are plotted along with simulated observations (open circles) in the Fe4383 versus Hn/Fe diagram. The solid and dashed lines indicate the grid of Worthey models, and the large square represents M32. An additional age line is shown here, at 19.05 Gyr. In panel (a) we have only included the known $\pm 1\sigma$ observational errors in producing the simulated galaxy points. In panels (b) and (c) we have allowed for a $\pm 1\sigma$ scatter of 2 Gyr in age and 0.1 in $[\text{Fe}/\text{H}]$, respectively, along with the observational errors. In panel (d) we have simulated correlated errors in age and $[\text{Fe}/\text{H}]$. See text for details.

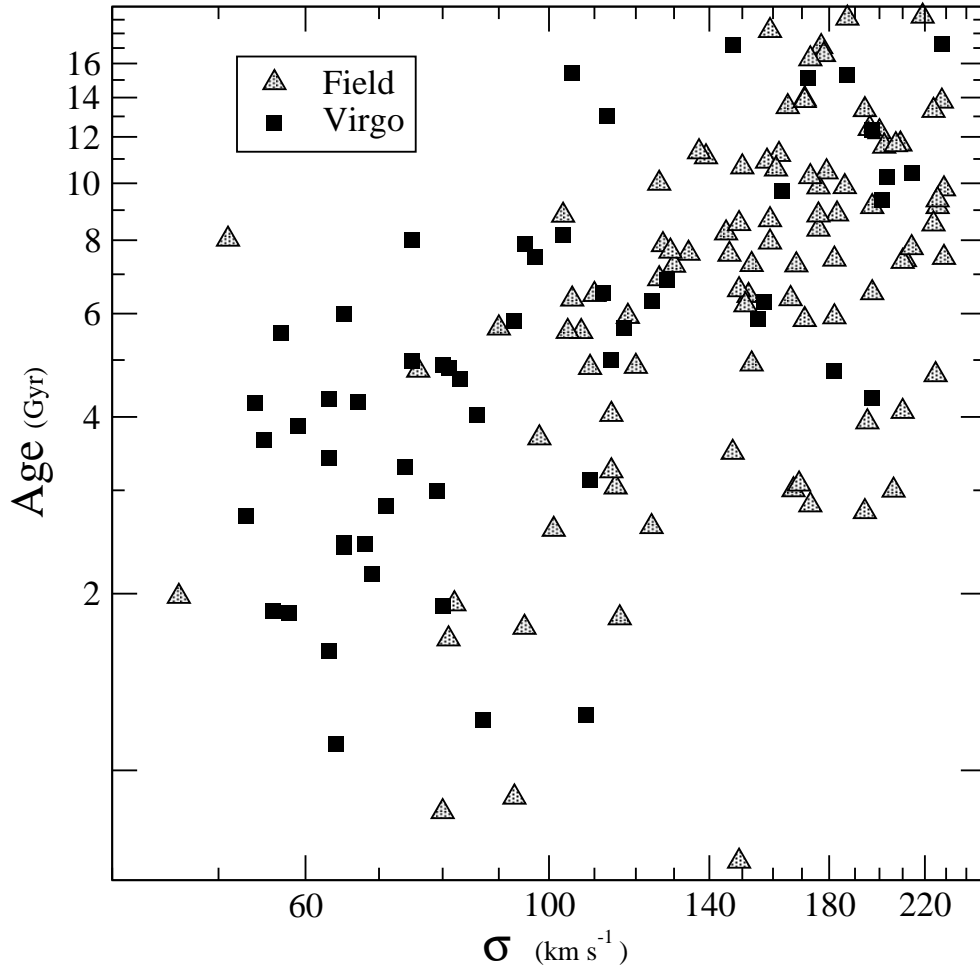


Fig. 21.— The age- σ diagram for all galaxies in the sample. The squares denote the Virgo galaxies; the triangles denote field galaxies.

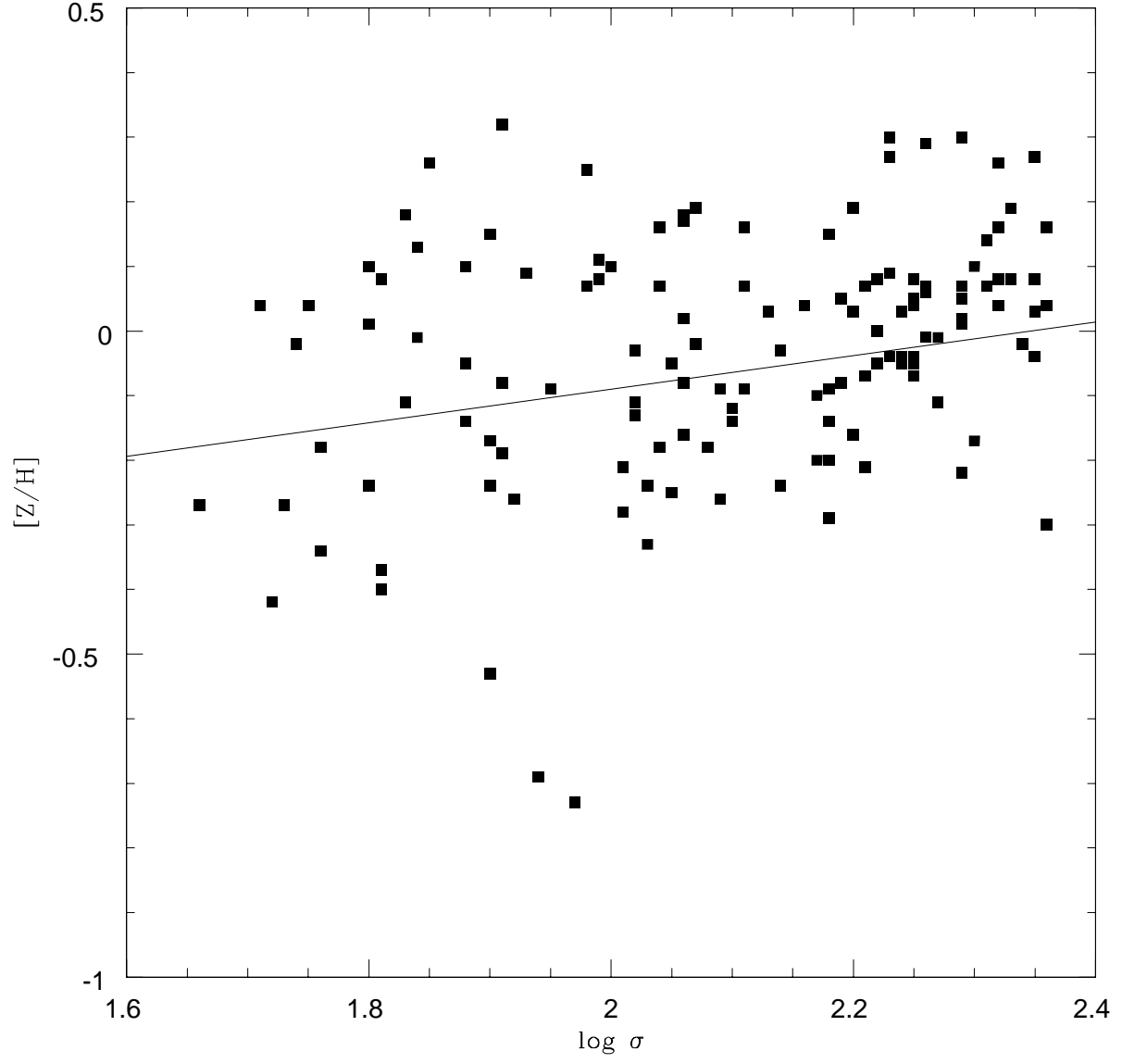


Fig. 22.— The $[Z/H]$ - $\log \sigma$ correlation for all galaxies in the sample. The $[Z/H]$ values have been determined from the Fe5270 versus $H\beta$ diagram, where both indices have been corrected for NSAR effects.

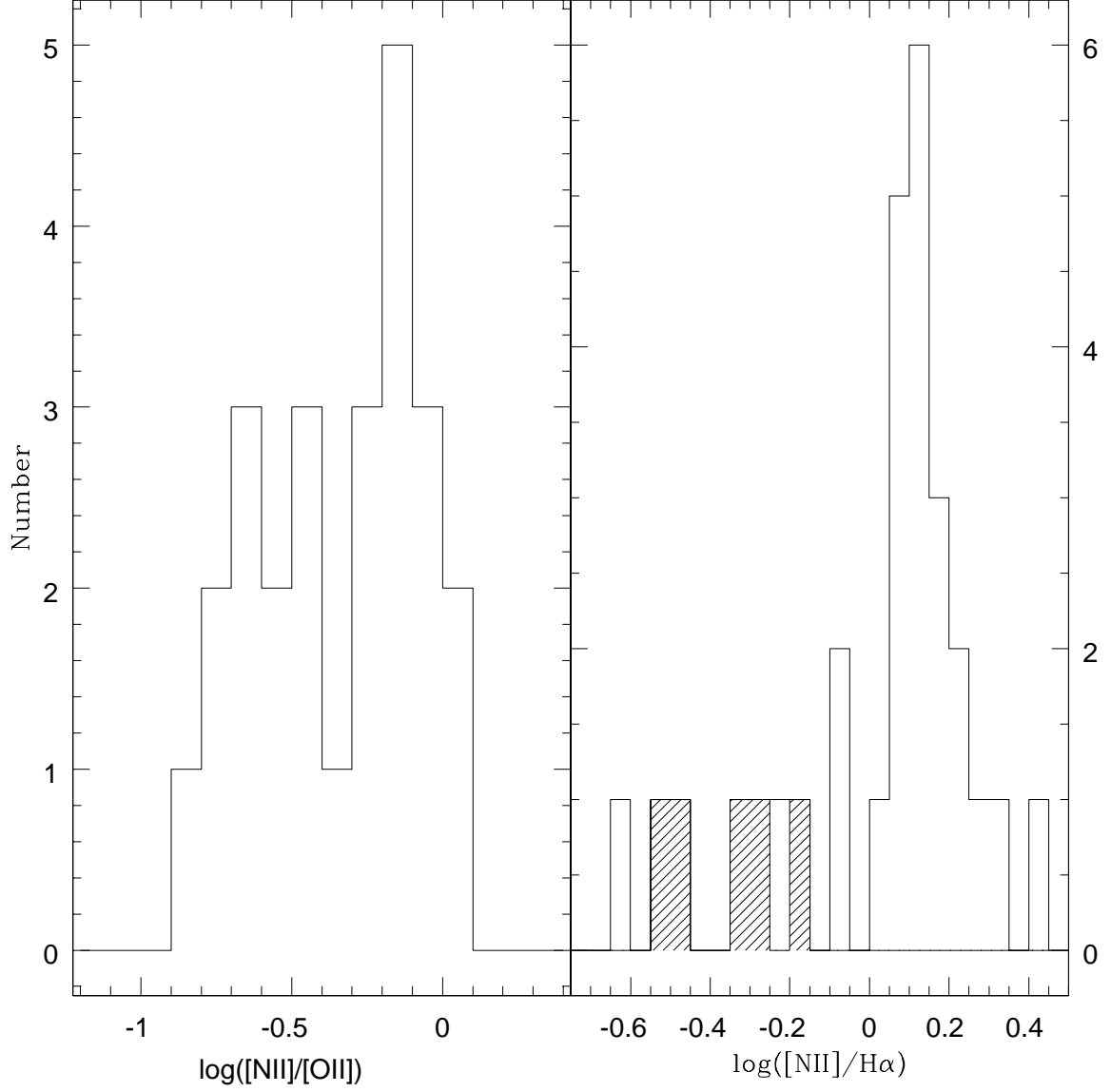


Fig. 23.— Histograms of the line ratio $\log([NII]/[OII])$ (left panel), and $\log([NII]\lambda 6584/H\alpha)$ (right panel) for those galaxies with measurable emission in their red spectra. In the right hand histogram, the shaded areas denote the low-luminosity Virgo galaxies; the open regions are higher mass galaxies.

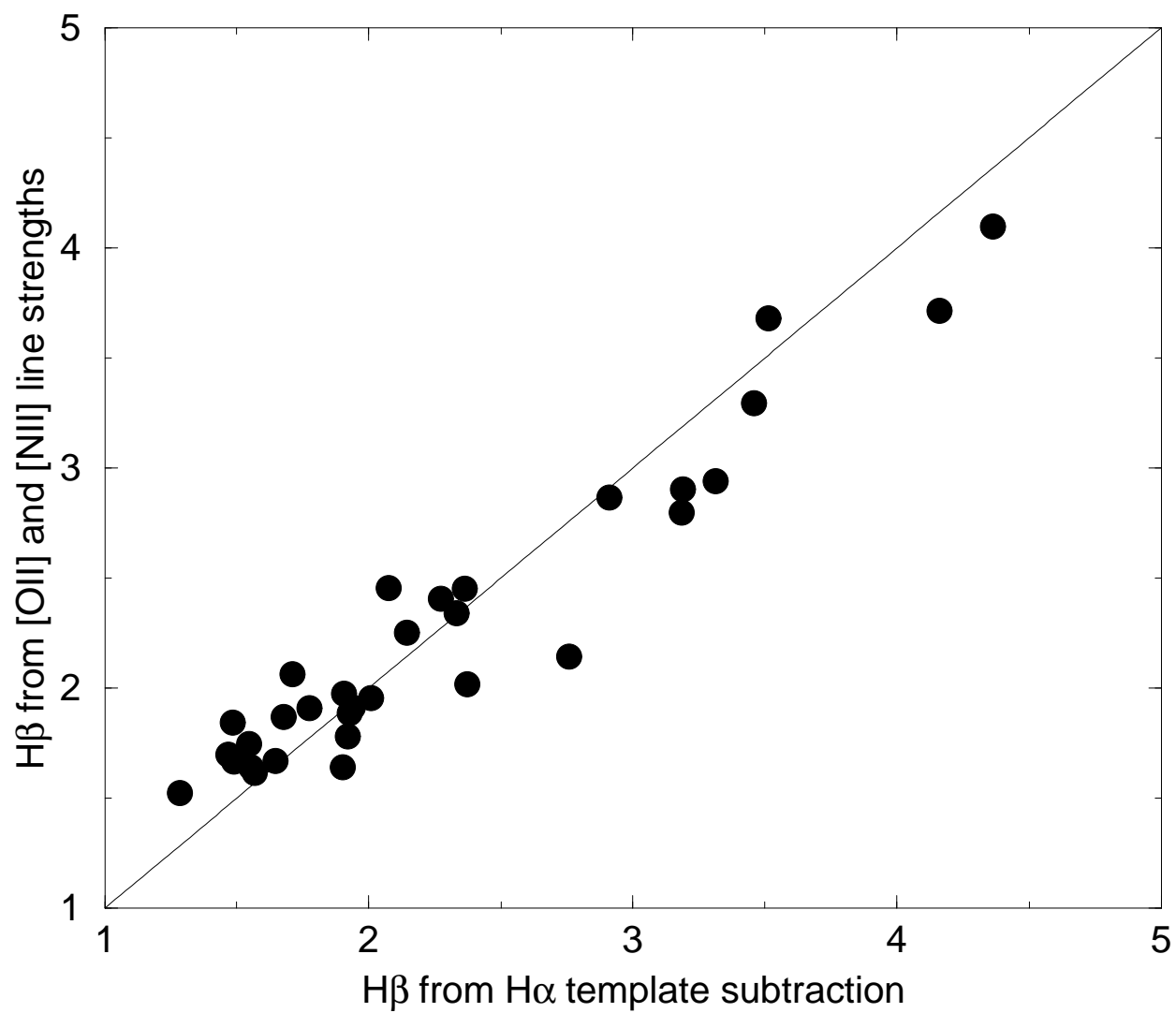


Fig. 24.— Comparison of H β corrections using the two different methods. The rms scatter is 0.2Å

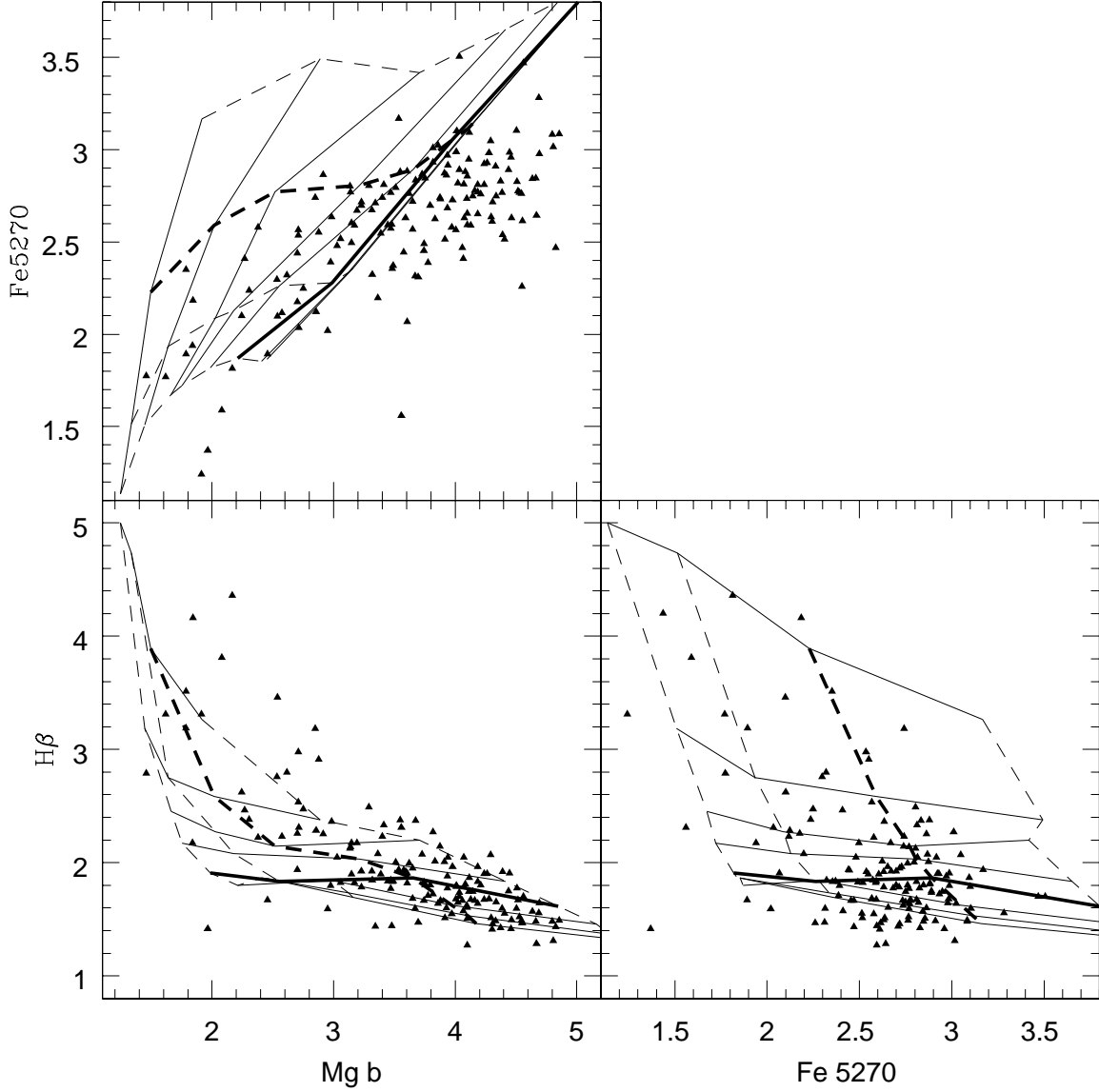


Fig. 25.— Three indices which suggest the overabundance of Mg in early-type galaxies. The age and metallicity contours are the same as in previous figures. Age increases from top to bottom in the two bottom panels, and increases from left to right in the single top panel. Metallicity increases from left to right in the two lower panels, and from bottom to top in the upper panel. The galaxy indices have been corrected for emission in H β but not for NSAR. Note that the Mg b index predicts younger ages and higher metallicities than the Fe index.

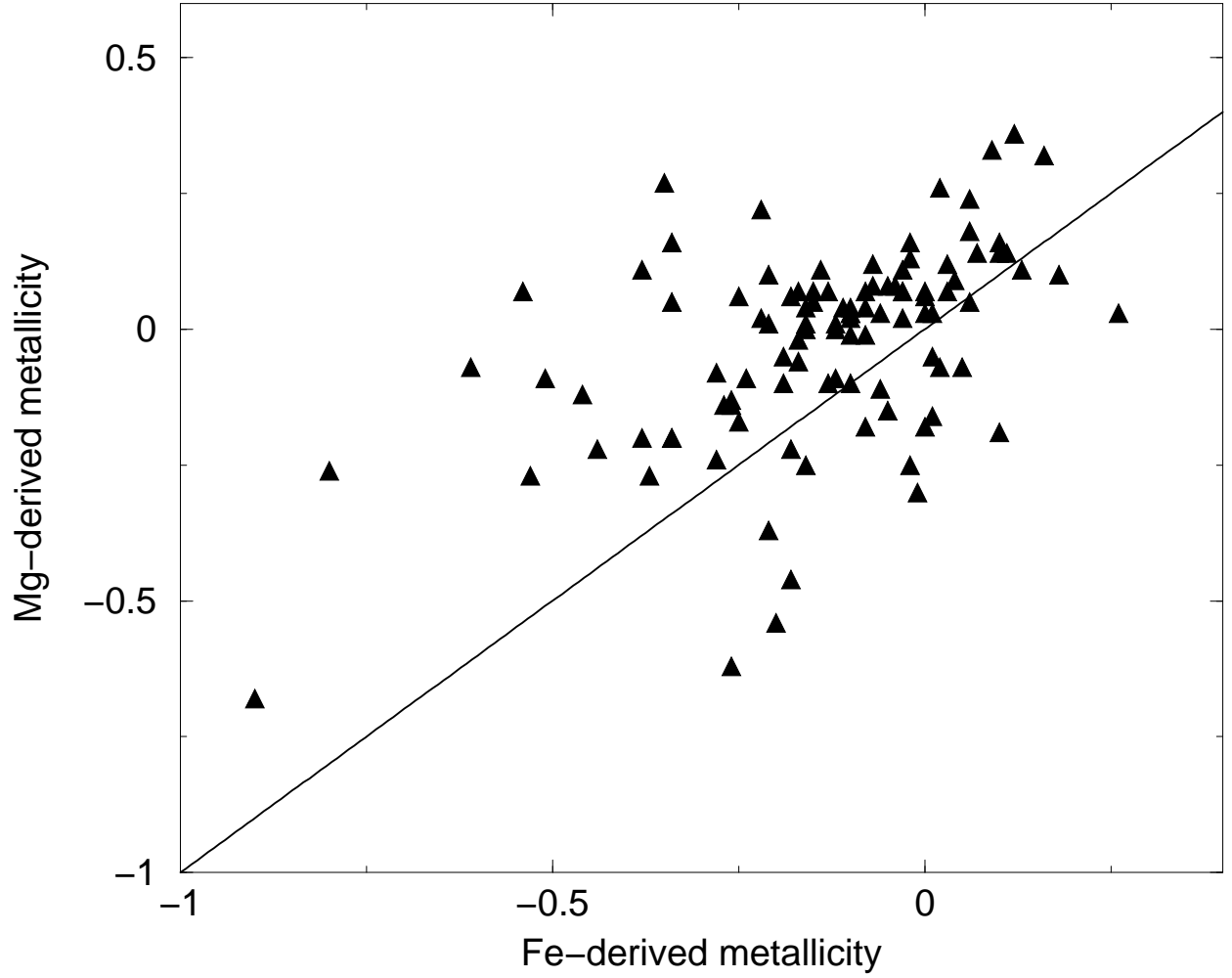


Fig. 26.— The comparison between the metallicity derived from the Mg b - $H\beta$ model grids and that derived from the Fe 5270- $H\beta$ model grids. In both cases we have derived the abundances from spectral indices that have *not* been corrected for NSAR. The solid line is the unity relation. The Mg b index tends to yield higher metallicity values.

Table 1. Log of Galaxy Observations

Name (1)	Alt-Name (2)	Env (3)	N (4)	S/N (5)	CZ_{meas} (6)	CZ_{err} (7)	CZ_{lit} (8)	σ_{meas} (9)	σ_{err} (10)	σ_{lit} (11)	Morph (12)	H α (13)
A00368+25	—	F	4	45	4675	26	4614	162	7	—	E	—
A10025+59	—	F	3	68	2916	23	2871	219	7	—	E	—
A15565+64	—	F	3	36	9260	32	9216	302	7	—	E	—
A15572+48	—	F	2	31	5990	66	6011	153	7	212	S0	—
A16044+16	—	F	2	42	11010	44	11015	229	7	216	S0+	u
A23174+26	—	F	4	37	5915	43	5864	240	7	—	S0	y
A23302+29	—	F	6	37	5555	34	5595	206	14	—	S0	y
IC0195	—	F	3	45	3675	43	3648	127	7	—	S0+	—
IC0555	—	F	3	29	6733	35	6732	211	8	—	S0	—
IC0598	—	F	1	17	2246	10	2258	115	7	—	S0	—
IC1153	—	F	3	44	6017	24	5879	224	7	—	S0	y
IC1211	—	F	4	28	5475	20	5563	209	12	—	E	—
IC2382	—	F	3	60	6033	41	6139	282	7	—	—	—
M32	NGC221	LG	8	166	-222	16	-145	100	7	79	E	—
NGC183	—	F	4	57	5289	64	5402	177	7	—	E	—
NGC205	—	LG	2	71	-243	44	-241	93	7	97	dE	—
NGC311	—	F	3	51	5095	41	5065	263	7	286	S0	—
NGC380	—	F	3	48	4435	121	4426	261	9	275	E	n
NGC384	—	F	4	42	4844	31	4287	193	7	—	E	—
NGC448	—	F	2	31	1833	13	1917	103	7	90	S0	—
NGC474	—	F	3	53	2349	20	2372	159	7	169	S0+	u
NGC502	—	F	2	61	2570	17	2489	129	7	74	S0+	—
NGC516	—	F	3	32	2432	23	2432	46	7	—	S0	—
NGC525	—	F	4	46	2192	19	2146	105	7	—	S0	—
NGC584	IC1712	F	3	73	1834	27	1802	210	7	230	E	—
NGC636	—	F	2	46	1838	25	1860	176	7	166	E	—
NGC656	—	F	4	49	3806	43	3916	76	7	—	S0	u
NGC770	—	F	4	51	2482	31	2458	51	7	—	E	n
NGC774	—	F	4	48	4664	25	4595	173	7	—	S0	—
NGC821	—	F	2	81	1762	22	1735	202	7	207	E+	n
NGC938	—	F	4	60	4118	26	4099	186	7	—	E	—
NGC990	—	F	3	62	3476	54	3508	137	7	179	E	—
NGC1026	—	F	5	51	4142	74	4179	158	19	191	S0	n
NGC1029	—	F	3	41	3658	44	3635	145	7	159	S0	u
NGC1107	—	F	4	35	3350	72	3424	176	12	256	S0	—
NGC1153	—	F	4	61	3116	33	3126	226	7	—	S0	u
NGC1211	—	F	2	44	3250	37	3171	114	7	174	S0+	y
NGC1298	—	F	3	30	6514	26	6528	166	7	178	E+	—
NGC1550	—	F	2	46	3836	48	3714	295	7	—	S0	—
NGC1552	—	F	3	38	4958	96	4924	232	7	—	S0	—

Table 1—Continued

Name (1)	Alt-Name (2)	Env (3)	N (4)	S/N (5)	cZ_{meas} (6)	cZ_{err} (7)	cZ_{lit} (8)	σ_{meas} (9)	σ_{err} (10)	σ_{lit} (11)	Morph (12)	H α (13)
NGC2693	—	F	3	69	4928	68	4942	267	25	326	E3	—
NGC2778	—	F	2	51	2082	25	2016	160	7	180	E	u
NGC2880	—	F	3	74	1608	21	1551	146	7	142	S0	—
NGC2918	—	F	2	39	6823	43	6810	233	7	—	E	—
NGC2950	—	F	2	91	1334	17	1337	168	7	183	S0	—
NGC2954	—	F	2	48	3743	20	3821	195	7	218	E	—
NGC3071	—	F	3	28	6430	29	6422	150	7	—	—	u
NGC3102	—	F	4	22	3052	12	3066	134	7	166	S0	—
NGC3156	—	F	2	50	1375	37	1266	79	7	87	S0	y
NGC3193	—	F	2	76	1318	17	1399	197	7	191	E	—
NGC3248	—	F	2	54	1523	18	1466	114	7	—	S0	—
NGC3266	—	F	2	49	1765	12	1616	139	7	—	S0+	—
NGC3489	—	F	2	116	623	19	677	115	7	138	S0+	—
NGC3524	—	F	2	30	1365	7	1369	109	7	—	S0	—
NGC3599	—	F	2	40	755	19	835	81	7	79	S0	y
NGC3648	—	F	2	51	1948	20	1988	170	7	—	S0	y
NGC3731	—	F	4	28	3124	14	3212	171	7	176	E	—
NGC3757	—	F	4	37	1161	11	1273	165	7	—	S0	—
NGC3818	—	F	3	36	1664	26	1701	183	7	198	E	—
NGC3872	—	F	2	64	3161	43	3186	296	7	256	E	—
NGC4283	—	F	3	49	984	7	1076	130	7	105	E	—
NGC4296	—	F	2	41	4095	29	4227	213	7	195	S0	u
NGC4308	—	F	3	15	589	10	624	90	7	87	E	—
NGC4648	—	F	3	17	1414	18	1474	210	7	224	E	—
NGC5342	—	F	3	54	2249	17	2211	178	13	188	S0	n
NGC5370	—	F	3	30	3081	35	3057	109	7	135	S0+	y
NGC5422	—	F	5	54	1820	14	1782	176	8	—	S0	—
NGC5424	—	F	2	34	6052	35	5951	194	7	189	S0	y
NGC5459	—	F	3	35	5193	25	5261	200	10	217	S0	—
NGC5481	—	F	2	40	2132	14	2064	148	7	140	E	y
NGC5500	—	F	4	33	1988	25	1881	107	7	—	E	—
NGC5576	—	F	2	88	1511	14	1482	182	7	190	E	—
NGC5582	—	F	2	53	1362	16	1448	179	7	150	E	n
NGC5590	—	F	2	31	3221	21	3242	173	7	—	S0	u
NGC5596	—	F	3	38	3143	20	3167	124	7	152	S0	u
NGC5603	—	F	3	49	5664	20	5635	206	8	—	S0	y
NGC5611	—	F	2	56	2015	22	1957	152	7	—	S0	—
NGC5623	—	F	3	40	3642?	30	3356	273	17	—	E	y
NGC5629	—	F	2	35	4444	36	4498	258	7	261	S0	—
NGC5631	—	F	2	35	2067	17	1979	169	8	135	S0+	y
NGC5644	—	F	4	44	7502	30	7562	272	7	—	S0	—

Table 1—Continued

Name (1)	Alt-Name (2)	Env (3)	N (4)	S/N (5)	cz_{meas} (6)	cz_{err} (7)	cz_{lit} (8)	σ_{meas} (9)	σ_{err} (10)	σ_{lit} (11)	Morph (12)	H α (13)
NGC5770	—	F	2	52	1491	14	1464	104	7	124	S0	—
NGC5813	—	F	2	62	1930	23	1972	233	7	230	E	y
NGC5831	—	F	3	60	1703	22	1656	167	7	168	E	—
NGC5845	—	F	2	56	1471	33	1456	229	7	244	E	—
NGC5869	—	F	3	55	1934	14	2087	182	7	—	S0	n
NGC5966	—	F	3	43	4477	26	4474	236	7	174	E	y
NGC5982	—	F	5	66	3155	23	3017	256	7	256	E	—
NGC6003	—	F	2	35	3937	12	4060	153	7	184	S0	n
NGC6017	—	F	2	38	1682	22	1626	117	7	—	S0+	y
NGC6030	—	F	3	34	4407	19	4491	197	7	—	S0+	—
NGC6126	—	F	4	37	9859	40	9759	226	9	—	S0+	—
NGC6127	—	F	2	30	4601	23	4644	248	18	225	E	—
NGC6137	—	F	3	36	9306	38	9308	303	14	293	E	—
NGC7194	—	F	3	39	8102	101	8042	243	7	—	E	—
NGC7280	—	F	3	59	1900	17	1844	98	7	—	S0+	y
NGC7391	—	F	4	53	2982	93	3049	196	7	281	E	u
NGC7411	—	F	3	40	6796	48	6835	251	18	—	E	—
NGC7454	—	F	3	32	1992	20	2051	120	7	121	E	—
NGC7461	—	C	4	49	4234	51	4272	159	7	—	S0	—
NGC7557	—	P	2	21	3692	19	3754	81	7	—	S0+	—
NGC7611	—	P	4	79	3331	51	3252	194	7	—	S0	n
NGC7612	—	P	3	41	3186	45	3213	173	7	196	S0	—
NGC7623	—	P	3	51	3738	24	3739	171	7	—	S0+	—
NGC7628	—	F	3	45	4251	45	4202	148	7	—	E	—
NGC7671	—	F	4	50	3904	69	3875	254	8	—	S0	u
NGC7698	—	F	4	41	6939	53	7028	126	9	—	S0	n
NGC7703	—	F	4	41	4062	22	3936	146	7	—	S0	y
NGC7707	—	F	4	41	5544	34	5484	187	10	—	S0	—
NGC7711	—	F	4	63	3999	59	4057	151	7	181	S0	y
UGC06604	NGC3795B	F	6	28	1437	9	1358	126	7	—	E	—
UGC08876	—	F	4	46	2074	12	2113	159	7	—	S0	—
UGC12454	—	F	3	17	4892	48	4793	155	15	—	S0	—
UGC12472	—	F	3	45	6406	75	6511	151	7	—	S0	y
UGC9519	—	F	2	18	1702	29	1692	95	7	—	S0	y
VCC049	NGC4168	V	2	23	2215	11	2284	182	16	186	E	—
VCC140	IC3065	V	2	21	1013	26	1072	63	13	—	S0	n
VCC218	IC3100	V	4	13	454	55	533	87	17	—	dS0	y
VCC345	NGC4261	V	4	22	2220	24	2238	308	7	326	E	—
VCC389	IC0781	V	4	23	1369	25	1330	55	15	—	dS0	n
VCC523	NGC4306	V	3	31	1981	20	1508	56	7	—	S0+	n
VCC538	NGC4309A	V	4	15	620	37	500	57	12	—	E	n

Table 1—Continued

Name (1)	Alt-Name (2)	Env (3)	N (4)	S/N (5)	cz_{meas} (6)	cz_{err} (7)	cz_{lit} (8)	σ_{meas} (9)	σ_{err} (10)	σ_{lit} (11)	Morph (12)	H α (13)
VCC634	NGC4328	V	4	7	429	40	499	53	20	36	dE	—
VCC685	NGC4350	V	3	9	1200	15	1241	112	7	—	S0	—
VCC698	NGC4352	V	7	40	2070	7	2106	63	14	62	S0+	n
VCC731	NGC4365	V	2	68	1222	18	1243	271	7	261	E	—
VCC751	IC3292	V	4	17	697	36	710	68	8	—	dS0	n
VCC758	NGC4370	V	4	13	726	18	782	104	15	—	S0+	u
VCC781	IC3303	V	4	17	-337	54	-254	63	16	—	dS0	y
VCC784	NGC4379	V	2	55	939	20	1069	153	7	70	S0+	—
VCC828	NGC4387	V	3	44	472	11	561	105	7	112	E	—
VCC856	IC3328	V	3	10	961	34	972	74	16	38	dE	—
VCC929	NGC4415	V	3	18	839	20	910	65	10	41	E	—
VCC944	NGC4417	V	4	73	820	12	843	164	7	84	S0+	—
VCC966	NGC4421	V	2	42	1610	14	1603	71	7	—	S0+	n
VCC1010	NGC4431	V	4	16	878	12	913	75	12	55	S0+	y
VCC1025	NGC4434	V	3	54	987	13	1071	128	7	115	E	—
VCC1030	NGC4435	V	4	83	771	13	801	197	7	168	S0+	—
VCC1036	NGC4436	V	4	24	1004	28	1135	83	12	40	dS0	—
VCC1062	NGC4442	V	4	104	530	17	532	197	7	217	S0+	—
VCC1073	IC0794	V	4	5	1860	41	1899	67	28	41	dE	—
VCC1125	NGC4452	V	4	37	165	6	195	114	7	—	S0	—
VCC1146	NGC4458	V	3	48	593	14	635	113	7	106	E	—
VCC1178	NGC4464	V	3	58	1173	16	1243	147	7	121	E	—
VCC1183	IC3413	V	3	18	1283	31	1387	81	7	69	dS0	n
VCC1199	—	V	4	9	1201	21	900	69	19	—	E	n
VCC1231	NGC4473	V	2	83	2141	23	2244	201	7	193	E	—
VCC1242	NGC4474	V	4	54	1588	7	1610	112	7	87	S0+	—
VCC1250	NGC4476	V	2	47	2013	20	1978	69	7	69	S0+	y
VCC1279	NGC4478	V	2	74	1402	20	1349	155	7	143	E	n
VCC1283	NGC4479	V	4	24	912	23	876	93	7	—	S0+	n
VCC1297	NGC4486B	V	3	53	1485	21	1555	172	7	185	E	—
VCC1303	NGC4483	V	3	52	846	15	875	97	7	—	S0+	—
VCC1318	NGC4488	V	4	31	972	8	980	80	7	—	S0+	—
VCC1321	NGC4489	V	3	51	895	18	967	75	7	51	S0	—
VCC1422	IC3648	V	4	24	1351	29	1372	54	8	36	E+	n
VCC1440	IC0798	V	3	19	382	21	414	59	9	—	E	—
VCC1475	NGC4515	V	3	61	1011	21	1018	104	7	91	E	—
VCC1479	NGC4516	V	3	8	917	9	958	118	7	—	S0+	—
VCC1488	IC3487	V	3	17	1038	60	1157	108	38	—	E	n
VCC1521	IC3499	V	4	36	1198	20	1212	80	7	—	S0	n
VCC1535	NGC4526	V	4	104	572	25	448	282	11	267	S0+	—
VCC1537	NGC4528	V	4	65	1342	8	1374	124	7	107	S0+	—

Table 1—Continued

Name (1)	Alt-Name (2)	Env (3)	N (4)	S/N (5)	CZ_{meas} (6)	CZ_{err} (7)	CZ_{lit} (8)	σ_{meas} (9)	σ_{err} (10)	σ_{lit} (11)	Morph (12)	H α (13)
VCC1545	IC3509	V	3	12	2000	22	2050	65	10	—	E	—
VCC1614	IC3540	V	4	23	754	36	753	58	7	—	S0+	y
VCC1630	NGC4451	V	3	47	1109	11	1172	109	7	—	E	—
VCC1827	NGC4598	V	4	26	2020	23	1961	65	7	92	S0	n
VCC1871	IC3653	V	4	33	402	21	603	117	7	51	E	—
VCC1903	NGC4621	V	3	49	453	17	410	228	7	230	E	—
VCC1912	IC0810	V	4	30	-128	35	-169	64	14	—	dS0	n
VCC1938	NGC4638	V	4	88	1135	11	1164	157	7	132	S0	—
VCC1939	NGC4636	V	2	76	938	15	938	203	13	207	E	—
VCC2000	NGC4660	V	2	74	989	20	1083	187	7	185	E	—
VCC2048	IC3773	V	4	24	1144	38	1095	79	14	40	dS0	n

Note. —

column (1): Galaxy name

column (2): Alternate NGC or IC name from NED

column (3): F=“field”; V=Virgo Cluster; P=Pegasus Cluster; LG=Local Group

column (4): Number of combined spectra

column (5): Signal-to-noise ratio of combined spectrum, measured near 4000 Å

column (6-7): Measured heliocentric radial velocity

column (8): Heliocentric radial velocity from NED or from Falco et al. (1999)

column (9-10): Measured velocity dispersion & errors

columns (11): Velocity dispersions, from McElroy (1995), Simien & Prugniel (2002), Pedraz et al. (2002), and Geha et al. (2002).

column (12): Morphology from NED (NASA Extragalactic Database). Those in turn originate either from de Vaucouleurs et al. (1991), or Bingelli et al. (1985). An E+ or S0+ is our own note to indicate the presence of rings, shells, or other peculiarities based on the NED designation

column (13): H α detection. A ‘y’ indicates a detection of H α , ‘n’ indicates no detection, and ‘u’ indicates uncertain detection.

Table 2. List of Spectral Indices Measured

Spectral Index	Ref ^a	Col ^b	Unit
H δ / λ 4045	R94	(2)	
H δ / λ 4063	”	(4)	
SrII λ 4077/ λ 4045	”	(6)	
SrII λ 4077/ λ 4063	”	(8)	
H γ / λ 4325	”	(10)	
λ 4289/ λ 4271	”	(12)	
λ 4384/ λ 4352	”	(14)	
p[Fe/H]	”	(16)	
Ca II H/K	”	(18)	
λ 3888/ λ 3859	”	(20)	
p4220/p4209	”	(22)	
EW(Fe4045)	”	(24)	Å
EW(Ca4226)	”	(26)	Å
EW(H γ)	”	(28)	Å
H δ_A	WO97	(30)	Å
H γ_A	”	(32)	Å
H δ_F	”	(34)	Å
H γ_F	”	(36)	Å
Ca4227	W94	(38)	Å
G4300	”	(40)	Å
Fe4383	”	(42)	Å
H β	”	(44)	Å
Fe5015	”	(46)	Å
Mg <i>b</i>	”	(48)	Å
Fe5270	”	(50)	Å
CN1	”	(52)	mag
CN2	”	(54)	mag
Mg ₁	”	(56)	mag
Mg ₂	”	(58)	mag
Hn/Fe	CRC00	(60)	

^a References: R94 (Rose, 1994); WO97 (Worthey & Ottaviani, 1997); W94 (Worthey et al., 1994); CRC00(Concannon, Rose, & Caldwell 2000)

^bColumn number in Table 3

Table 3. Spectral Indices and Their Errors (Full Table Available as a Separate File)

Galaxy ID	$\frac{H\delta^a}{\lambda 4045}$	$\frac{H\delta}{\lambda 4063}$	$\frac{SrII\lambda 4077}{\lambda 4045}$	$\frac{SrII\lambda 4077}{\lambda 4063}$	$\frac{H\gamma^a}{\lambda 4325}$	$\frac{\lambda 4289}{\lambda 4271}$	$\frac{\lambda 4384}{\lambda 4352}$	p[Fe/H]	Ca II	$\frac{\lambda 3888^a}{\lambda 3859}$	$\frac{p4220}{p4209}$											
	EW(Fe)	EW(Ca)	EW(H γ)	H δ_A	H γ_A	H δ_F	H γ_F		Ca4227	Fe4383 ^b	H $\beta^{a,b}$											
	Fe5015	Mg b^b	Fe5270 ^b	CN1	CN2	Mg ₁ ^b	Mg ₂ ^b	Hn/Fe ^a	$\Delta H\beta_{emiss}^c$	$\Delta H\beta_{NSAR}^d$												
A00368+25	0.925	0.013	0.940	0.013	1.012	0.015	1.028	0.015	0.995	0.010	1.020	0.010	0.876	0.008	1.100	0.013	1.166	0.058	1.109	0.033	1.002	0.010
	0.328	0.040	0.567	0.031	0.458	0.027	-1.441	0.392	-5.524	0.318	0.852	0.220	-1.463	0.167	1.245	0.144	5.595	0.234	4.575	0.308	1.632	0.114
	4.160	0.250	3.614	0.129	2.729	0.135	0.058	0.009	0.104	0.011	-0.266	0.004	0.083	0.006	1.009	0.013	0.018					
A10025+59	0.977	0.009	0.988	0.010	1.009	0.011	1.019	0.011	1.004	0.007	1.023	0.007	0.878	0.006	1.137	0.009	1.215	0.041	1.212	0.024	1.016	0.007
	0.393	0.048	0.592	0.038	0.479	0.033	-2.156	0.202	-6.376	0.164	0.663	0.114	-1.782	0.086	1.251	0.074	5.854	0.120	4.919	0.159	1.634	0.059
	5.014	0.129	3.911	0.067	2.998	0.070	0.093	0.004	0.138	0.004	-0.240	0.002	0.110	0.002	1.065	0.009	0.033					
A15572+48	0.893	0.014	0.919	0.015	1.007	0.017	1.036	0.016	0.962	0.011	0.983	0.011	0.876	0.009	1.093	0.014	1.136	0.063	1.047	0.036	0.988	0.011
	0.227	0.056	0.470	0.044	0.512	0.039	-0.434	0.394	-4.848	0.319	1.010	0.221	-0.924	0.167	1.201	0.144	5.210	0.235	4.181	0.309	1.859	0.115
	4.451	0.251	3.108	0.130	2.573	0.136	0.014	0.005	0.054	0.007	-0.082	0.002	0.132	0.003	0.967	0.014	0.046					
A16044+16	0.914	0.019	0.923	0.020	1.009	0.023	1.019	0.022	0.965	0.015	1.006	0.015	0.889	0.012	1.111	0.019	1.115	0.085	1.100	0.049	1.008	0.014
	0.262	0.036	0.499	0.029	0.514	0.025	-1.095	0.207	-4.869	0.168	1.113	0.116	-0.809	0.088	1.312	0.076	5.327	0.123	4.645	0.163	2.164	0.060
	4.862	0.132	2.331	0.068	2.274	0.071	0.051	0.002	0.091	0.002	-0.987	0.001	-0.262	0.001	0.993	0.019	0.000					
A23174+26	0.969	0.024	0.970	0.025	1.030	0.028	1.031	0.028	1.008	0.019	0.983	0.019	0.838	0.015	1.094	0.024	1.278	0.107	1.242	0.061	1.047	0.018
	0.608	0.066	0.440	0.052	0.381	0.046	-2.593	0.408	-6.610	0.331	0.096	0.229	-1.801	0.173	1.221	0.150	5.890	0.243	5.433	0.321	1.394	0.119
	4.829	0.260	3.947	0.135	2.966	0.141	0.104	0.012	0.151	0.014	-0.378	0.005	0.071	0.007	1.073	0.023	0.264					
A2330+29	0.994	0.028	0.988	0.030	1.043	0.034	1.037	0.033	1.028	0.023	1.045	0.022	0.866	0.019	1.123	0.029	1.152	0.127	1.171	0.072	1.012	0.022
	0.413	0.108	0.428	0.085	0.322	0.075	-2.348	0.525	-6.263	0.426	0.360	0.295	-1.747	0.223	1.438	0.192	5.524	0.313	5.432	0.412	1.591	0.153
	4.847	0.335	4.231	0.173	3.247	0.181	0.108	0.023	0.156	0.028	-0.248	0.010	0.158	0.014	1.064	0.028	0.282					

^aCorrected for emission

^bCorrected for non-solar abundance ratios (NSAR)

^cCorrection to the Lick H β index due to emission

^dCorrection to the Lick H β index due to NSAR

Table 4. Measured Intrinsic Scatter

Group	Num	H β ^a	Hn/Fe	Mg b ^a	Fe 5270 ^a
Scatter for Uncorrected Indices					
log $\sigma > 2.0$	100	0.201 \pm 0.021	0.023 \pm 0.004	0.447 \pm 0.027	0.263 \pm 0.019
(median index error)	...	(\pm 0.078)	(\pm 0.014)	(\pm 0.088)	(\pm 0.090)
log $\sigma < 2.0$	38	0.383 \pm 0.093	0.078 \pm 0.023	0.567 \pm 0.104	0.179 \pm 0.025
(median index error)	...	(\pm 0.155)	(\pm 0.031)	(\pm 0.175)	(\pm 0.184)
Scatter for Emission-Corrected Indices					
log $\sigma > 2.0$	100	0.214 \pm 0.027	0.021 \pm 0.005	0.449 \pm 0.029	0.264 \pm 0.020
log $\sigma < 2.0$	38	0.600 \pm 0.107	0.084 \pm 0.021	0.572 \pm 0.100	0.193 \pm 0.028
Scatter for Emission and NSAR-Corrected Indices					
log $\sigma > 2.0$	100	0.208 \pm 0.025	0.021 \pm 0.005	0.297 \pm 0.023	0.144 \pm 0.017
log $\sigma < 2.0$	38	0.581 \pm 0.107	0.084 \pm 0.021	0.546 \pm 0.092	0.282 \pm 0.045

^aThe Lick indices have *not* been converted to magnitudes

Table 5. Summary of Mean Ages by log σ

log σ Range	Number	Mean Age	RMS
log $\sigma < 1.8$	12	3.6	1.9
1.8 \leq log $\sigma < 2.0$	30	3.6	2.1
2.0 \leq log $\sigma < 2.2$	48	7.4	4.2
log $\sigma \geq 2.2$	61	9.9	4.2

Table 6. Kolmogorov-Smirnoff Test for Ages of Different $\log \sigma$ Groups

Group Combination	Likelihood	Group Combination	Likelihood
1-2	8.82×10^{-1}	2-3	9.42×10^{-6}
1-3	2.92×10^{-4}	2-4	4.59×10^{-9}
1-4	2.32×10^{-5}	3-4	5.62×10^{-4}

Note. — Groups by velocity dispersion are: Group1 — $\log \sigma < 1.8$,
Group 2 — $1.8 \leq \log \sigma < 2.0$, Group 3 — $2.0 \leq \log \sigma < 2.2$, Group 4 — $\log \sigma > 2.2$

Table 7. Effects of Index Corrections on Age and $[\text{Fe}/\text{H}]$ Determinations

Corrections	$\langle \text{Age} \rangle$	$\langle [\text{Fe}/\text{H}] \rangle$	$\langle \text{Age} \rangle$	$\langle [\text{Fe}/\text{H}] \rangle$
	Fe4383 vs H γ /Fe		Fe5270 vs H β	
None	8.9 ± 5.3	0.01 ± 0.37	11.1 ± 6.3	-0.15 ± 0.17
Emission	8.2 ± 5.0	0.01 ± 0.33	9.3 ± 6.2	-0.12 ± 0.16
Emission + NSAR	9.3 ± 6.0	-0.03 ± 0.17

Table 8. Age and Metallicity Determinations^a

Galaxy	Ages				Metallicities			
(1)	(2)	(3)	(4)	(5)	(6)	(7)	(8)	(9)
A00368+25	11.2±6.8	8.2	15.5	15.1	-0.25±0.22	-0.10	-0.31	-0.21
A10025+59	19.2±0.2	10.5	12.2	12.2	1.00±0.19	0.00	-0.18	-0.02
A15572+48	7.3±5.4	6.4	8.4	8.2	-0.25±0.24	-0.17	-0.28	-0.20
A16044+16	7.5±4.1	14.9	2.7	4.0	-0.14±0.17	-0.44	0.19	-0.30
A23174+26	13.3±0.0	11.7	-0.10±0.00	-0.05
A2330+29	11.6±9.4	7.1	12.2	12.0	-0.08±0.29	0.17	-0.07	0.08
IC0195	7.9±3.4	8.4	6.8	7.6	-0.12±0.17	-0.15	-0.07	-0.14
IC0555	7.4±4.6	7.0	7.1	7.9	0.03±0.24	0.06	0.04	0.04
IC1153	8.5±5.3	9.3	5.8	8.3	0.05±0.18	0.00	0.14	0.03
IC1211	11.7±1.8	4.7	6.7	4.5	-0.16±0.17	0.25	0.01	0.26
IC598a	3.0±0.0	2.8	2.1	2.3	-0.26±0.00	-0.13	-0.04	-0.08
M32	2.6±0.2	3.2	2.9	2.9	0.27±0.05	0.10	0.23	0.10
NGC183	17.1±0.9	9.4	9.6	9.5	-0.33±0.02	-0.04	-0.19	-0.04
NGC205	0.9±0.0	1.2	1.3	1.3	-0.37±0.02	-0.67	-0.49	-0.73
NGC448	8.8±5.9	14.3	7.3	8.8	-0.11±0.23	-0.33	-0.06	-0.28
NGC474	7.9±3.3	6.4	7.4	7.9	-0.06±0.17	0.06	-0.04	0.03
NGC502	7.7±1.0	6.6	9.0	8.8	0.03±0.03	0.09	0.00	0.07
NGC516	2.0±0.6	3.6	2.7	3.1	0.27±0.21	-0.26	0.16	-0.27
NGC525	6.3±3.5	6.2	6.3	6.6	-0.12±0.20	-0.10	-0.11	-0.11
NGC584	7.4±2.5	6.6	8.4	8.9	0.03±0.10	0.07	0.00	0.04
NGC636	8.8±3.9	6.0	10.5	10.1	-0.08±0.18	0.11	-0.13	0.04
NGC656	4.8±3.3	6.7	8.1	8.1	0.10±0.26	-0.03	0.00	-0.05
NGC770	8.0±4.3	7.5	6.8	7.1	-0.15±0.19	-0.12	-0.11	-0.11
NGC774	16.3±1.0	7.8	11.3	10.2	-0.35±0.19	0.00	-0.28	-0.04
NGC821	11.6±2.4	9.3	9.8	10.2	-0.05±0.08	0.09	0.02	0.07
NGC938	9.9±7.0	6.5	7.1	7.3	-0.24±0.22	0.00	-0.16	-0.01
NGC990	11.3±4.2	8.5	8.3	8.0	-0.20±0.13	-0.04	-0.11	-0.03
NGC1026	10.9±6.0	8.5	-0.15±0.19	0.00
NGC1029	8.2±3.5	7.6	0.06±0.13	0.08
NGC1107	9.9±5.8	8.2	...	17.3	-0.04±0.21	0.07	...	-0.07
NGC1153	9.4±4.5	9.9	0.06±0.17	0.03
NGC1211	4.0±1.7	4.9	4.0	4.2	0.11±0.18	0.01	0.11	0.02
NGC1298	6.4±7.6	5.7	4.9	5.5	-0.07±0.40	0.00	-0.01	0.00
NGC1552	13.8±0.0	12.5	-0.18±0.00	-0.13
NGC2778	10.6±3.4	6.5	9.8	10.0	-0.12±0.13	0.12	-0.09	0.07
NGC2880	7.6±1.9	6.3	4.7	5.6	-0.11±0.10	0.02	0.02	0.04
NGC2918	...	6.9	8.9	11.3	...	0.04	0.19	-0.04
NGC2950	7.3±1.0	4.5	3.2	3.2	0.02±0.05	0.21	0.25	0.27
NGC2954	3.9±1.6	2.8	2.6	2.9	0.10±0.16	0.30	0.25	0.30
NGC3071	10.7±6.4	9.3	12.4	14.3	-0.15±0.22	-0.07	-0.17	-0.14

Table 8—Continued

Galaxy		Ages			Metallicities			
(1)	(2)	(3)	(4)	(5)	(6)	(7)	(8)	(9)
NGC3156	0.8±0.0	1.2	0.7	1.2	0.05±0.21	-0.26	0.10	-0.24
NGC3193	9.1±1.7	7.1	11.7	11.9	-0.01±0.08	0.10	-0.10	0.02
NGC3248	3.2±0.9	3.2	2.3	2.6	0.15±0.09	0.16	0.30	0.17
NGC3266	11.1±3.3	9.4	15.4	14.6	-0.25±0.08	-0.17	-0.31	-0.24
NGC3489	1.8±0.1	1.9	1.5	1.7	0.19±0.06	0.15	0.32	0.18
NGC3524	4.9±1.3	4.0	3.2	3.1	-0.09±0.11	0.05	0.05	0.07
NGC3599	1.9±0.4	1.8	1.1	1.3	0.17±0.14	0.23	0.55	0.32
NGC3648	13.8±3.1	6.4	...	17.6	-0.14±0.09	0.22	...	0.09
NGC3731	13.9±2.0	12.7	16.7	...	-0.14±0.11	-0.09	-0.18	...
NGC3757	13.5±1.7	8.2	11.4	10.4	-0.25±0.06	0.00	-0.22	-0.05
NGC3818	8.9±5.8	5.8	10.7	11.0	-0.01±0.23	0.16	-0.08	0.07
NGC4283	7.2±3.3	5.9	6.7	6.7	0.09±0.14	0.18	0.11	0.16
NGC4296	7.8±3.3	5.7	5.8	6.3	0.08±0.13	0.21	0.16	0.19
NGC4308	5.7±9.7	6.4	6.8	6.8	0.00±0.59	-0.08	-0.06	-0.09
NGC4648	4.1±0.6	2.8	...	13.2	0.16±0.23	0.39	...	0.16
NGC5342	16.6±0.0	6.7	...	15.6	-0.36±0.20	0.07	...	-0.05
NGC5370	6.5±3.0	4.1	6.6	5.2	0.00±0.18	0.19	0.00	0.16
NGC5422	8.4±5.4	6.4	10.3	10.4	0.05±0.24	0.15	-0.01	0.08
NGC5424	13.3±5.1	9.5	-0.22±0.12	-0.05
NGC5459	12.2±9.4	8.3	11.0	14.2	-0.25±0.26	-0.07	-0.23	-0.17
NGC5481	8.5±2.8	8.4	-0.10±0.12	-0.09
NGC5500	5.6±4.3	6.2	10.0	10.7	-0.20±0.30	-0.26	-0.34	-0.33
NGC5576	5.9±1.4	6.7	6.1	6.8	0.05±0.07	-0.01	0.04	-0.01
NGC5582	10.5±4.6	4.8	8.8	8.5	-0.29±0.13	0.09	-0.24	0.05
NGC5590	10.3±5.5	5.7	10.9	9.8	-0.20±0.18	0.10	-0.21	0.03
NGC5596	2.6±0.2	7.0	10.5	15.3	0.41±0.12	-0.17	0.00	-0.26
NGC5603	3.0±0.5	4.1	5.7	6.7	0.41±0.12	0.20	0.17	0.14
NGC5611	6.4±1.1	7.1	8.9	8.7	-0.11±0.08	-0.18	-0.20	-0.20
NGC5631	3.1±0.9	2.7	2.8	3.0	0.19±0.11	0.30	0.24	0.30
NGC5770	5.6±1.4	4.8	3.2	3.6	-0.13±0.10	-0.06	0.03	-0.03
NGC5831	3.0±0.6	4.4	6.3	7.1	0.35±0.11	0.13	0.12	0.08
NGC5845	9.8±0.0	7.9	10.0	10.8	-0.01±0.00	0.08	-0.02	0.04
NGC5865	7.4±3.7	6.8	10.6	10.6	0.08±0.15	0.12	0.00	0.06
NGC5966	4.7±0.0	6.1	2.1	2.9	0.11±0.00	0.02	0.41	0.08
NGC6003	4.9±3.4	7.8	6.5	7.9	0.11±0.23	-0.11	0.06	-0.09
NGC6017	5.9±3.3	3.1	2.7	2.8	-0.17±0.24	0.17	0.09	0.19
NGC6030	6.5±6.3	10.8	11.3	15.9	0.09±0.35	-0.17	-0.06	-0.22
NGC6126	9.1±6.9	3.8	10.9	7.9	0.00±0.28	0.40	-0.06	0.27
NGC7280	3.7±1.1	3.7	2.5	2.7	0.05±0.12	0.04	0.20	0.08
NGC7391	12.4±5.8	7.5	...	15.9	-0.12±0.17	0.11	...	0.01
NGC7454	4.9±2.3	6.7	4.2	5.6	-0.03±0.17	-0.21	0.03	-0.18

Table 8—Continued

Galaxy	Ages			Metallicities				
(1)	(2)	(3)	(4)	(5)	(6)	(7)	(8)	(9)
NGC7461	8.7±4.9	7.2	-0.07±0.23	0.03
NGC7557	1.7±0.1	2.6	2.6	2.9	0.31±0.23	-0.15	0.11	-0.19
NGC7611	2.8±0.5	3.8	3.7	4.1	0.27±0.13	0.08	0.16	0.07
NGC7612	2.8±0.9	4.9	11.3	12.9	0.40±0.13	0.06	-0.02	-0.05
NGC7623	5.9±2.1	6.4	11.0	11.5	0.09±0.10	0.06	-0.08	-0.04
NGC7628	6.6±3.1	6.7	3.3	3.5	-0.01±0.17	-0.03	0.17	0.03
NGC7698	10.0±6.9	6.6	4.8	5.7	-0.14±0.24	0.07	0.04	0.09
NGC7703	3.5±2.2	4.5	7.0	6.9	0.10±0.27	-0.06	-0.11	-0.10
NGC7707	19.1±0.0	7.8	8.8	8.9	1.00±0.24	0.04	-0.20	0.04
NGC7711	6.2±2.4	4.1	5.3	5.0	-0.02±0.14	0.16	0.02	0.15
UGC06604	6.9±5.9	6.8	7.3	7.5	-0.10±0.31	-0.10	-0.13	-0.12
UGC0887	18.2±0.7	10.2	...	16.8	-0.33±0.31	-0.08	...	-0.16
UGC12454	...	12.7	4.4	5.2	...	-0.21	-0.12	-0.08
UGC12472	0.7±0.0	1.1	0.5	1.0	0.42±0.14	-0.22	0.10	-0.20
UGC9519	1.8±1.1	1.8	0.9	1.4	0.07±0.47	-0.03	0.35	0.07
VCC049	4.8±5.3	3.5	2.1	2.4	0.10±0.34	0.27	0.43	0.29
VCC140	3.4±2.0	3.5	2.7	2.8	-0.26±0.22	-0.27	-0.16	-0.24
VCC218	1.2±0.4	2.1	1.4	2.0	0.15±0.12	-0.70	0.08	-0.69
VCC389	3.7±2.9	3.1	2.0	2.2	-0.24±0.33	-0.12	0.03	-0.02
VCC523	1.9±0.4	1.8	1.8	1.9	0.02±0.25	0.05	0.04	0.04
VCC538	5.6±0.7	3.2	1.9	1.9	-0.62±0.25	-0.29	-0.22	-0.18
VCC634	2.7±0.0	4.8	0.9	1.7	-0.20±0.13	-0.66	0.40	-0.42
VCC685	10.4±2.2	5.9	...	17.4	0.00±0.10	0.24	...	0.08
VCC698	4.3±4.2	3.5	3.0	3.1	0.00±0.36	0.10	0.09	0.10
VCC751	2.4±1.3	3.2	3.0	3.0	0.16±0.35	-0.10	0.07	-0.11
VCC758	7.9±0.0	3.7	2.4	2.6	-0.18±0.12	0.21	0.21	0.25
VCC781	1.6±0.1	1.0	2.0	1.3	-0.80±0.25	-0.01	-1.00	0.01
VCC784	...	15.3	10.5	13.8	...	-0.30	-0.28	-0.29
VCC828	15.4±1.7	8.0	11.7	11.9	-0.35±0.04	-0.04	-0.30	-0.13
VCC856	3.3±0.4	5.2	-0.43±0.12	-0.85
VCC929	6.0±13.7	9.6	-0.25±0.65	-0.52
VCC944	9.7±3.9	8.4	13.4	13.2	-0.08±0.14	0.02	-0.16	-0.07
VCC966	2.8±0.5	3.0	2.1	2.4	0.30±0.12	0.24	0.43	0.26
VCC1010	8.0±0.2	5.3	5.4	5.3	-0.40±0.34	-0.14	-0.28	-0.14
VCC1025	6.8±3.6	6.5	9.4	9.6	-0.07±0.19	-0.03	-0.15	-0.09
VCC1030	4.3±1.5	4.1	8.2	7.9	0.09±0.15	0.12	-0.07	0.05
VCC1036	4.6±6.3	3.7	7.2	6.6	-0.34±0.39	-0.21	-0.46	-0.26
VCC1062	12.3±2.7	7.4	-0.05±0.07	0.18
VCC1073	4.2±0.0	2.8	3.0	3.0	-0.06±0.07	0.19	0.05	0.18
VCC1125	5.0±7.0	6.2	10.2	10.0	0.02±0.45	-0.09	-0.16	-0.16
VCC1146	13.0±6.5	8.8	17.2	15.1	-0.34±0.16	-0.18	-0.39	-0.25

Table 8—Continued

Galaxy	Ages				Metallicities			
(1)	(2)	(3)	(4)	(5)	(6)	(7)	(8)	(9)
VCC1178	17.2±0.9	13.8	-0.33±0.16	-0.22
VCC1183	4.8±12.2	3.1	2.2	2.2	-0.44±0.59	-0.17	-0.17	-0.08
VCC1199	5.1	6.8	0.25	0.13
VCC1231	9.4±1.3	5.7	12.1	11.3	0.00±0.06	0.21	-0.07	0.10
VCC1242	6.5±4.2	7.1	3.9	4.7	-0.04±0.26	-0.09	0.10	-0.05
VCC1250	2.2±0.4	2.1	1.9	1.9	-0.06±0.17	-0.03	0.03	-0.01
VCC1279	5.9±1.1	5.0	5.2	6.2	0.02±0.06	0.06	0.05	0.05
VCC1283	5.8±8.9	7.5	0.01±0.54	-0.17
VCC1297	15.1±6.2	10.5	-0.20±0.52	-0.01
VCC1303	7.5±3.4	4.3	9.7	8.3	-0.09±0.18	0.17	-0.16	0.11
VCC1318	1.9±0.7	1.7	1.6	1.6	0.01±0.37	0.14	0.09	0.15
VCC1321	5.0±2.1	3.4	2.9	3.0	-0.14±0.18	0.10	0.04	0.10
VCC1422	4.2±4.5	3.3	2.9	3.1	-0.41±0.44	-0.26	-0.31	-0.27
VCC1440	3.9±5.2	4.8	-0.45±0.41	-0.59
VCC1475	8.2±3.7	7.3	6.5	7.0	-0.27±0.12	-0.21	-0.21	-0.21
VCC1479	4.0±4.7	4.3	1.2	1.6	-0.03±0.54	-0.09	0.60	0.09
VCC1488	1.2±0.0	0.9	1.5	1.3	-0.47±0.54	-0.20	-0.62	-0.24
VCC1521	4.9±3.6	5.1	8.5	8.1	-0.10±0.27	-0.11	-0.24	-0.17
VCC1537	6.3±1.5	6.8	7.0	6.7	-0.05±0.12	-0.10	-0.08	-0.09
VCC1545	2.4±10.7	3.5	10.6	12.7	0.12±0.12	-0.25	-0.33	-0.37
VCC1614	1.9±0.8	1.8	1.8	1.8	-0.46±0.43	-0.34	-0.40	-0.34
VCC1630	3.1±1.4	6.4	11.4	14.5	0.29±0.20	-0.05	-0.07	-0.18
VCC1827	2.4±1.1	2.3	1.9	2.0	0.05±0.33	0.08	0.13	0.08
VCC1871	5.7±7.7	7.4	3.5	4.0	0.06±0.39	-0.09	0.20	-0.02
VCC1903	17.3±1.1	6.0	16.3	12.4	-0.23±0.39	0.26	-0.21	0.16
VCC1912	1.1±0.0	1.5	1.7	1.7	0.00±0.02	-0.34	-0.25	-0.40
VCC1938	6.3±2.4	6.5	3.8	4.1	0.15±0.12	0.13	0.29	0.19
VCC1939	10.3±4.7	6.4	-0.04±0.19	0.18
VCC2000	15.3±2.5	11.2	-0.14±0.06	0.01
VCC2048	3.0±3.2	4.7	3.0	3.7	-0.25±0.46	-0.56	-0.26	-0.53

^a column (2): age and error in Gyr determined from Fe4383 *vs* Hn/Fe diagram
column (3): age determined from Fe5270 *vs* Hn/Fe
column (4): age determined from Fe4383 *vs* H β
column (5): age determined from Fe5270 *vs* H β
column (6): [Fe/H] and error determined from Fe4383 *vs* Hn/Fe
column (7): [M/H] determined from Fe5270 *vs* Hn/Fe
column (8): [Fe/H] determined from Fe4383 *vs* H β
column (9): [M/H] determined from Fe5270 *vs* H β

Table 9. Mean Age and [Fe/H] for Different σ Groups

log σ Group	Index Pair	<Age>	<[Fe/H]>	Index Pair	<Age>	<[Fe/H]>
log $\sigma < 1.8$	<i>Fe</i> 4383 vs <i>H</i> β	2.4	-0.02	<i>Fe</i> 5270 vs <i>H</i> β	2.3	-0.22
1.8 \leq log $\sigma < 2.0$...	2.3	0.14	...	2.2	-0.12
2.0 \leq log $\sigma < 2.2$...	6.1	0.06	...	5.0	-0.13
2.2 \leq log σ	...	13.5	-0.03	...	12.8	-0.14
log $\sigma < 1.8$	<i>Fe</i> 4383 vs <i>Hn/Fe</i>	3.0	-0.28	<i>Fe</i> 5270 vs <i>Hn/Fe</i>	3.0	-0.28
1.8 \leq log $\sigma < 2.0$...	2.8	-0.06	...	3.0	-0.20
2.0 \leq log $\sigma < 2.2$...	5.8	-0.07	...	6.9	-0.17
2.2 \leq log σ	...	8.8	-0.06	...	9.4	-0.08
log $\sigma < 1.8$	<i>Fe</i> 4383 vs <i>H</i> γ_F	2.6	-0.21	<i>Fe</i> 5270 vs <i>H</i> γ_F	2.7	-0.26
1.8 \leq log $\sigma < 2.0$...	2.0	0.08	...	2.5	-0.15
2.0 \leq log $\sigma < 2.2$...	5.2	-0.04	...	6.2	-0.15
2.2 \leq log σ	...	10.6	-0.11	...	10.6	-0.11
log $\sigma < 1.8$	<i>Fe</i> 4383 vs <i>H</i> γ /4325	3.1	-0.30	<i>Fe</i> 5270 vs <i>H</i> γ /4325	3.1	-0.29
1.8 \leq log $\sigma < 2.0$...	2.6	-0.02	...	2.9	-0.19
2.0 \leq log $\sigma < 2.2$...	6.6	-0.11	...	7.2	-0.18
2.2 \leq log σ	...	9.3	-0.41	...	10.5	-0.11
log $\sigma < 1.8$	<i>Fe</i> 4383 vs <i>H</i> δ_F	2.0	-0.06	<i>Fe</i> 5270 vs <i>H</i> δ_F	2.3	-0.22
1.8 \leq log $\sigma < 2.0$...	1.7	0.17	...	2.0	-0.11
2.0 \leq log $\sigma < 2.2$...	2.5	0.20	...	3.1	-0.11
2.2 \leq log σ	...	5.4	0.07	...	6.6	-0.03
log $\sigma < 1.8$	<i>Fe</i> 4383 vs <i>H</i> δ /4045	2.6	-0.19	<i>Fe</i> 5270 vs <i>H</i> δ /4045	2.7	-0.25
1.8 \leq log $\sigma < 2.0$...	2.0	0.08	...	2.4	-0.14
2.0 \leq log $\sigma < 2.2$...	3.1	0.09	...	4.1	-0.12
2.2 \leq log σ	...	4.1	0.14	...	5.2	0.00
log $\sigma < 1.8$	<i>Fe</i> 4383 vs <i>H</i> 8/3859	3.4	-0.32	<i>Fe</i> 5270 vs <i>H</i> 8/3859	3.2	-0.28
1.8 \leq log $\sigma < 2.0$...	5.7	0.37	...	4.0	-0.22
2.0 \leq log $\sigma < 2.2$...	8.8	0.39	...	9.2	-0.21

Table 9—Continued

log σ Group	Index Pair	$\langle \text{Age} \rangle$	$\langle [\text{Fe}/\text{H}] \rangle$	Index Pair	$\langle \text{Age} \rangle$	$\langle [\text{Fe}/\text{H}] \rangle$
$2.2 \leq \log \sigma$...	13.8	-0.17	...	12.6	-0.13

Table 10. A Comparison with Previous Ages and Metallicities

Galaxy	VCC Name	Age _{Lit} (Gyr)	[Z/H] _{Lit}	Age _{Meas}	[Fe/H] _{Meas}
Trager et al. (2000a)					
NGC 221	M32	3.0	0.0	2.6	0.28
NGC 636		4.1	0.34	8.8	-0.08
NGC 821		7.7	0.22	11.5	-0.05
NGC 2778		5.4	0.29	10.5	-0.19
NGC 3818		5.6	0.36	8.8	-0.01
NGC 4478	VCC1279	4.6	0.29	5.86	0.02
NGC 4489	VCC1321	2.5	0.14	4.9	-0.14
NGC 5831		2.6	0.54	3.0	0.35
NGC 7454		5.0	-0.06	4.9	-0.03
Kuntschner et al. (2001)					
NGC 2778		12.0	0.12	10.5	-0.19
NGC 3489		1.1	0.22	1.8	0.19
NGC 4434	VCC1025	12.3	-0.24	6.8	-0.06
NGC 4458	VCC1146	4.6	0.03	13.0	-0.33
NGC 4473	VCC1231	12.8	0.16	9.3	0.00
NGC 4621	VCC1903	10.9	0.34	17.2	-0.22
NGC 4660	VCC2000	21.2	-0.07	15.3	-0.14
NGC 5582		13.3	-0.15	10.4	-0.28
NGC 5831		17.5	-0.07	3.0	0.35
Vazdekis et al. (2001b)					
NGC 4464	VCC1178	19	-0.27	17.2	-0.32
NGC 4387	VCC 828	16	-0.15	15.4	-0.35
NGC 4473	VCC1231	12	0.14	9.3	0.00
NGC 4478	VCC1279	9.3	0.08	5.8	0.02

Note. — The Trager et al. (2000a) ages are taken from 2000,AJ,119,1645, Table 6A using the values for Model 4. The metallicities are their [Z/H]. The Kuntschner et al.(2001) values are from private communication of ages & metallicities derived from the data in that paper. The Vazdekis et al. determinations were interpolated from a plot in 2001,ApJ,55 1,L127

Table 11. Spectral Index Emission Correction Relations

Index	Slope	Zero-Point
$H\delta/4045$	-2.97E+12	0.266E-3
$H\gamma/4325$	-5.03E+12	0.333E-6
$H_8/3859$	-1.35E+12	-0.233E-3
Hn/Fe	-3.11E+12	-0.144E-3
$H\beta$	8.59E+13	0.666E-6

Note. — The parameters of the line index corrections as a function of the $H\beta$ emission flux removed.

Table 3. Spectral Indices and Their Errors

Galaxy ID	$\frac{H\delta^a}{\lambda 4045}$	$\frac{H\delta}{\lambda 4063}$	$\frac{SrII\lambda 4077}{\lambda 4045}$	$\frac{SrII\lambda 4077}{\lambda 4063}$	$\frac{H\gamma^a}{\lambda 4325}$	$\frac{\lambda 4289}{\lambda 4271}$	$\frac{\lambda 4384}{\lambda 4352}$	p[Fe/H]	Ca II	$\frac{\lambda 3888^a}{\lambda 3859}$	$\frac{p4220}{p4209}$											
	EW(Fe)	EW(Ca)	EW(H γ)	H δ_A	H γ_A	H δ_F	H γ_F	Ca4227	G4300	Fe4383 ^b	H $\beta^{a,b}$											
	Fe5015	Mg b^b	Fe5270 ^b	CN1	CN2	Mg ₁ ^b	Mg ₂ ^b	Hn/Fe ^a	$\Delta H\beta_{emiss}^c$	$\Delta H\beta_{NSAR}^d$												
A00368+25	0.925	0.013	0.940	0.013	1.012	0.015	1.028	0.015	0.995	0.010	1.020	0.010	0.876	0.008	1.100	0.013	1.166	0.058	1.109	0.033	1.002	0.010
	0.328	0.040	0.567	0.031	0.458	0.027	-1.441	0.392	-5.524	0.318	0.852	0.220	-1.463	0.167	1.245	0.144	5.595	0.234	4.575	0.308	1.632	0.114
	4.160	0.250	3.614	0.129	2.729	0.135	0.058	0.009	0.104	0.011	-0.266	0.004	0.083	0.006	1.009	0.013	0.018			-0.053		
A10025+59	0.977	0.009	0.988	0.010	1.009	0.011	1.019	0.011	1.004	0.007	1.023	0.007	0.878	0.006	1.137	0.009	1.215	0.041	1.212	0.024	1.016	0.007
	0.393	0.048	0.592	0.038	0.479	0.033	-2.156	0.202	-6.376	0.164	0.663	0.114	-1.782	0.086	1.251	0.074	5.854	0.120	4.919	0.159	1.634	0.059
	5.014	0.129	3.911	0.067	2.998	0.070	0.093	0.004	0.138	0.004	-0.240	0.002	0.110	0.002	1.065	0.009	0.033			-0.051		
A15572+48	0.893	0.014	0.919	0.015	1.007	0.017	1.036	0.016	0.962	0.011	0.983	0.011	0.876	0.009	1.093	0.014	1.136	0.063	1.047	0.036	0.988	0.011
	0.227	0.056	0.470	0.044	0.512	0.039	-0.434	0.394	-4.848	0.319	1.010	0.221	-0.924	0.167	1.201	0.144	5.210	0.235	4.181	0.309	1.859	0.115
	4.451	0.251	3.108	0.130	2.573	0.136	0.014	0.005	0.054	0.007	-0.082	0.002	0.132	0.003	0.967	0.014	0.046			-0.021		
A16044+16	0.914	0.019	0.923	0.020	1.009	0.023	1.019	0.022	0.965	0.015	1.006	0.015	0.889	0.012	1.111	0.019	1.115	0.085	1.100	0.049	1.008	0.014
	0.262	0.036	0.499	0.029	0.514	0.025	-1.095	0.207	-4.869	0.168	1.113	0.116	-0.809	0.088	1.312	0.076	5.327	0.123	4.645	0.163	2.164	0.060
	4.862	0.132	2.331	0.068	2.274	0.071	0.051	0.002	0.091	0.002	-0.987	0.001	-0.262	0.001	0.993	0.019	0.000			-0.147		
A23174+26	0.969	0.024	0.970	0.025	1.030	0.028	1.031	0.028	1.008	0.019	0.983	0.019	0.838	0.015	1.094	0.024	1.278	0.107	1.242	0.061	1.047	0.018
	0.608	0.066	0.440	0.052	0.381	0.046	-2.593	0.408	-6.610	0.331	0.096	0.229	-1.801	0.173	1.221	0.150	5.890	0.243	5.433	0.321	1.394	0.119
	4.829	0.260	3.947	0.135	2.966	0.141	0.104	0.012	0.151	0.014	-0.378	0.005	0.071	0.007	1.073	0.023	0.264			-0.073		
A2330+29	0.994	0.028	0.988	0.030	1.043	0.034	1.037	0.033	1.028	0.023	1.045	0.022	0.866	0.019	1.123	0.029	1.152	0.127	1.171	0.072	1.012	0.022
	0.413	0.108	0.428	0.085	0.322	0.075	-2.348	0.525	-6.263	0.426	0.360	0.295	-1.747	0.223	1.438	0.192	5.524	0.313	5.432	0.412	1.591	0.153
	4.847	0.335	4.231	0.173	3.247	0.181	0.108	0.023	0.156	0.028	-0.248	0.010	0.158	0.014	1.064	0.028	0.282			-0.055		
IC0195	0.966	0.014	0.991	0.014	1.033	0.016	1.060	0.016	0.979	0.011	1.009	0.011	0.876	0.009	1.105	0.014	1.215	0.061	1.066	0.035	1.015	0.010
	0.255	0.034	0.460	0.027	0.403	0.023	-1.896	0.271	-5.514	0.220	0.440	0.152	-1.383	0.115	1.230	0.099	5.637	0.162	4.788	0.213	1.890	0.079
	4.682	0.173	3.202	0.089	2.664	0.093	0.048	0.007	0.089	0.008	-0.266	0.003	0.036	0.004	1.004	0.013	0.000			-0.045		
IC0555	0.917	0.016	0.967	0.017	1.013	0.019	1.065	0.019	0.973	0.013	1.018	0.013	0.857	0.011	1.089	0.016	1.129	0.073	1.190	0.041	1.038	0.012
	0.402	0.045	0.509	0.036	0.517	0.031	-1.941	0.445	-6.163	0.361	0.502	0.250	-1.400	0.189	1.319	0.163	5.696	0.265	5.319	0.350	1.837	0.130
	5.124	0.284	3.796	0.147	3.001	0.154	0.080	0.007	0.113	0.009	-0.246	0.003	0.087	0.004	1.027	0.016	0.084			-0.050		
IC0598	0.881	0.041	0.884	0.042	1.028	0.048	1.020	0.047	0.899	0.032	1.020	0.032	0.939	0.026	1.093	0.041	0.996	0.182	0.856	0.104	1.001	0.031
	0.329	0.127	0.375	0.100	0.580	0.088	0.813	0.847	-2.016	0.687	1.926	0.476	0.328	0.360	0.828	0.310	3.753	0.505	3.332	0.665	2.496	0.247
	3.712	0.540	2.208	0.279	2.499	0.292	-0.027	0.019	0.020	0.023	-0.502	0.008	-0.079	0.012	0.878	0.040	0.286			-0.078		
IC1153	0.933	0.027	0.942	0.028	1.031	0.032	1.040	0.032	1.025	0.022	1.004	0.021	0.842	0.018	1.124	0.028	1.166	0.122	1.185	0.069	1.004	0.021
	0.376	0.040	0.467	0.031	0.378	0.027	-1.902	0.236	-6.439	0.192	0.530	0.133	-1.557	0.100	1.227	0.087	5.348	0.141	5.532	0.185	1.837	0.069
	3.700	0.150	3.696	0.078	2.941	0.081	0.086	0.008	0.125	0.010	-0.461	0.004	0.020	0.005	1.047	0.027	0.499			-0.083		
IC1211	0.980	0.051	1.012	0.053	1.065	0.060	1.091	0.059	0.972	0.041	1.061	0.040	0.870	0.033	1.155	0.052	1.212	0.227	1.167	0.129	1.004	0.038
	0.440	0.123	0.564	0.097	0.483	0.085	-2.089	0.750	-5.680	0.608	0.560	0.421	-1.278	0.318	1.354	0.275	5.617	0.447	5.038	0.589	1.974	0.219
	5.293	0.478	4.360	0.247	3.316	0.258	0.065	0.017	0.105	0.020	0.464	0.007	0.456	0.010	1.039	0.050	0.232			0.039		
M32	0.903	0.004	0.926	0.004	0.996	0.005	1.021	0.005	0.951	0.004	1.011	0.003	0.868	0.003	1.106	0.004	1.155	0.020	0.972	0.011	1.012	0.003
	0.296	0.011	0.474	0.009	0.550	0.007	-0.895	0.091	-4.618	0.074	0.993	0.051	-0.634	0.038	1.196	0.033	5.141	0.054	4.944	0.071	2.242	0.026

Table 3—Continued

Galaxy ID	$\frac{H\delta^a}{\lambda 4045}$	$\frac{H\delta}{\lambda 4063}$	$\frac{SrII\lambda 4077}{\lambda 4045}$	$\frac{SrII\lambda 4077}{\lambda 4063}$	$\frac{H\gamma^a}{\lambda 4325}$	$\frac{\lambda 4289}{\lambda 4271}$	$\frac{\lambda 4384}{\lambda 4352}$	p[Fe/H]	Ca II	$\frac{\lambda 3888^a}{\lambda 3859}$	$\frac{p4220}{p4209}$											
	EW(Fe)	EW(Ca)	EW(H γ)	H δ_A	H γ_A	H δ_F	H γ_F	Ca4227	G4300	Fe4383 ^b	H $\beta^{a,b}$											
	Fe5015	Mg b^b	Fe5270 ^b	CN1	CN2	Mg ₁ ^b	Mg ₂ ^b	Hn/Fe ^a	$\Delta H\beta_{emiss}^c$	$\Delta H\beta_{NSAR}^d$												
NGC183	5.039	0.058	2.814	0.030	2.923	0.031	0.024	0.002	0.061	0.003	0.001	0.001	0.169	0.001	0.942	0.004	0.000	-0.012				
	0.961	0.016	0.989	0.017	1.002	0.020	1.025	0.019	1.003	0.013	1.016	0.013	0.894	0.011	1.105	0.017	1.188	0.074	1.157	0.042	1.031	0.013
	0.246	0.032	0.446	0.026	0.312	0.023	-2.018	0.234	-5.880	0.190	0.407	0.132	-1.625	0.100	1.322	0.086	5.502	0.140	4.646	0.184	1.777	0.068
NGC205	4.483	0.149	3.847	0.077	2.881	0.081	0.074	0.008	0.111	0.010	-0.114	0.004	0.170	0.005	1.040	0.016	0.185	-0.030				
	0.623	0.004	0.624	0.004	0.957	0.005	0.956	0.005	0.719	0.003	0.981	0.003	1.161	0.003	0.978	0.004	0.659	0.018	0.573	0.010	0.989	0.003
	0.139	0.053	0.166	0.042	0.863	0.037	6.548	0.167	4.481	0.135	4.954	0.094	4.272	0.071	0.472	0.061	1.201	0.099	0.819	0.131	4.304	0.049
NGC448	2.272	0.106	1.314	0.055	1.235	0.057	-0.141	0.004	-0.076	0.005	0.313	0.002	0.197	0.002	0.638	0.004	0.059	0.041				
	0.988	0.017	0.994	0.018	1.037	0.020	1.044	0.020	0.988	0.014	1.025	0.013	0.860	0.011	1.127	0.017	1.259	0.075	1.074	0.043	1.002	0.013
	0.331	0.054	0.500	0.043	0.465	0.038	-1.949	0.399	-5.736	0.324	0.486	0.224	-1.522	0.169	1.201	0.146	5.505	0.237	4.903	0.313	1.851	0.116
NGC474	5.045	0.254	2.929	0.132	2.462	0.137	0.042	0.017	0.078	0.021	-0.307	0.007	0.047	0.010	1.016	0.017	0.000	-0.056				
	0.939	0.014	0.958	0.014	1.014	0.016	1.029	0.016	0.991	0.011	1.018	0.011	0.857	0.009	1.115	0.014	1.176	0.062	1.118	0.035	1.004	0.010
	0.349	0.035	0.554	0.028	0.438	0.024	-2.018	0.277	-5.783	0.225	0.579	0.156	-1.539	0.118	1.294	0.102	5.479	0.165	5.021	0.218	1.846	0.081
NGC502	4.831	0.177	3.746	0.091	2.980	0.096	0.080	0.014	0.122	0.017	-0.216	0.006	0.120	0.008	1.016	0.014	0.149	-0.048				
	0.946	0.004	0.972	0.004	1.028	0.005	1.057	0.005	1.007	0.003	1.026	0.003	0.859	0.003	1.132	0.004	1.082	0.019	1.137	0.011	1.010	0.003
	0.329	0.010	0.514	0.008	0.466	0.007	-2.104	0.079	-5.994	0.064	0.511	0.044	-1.592	0.033	1.436	0.029	5.461	0.047	5.335	0.062	1.786	0.023
NGC516	5.316	0.050	3.895	0.026	3.054	0.027	0.060	0.002	0.099	0.003	0.021	0.001	0.223	0.001	1.030	0.004	0.000	-0.014				
	0.878	0.015	0.884	0.015	1.010	0.018	1.018	0.017	0.909	0.012	0.965	0.012	0.877	0.010	1.070	0.015	1.093	0.067	0.897	0.038	0.979	0.011
	0.265	0.041	0.346	0.032	0.502	0.029	0.320	0.374	-4.163	0.303	1.552	0.210	-0.207	0.159	0.961	0.137	5.055	0.223	4.557	0.294	2.252	0.109
NGC525	4.461	0.238	2.227	0.123	2.319	0.129	-0.024	0.010	0.014	0.011	-0.396	0.004	-0.059	0.006	0.895	0.015	0.000	-0.059				
	0.944	0.020	0.955	0.021	1.029	0.023	1.039	0.023	0.973	0.016	1.007	0.015	0.887	0.013	1.106	0.020	1.130	0.089	1.012	0.051	0.976	0.015
	0.321	0.056	0.508	0.045	0.459	0.039	-1.294	0.277	-5.298	0.225	0.741	0.156	-1.211	0.118	1.266	0.102	5.432	0.165	4.522	0.218	1.944	0.081
NGC584	4.662	0.177	3.172	0.091	2.674	0.096	0.009	0.011	0.049	0.014	-0.102	0.005	0.135	0.007	0.976	0.020	0.072	-0.026				
	0.935	0.013	0.976	0.014	0.987	0.015	1.030	0.015	0.993	0.010	1.021	0.010	0.870	0.008	1.133	0.013	1.138	0.058	1.144	0.033	1.012	0.010
	0.283	0.038	0.570	0.030	0.494	0.026	-2.034	0.178	-5.981	0.145	0.469	0.100	-1.547	0.076	1.356	0.065	5.626	0.106	5.275	0.140	1.791	0.052
NGC636	5.277	0.114	3.839	0.059	3.011	0.062	0.075	0.004	0.116	0.004	-0.161	0.002	0.142	0.002	1.024	0.013	0.000	-0.042				
	0.969	0.013	1.004	0.014	1.016	0.016	1.054	0.016	0.990	0.011	1.028	0.010	0.850	0.009	1.105	0.014	1.093	0.060	1.109	0.034	0.996	0.010
	0.323	0.030	0.575	0.023	0.519	0.021	-1.934	0.278	-5.762	0.226	0.451	0.156	-1.447	0.118	1.344	0.102	5.532	0.166	5.012	0.219	1.722	0.081
NGC656	5.391	0.177	3.924	0.092	3.060	0.096	0.072	0.008	0.108	0.009	-0.031	0.003	0.198	0.005	1.022	0.013	0.000	-0.023				
	0.939	0.016	0.959	0.016	1.010	0.019	1.031	0.018	1.004	0.013	1.012	0.012	0.871	0.010	1.106	0.016	1.124	0.070	1.053	0.040	1.016	0.012
	0.252	0.056	0.449	0.044	0.398	0.038	-1.837	0.335	-5.638	0.272	0.573	0.188	-1.456	0.142	1.217	0.123	5.424	0.200	5.210	0.263	1.851	0.098
NGC770	4.899	0.213	3.739	0.111	2.806	0.116	0.068	0.006	0.105	0.007	0.127	0.003	0.270	0.004	0.999	0.015	0.030	0.002				
	0.958	0.016	0.978	0.016	1.010	0.019	1.027	0.018	0.969	0.013	0.999	0.012	0.885	0.010	1.096	0.016	1.125	0.070	1.065	0.040	0.995	0.012
	0.243	0.052	0.425	0.041	0.392	0.036	-1.972	0.275	-5.260	0.223	0.382	0.154	-1.129	0.117	1.173	0.101	5.523	0.164	4.633	0.216	1.916	0.080
NGC774	4.742	0.175	3.254	0.091	2.704	0.095	0.036	0.010	0.069	0.011	-0.092	0.004	0.142	0.006	0.997	0.015	0.101	-0.023				
	0.965	0.020	0.974	0.021	1.043	0.023	1.047	0.023	0.989	0.016	1.041	0.015	0.886	0.013	1.121	0.020	1.256	0.088	1.118	0.050	1.014	0.015

Table 3—Continued

Galaxy ID	$\frac{H\delta^a}{\lambda 4045}$	$\frac{H\delta}{\lambda 4063}$	$\frac{SrII\lambda 4077}{\lambda 4045}$	$\frac{SrII\lambda 4077}{\lambda 4063}$	$\frac{H\gamma^a}{\lambda 4325}$	$\frac{\lambda 4289}{\lambda 4271}$	$\frac{\lambda 4384}{\lambda 4352}$	p[Fe/H]	Ca II	$\frac{\lambda 3888^a}{\lambda 3859}$	$\frac{p4220}{p4209}$											
	EW(Fe)	EW(Ca)	EW(H γ)	H δ_A	H γ_A	H δ_F	H γ_F	Ca4227	G4300	Fe4383 ^b	H $\beta^{a,b}$											
	Fe5015	Mg b^b	Fe5270 ^b	CN1	CN2	Mg1 ^b	Mg2 ^b	Hn/Fe ^a	$\Delta H\beta_{emiss}^c$	$\Delta H\beta_{NSAR}^d$												
NGC821	0.363	0.072	0.548	0.056	0.426	0.050	-1.708	0.287	-5.332	0.233	0.597	0.161	-1.440	0.122	1.242	0.105	5.273	0.171	4.439	0.225	1.743	0.084
	4.558	0.183	3.860	0.095	2.902	0.099	0.052	0.007	0.088	0.008	0.052	0.003	0.222	0.004	1.024	0.020	0.152		-0.008			
	0.970	0.008	1.006	0.008	1.004	0.009	1.042	0.009	1.022	0.006	1.044	0.006	0.859	0.005	1.124	0.008	1.187	0.036	1.221	0.020	1.018	0.006
	0.334	0.020	0.652	0.016	0.438	0.014	-2.815	0.131	-6.455	0.106	0.244	0.074	-1.815	0.056	1.416	0.048	5.641	0.078	5.544	0.103	1.702	0.038
NGC938	5.263	0.083	4.026	0.043	3.131	0.045	0.103	0.003	0.147	0.004	-0.214	0.001	0.138	0.002	1.071	0.008	0.000		-0.049			
	0.917	0.018	0.949	0.019	1.003	0.022	1.033	0.021	0.996	0.014	1.019	0.014	0.868	0.012	1.108	0.019	1.252	0.081	1.087	0.046	1.001	0.014
	0.327	0.048	0.487	0.038	0.423	0.033	-1.604	0.370	-5.221	0.301	0.653	0.208	-1.427	0.157	1.192	0.136	5.243	0.221	4.509	0.291	1.899	0.108
	4.803	0.236	3.523	0.122	2.856	0.128	0.065	0.008	0.104	0.009	-0.120	0.003	0.145	0.005	1.000	0.018	0.131		-0.033			
NGC990	0.951	0.011	0.972	0.011	1.005	0.013	1.026	0.013	0.998	0.009	1.016	0.009	0.880	0.007	1.098	0.011	1.208	0.049	1.129	0.028	1.007	0.008
	0.261	0.034	0.484	0.027	0.396	0.023	-1.987	0.203	-5.631	0.165	0.416	0.114	-1.571	0.086	1.269	0.075	5.551	0.121	4.839	0.160	1.858	0.059
	4.863	0.130	3.770	0.067	2.837	0.070	0.067	0.005	0.107	0.005	0.116	0.002	0.263	0.003	1.026	0.011	0.054		0.002			
	0.950	0.020	0.981	0.021	0.988	0.024	1.020	0.023	1.012	0.016	0.997	0.016	0.882	0.013	1.102	0.020	1.180	0.089	1.140	0.051	1.012	0.015
NGC1026	0.227	0.054	0.481	0.042	0.322	0.037	-2.125	0.266	-6.039	0.216	0.411	0.149	-1.676	0.113	1.232	0.097	5.526	0.159	4.996	0.209	1.476	0.078
	4.437	0.170	3.846	0.088	2.899	0.092	0.092	0.010	0.136	0.012	-0.253	0.004	0.126	0.006	1.034	0.020	0.019		-0.054			
	0.974	0.014	1.006	0.015	1.023	0.017	1.056	0.017	1.016	0.012	1.023	0.011	0.850	0.009	1.108	0.015	1.187	0.065	1.146	0.037	1.024	0.011
	0.305	0.045	0.563	0.036	0.372	0.032	-2.477	0.243	-6.524	0.197	0.148	0.137	-1.937	0.103	1.319	0.089	5.444	0.145	5.526	0.191	1.425	0.071
NGC1107	4.835	0.155	4.011	0.080	3.074	0.084	0.093	0.005	0.128	0.006	-0.364	0.002	0.032	0.003	1.045	0.014	0.136		-0.064			
	0.949	0.022	0.998	0.023	0.974	0.026	1.020	0.026	1.030	0.018	1.009	0.017	0.851	0.014	1.116	0.022	1.183	0.098	1.163	0.056	0.999	0.017
	0.154	0.069	0.531	0.054	0.309	0.048	-2.580	0.342	-7.279	0.278	-0.057	0.192	-2.382	0.145	1.383	0.125	6.073	0.204	5.331	0.269	1.502	0.100
	5.064	0.218	4.026	0.113	3.030	0.118	0.102	0.015	0.137	0.018	-0.171	0.007	0.155	0.009	1.048	0.022	0.120		-0.042			
NGC1153	0.966	0.022	1.017	0.023	0.991	0.026	1.044	0.025	1.046	0.017	1.016	0.017	0.850	0.014	1.060	0.022	1.259	0.097	1.174	0.055	1.028	0.016
	0.349	0.048	0.459	0.038	0.326	0.033	-2.770	0.255	-6.748	0.207	-0.199	0.143	-2.189	0.108	1.470	0.094	5.891	0.152	5.684	0.200	1.206	0.074
	4.960	0.163	4.019	0.084	3.022	0.088	0.125	0.007	0.175	0.008	-0.400	0.003	0.073	0.004	1.062	0.021	0.153		-0.078			
	0.912	0.011	0.942	0.012	0.997	0.013	1.030	0.013	0.975	0.009	0.996	0.009	0.869	0.007	1.108	0.012	1.116	0.051	1.031	0.029	1.019	0.009
NGC1211	0.215	0.036	0.436	0.029	0.431	0.025	-0.835	0.184	-4.995	0.149	1.082	0.103	-0.988	0.078	1.178	0.067	4.837	0.109	4.939	0.144	2.080	0.054
	4.908	0.117	3.780	0.061	2.838	0.063	0.040	0.002	0.080	0.002	0.107	0.001	0.203	0.001	0.973	0.011	0.289		0.006			
	0.910	0.034	0.930	0.035	0.999	0.040	1.016	0.039	0.961	0.027	0.998	0.026	0.875	0.022	1.131	0.034	1.163	0.150	1.081	0.086	0.999	0.025
	0.245	0.065	0.519	0.052	0.501	0.045	-1.114	0.592	-5.124	0.480	0.849	0.332	-0.969	0.251	1.198	0.217	5.231	0.353	4.679	0.465	2.001	0.173
NGC1298	4.979	0.377	3.282	0.195	2.811	0.204	0.037	0.009	0.072	0.010	-0.184	0.004	0.085	0.005	0.984	0.033	0.119		-0.037			
	1.036	0.024	1.014	0.025	1.063	0.028	1.032	0.028	0.957	0.019	1.009	0.019	0.893	0.015	1.135	0.024	1.275	0.107	1.171	0.061	0.997	0.018
	0.549	0.066	0.540	0.052	0.344	0.046	-2.605	0.408	-5.957	0.331	0.362	0.229	-1.529	0.173	1.472	0.150	5.308	0.243	5.103	0.321	1.485	0.119
	4.473	0.260	3.747	0.135	2.800	0.141	0.071	0.012	0.113	0.014	-0.239	0.005	0.064	0.007	1.054	0.023	0.257		-0.043			
NGC2778	0.946	0.012	0.972	0.013	1.011	0.014	1.035	0.014	1.018	0.010	1.040	0.009	0.857	0.008	1.080	0.012	1.178	0.054	1.149	0.031	1.018	0.009
	0.351	0.019	0.554	0.015	0.416	0.013	-2.332	0.140	-6.201	0.113	0.278	0.079	-1.860	0.059	1.306	0.051	5.718	0.083	5.092	0.110	1.713	0.041
	4.927	0.089	4.003	0.046	3.120	0.048	0.092	0.002	0.140	0.003	-0.280	0.001	0.111	0.001	1.038	0.012	0.394		-0.061			

Table 3—Continued

Galaxy ID	$\frac{H\delta^a}{\lambda 4045}$		$\frac{H\delta}{\lambda 4063}$		$\frac{SrII\lambda 4077}{\lambda 4045}$		$\frac{SrII\lambda 4077}{\lambda 4063}$		$\frac{H\gamma^a}{\lambda 4325}$		$\frac{\lambda 4289}{\lambda 4271}$	$\frac{\lambda 4384}{\lambda 4352}$	p[Fe/H]		Ca II	$\frac{\lambda 3888^a}{\lambda 3859}$	$\frac{p4220}{p4209}$					
	EW(Fe)		EW(Ca)		EW(H γ)		H δ_A		H γ_A		H δ_F	H γ_F	Ca4227	G4300	Fe4383 ^b	$\Delta H\beta_{emiss}^c$	$\Delta H\beta_{NSAR}^d$					
	Fe5015		Mg b^b		Fe5270 ^b		CN1		CN2		Mg ₁ ^b	Mg ₂ ^b	Hn/Fe ^a		$\Delta H\beta_{emiss}^c$	$\Delta H\beta_{NSAR}^d$						
NGC2880	0.902	0.009	0.936	0.009	0.998	0.010	1.033	0.010	0.994	0.007	1.013	0.007	0.870	0.006	1.103	0.009	1.179	0.039	1.105	0.022	1.022	0.007
	0.305	0.026	0.510	0.021	0.464	0.018	-1.392	0.173	-5.574	0.140	0.741	0.097	-1.357	0.073	1.296	0.063	5.609	0.103	4.781	0.136	1.985	0.051
	4.974	0.110	3.379	0.057	2.889	0.060	0.067	0.004	0.109	0.005	-0.275	0.002	0.078	0.002	1.001	0.009	0.024		-0.055			
NGC2918	0.956	0.024	1.000	0.025	1.029	0.028	1.070	0.028	0.962	0.019	1.015	0.019	0.829	0.015	1.118	0.024	1.139	0.107	1.142	0.061	0.995	0.018
	0.402	0.066	0.571	0.052	0.482	0.046	-1.981	0.408	-6.483	0.331	0.492	0.229	-1.558	0.173	1.226	0.150	5.517	0.243	6.355	0.321	1.680	0.119
	5.174	0.260	3.921	0.135	2.960	0.141	0.070	0.012	0.105	0.014	-0.044	0.005	0.183	0.007	1.020	0.023	0.195		-0.021			
NGC2950	0.920	0.004	0.963	0.004	1.000	0.004	1.042	0.004	0.991	0.003	1.022	0.003	0.862	0.002	1.127	0.004	1.198	0.017	1.148	0.010	1.031	0.003
	0.283	0.014	0.520	0.011	0.462	0.010	-1.722	0.106	-5.808	0.086	0.667	0.059	-1.381	0.045	1.122	0.039	5.415	0.063	5.220	0.083	2.183	0.031
	5.550	0.067	3.423	0.035	3.217	0.036	0.095	0.003	0.136	0.004	0.106	0.001	0.261	0.002	1.020	0.004	0.141		-0.004			
NGC2954	0.935	0.011	0.981	0.012	1.007	0.014	1.041	0.013	0.965	0.009	1.020	0.009	0.864	0.007	1.123	0.012	1.186	0.051	1.003	0.029	1.005	0.009
	0.319	0.016	0.499	0.013	0.420	0.012	-1.846	0.150	-5.906	0.122	0.575	0.084	-1.419	0.064	1.369	0.055	5.500	0.090	4.881	0.118	2.245	0.044
	5.061	0.096	3.419	0.050	3.272	0.052	0.065	0.005	0.102	0.006	-0.337	0.002	0.050	0.003	0.967	0.011	0.425		-0.062			
NGC3071	0.965	0.019	0.973	0.020	1.022	0.022	1.034	0.022	1.001	0.015	1.008	0.015	0.877	0.012	1.113	0.019	1.089	0.084	1.128	0.048	1.005	0.014
	0.269	0.053	0.499	0.042	0.420	0.037	-2.119	0.348	-6.249	0.282	0.541	0.196	-1.631	0.148	1.285	0.128	5.513	0.207	4.978	0.273	1.629	0.102
	4.379	0.222	3.730	0.115	2.823	0.120	0.069	0.006	0.111	0.007	-0.272	0.003	0.062	0.004	1.030	0.019	0.332		-0.048			
NGC3102	0.940	0.046	0.938	0.048	1.027	0.054	1.019	0.054	0.970	0.037	1.014	0.036	0.889	0.030	1.110	0.047	1.231	0.206	1.052	0.117	1.009	0.035
	0.330	0.069	0.612	0.055	0.523	0.048	-0.893	0.821	-5.162	0.666	1.068	0.461	-1.122	0.349	1.257	0.301	5.502	0.489	4.519	0.645	2.091	0.239
	4.749	0.523	3.783	0.271	2.842	0.283	0.045	0.025	0.090	0.030	-0.012	0.011	0.216	0.015	0.987	0.045	0.150		-0.023			
NGC3156	0.659	0.009	0.687	0.009	0.901	0.010	0.938	0.010	0.759	0.007	0.965	0.007	1.057	0.006	0.999	0.009	0.866	0.039	0.679	0.022	1.010	0.007
	0.093	0.040	0.203	0.032	0.866	0.028	4.889	0.260	2.380	0.211	3.768	0.146	3.264	0.110	0.663	0.095	1.982	0.155	2.093	0.204	4.146	0.076
	3.198	0.166	2.424	0.086	1.847	0.090	-0.088	0.004	-0.045	0.004	-0.056	0.002	0.082	0.002	0.699	0.009	0.717		-0.015			
NGC3193	0.970	0.009	0.993	0.009	1.020	0.010	1.039	0.010	1.023	0.007	1.034	0.007	0.858	0.006	1.126	0.009	1.202	0.039	1.133	0.022	1.010	0.007
	0.305	0.027	0.638	0.021	0.405	0.019	-2.400	0.105	-6.656	0.086	0.335	0.059	-1.865	0.045	1.410	0.039	5.619	0.063	5.329	0.083	1.632	0.031
	5.241	0.067	4.020	0.035	3.095	0.036	0.098	0.003	0.142	0.004	-0.136	0.001	0.167	0.002	1.042	0.009	0.184		-0.038			
NGC3248	0.890	0.008	0.920	0.008	0.983	0.009	1.011	0.009	0.958	0.006	1.022	0.006	0.869	0.005	1.107	0.008	1.152	0.035	1.018	0.020	1.005	0.006
	0.271	0.011	0.479	0.009	0.500	0.008	-0.846	0.099	-4.816	0.080	0.957	0.055	-0.835	0.042	1.311	0.036	4.980	0.059	4.822	0.078	2.322	0.029
	4.639	0.063	2.925	0.032	3.018	0.034	0.020	0.007	0.059	0.008	-0.316	0.003	0.047	0.004	0.956	0.008	0.146		-0.057			
NGC3266	0.969	0.009	0.986	0.010	1.010	0.011	1.028	0.011	1.002	0.007	1.006	0.007	0.889	0.006	1.112	0.009	1.145	0.041	1.058	0.023	1.002	0.007
	0.319	0.027	0.505	0.022	0.435	0.019	-1.889	0.100	-5.617	0.081	0.453	0.056	-1.498	0.043	1.268	0.037	5.611	0.060	4.586	0.079	1.668	0.029
	4.506	0.064	3.507	0.033	2.651	0.034	0.048	0.006	0.088	0.007	-0.010	0.003	0.191	0.004	1.010	0.009	0.000		-0.017			
NGC3489	0.819	0.003	0.850	0.003	0.976	0.004	1.012	0.004	0.884	0.002	0.992	0.002	0.934	0.002	1.071	0.003	1.070	0.014	0.868	0.008	0.994	0.002
	0.182	0.004	0.349	0.003	0.612	0.003	1.535	0.090	-2.203	0.073	2.096	0.051	0.749	0.038	1.030	0.033	4.320	0.054	3.971	0.071	2.839	0.026
	4.114	0.057	2.277	0.030	2.902	0.031	-0.015	0.002	0.030	0.002	-0.455	0.001	-0.049	0.001	0.857	0.003	0.385		-0.072			
NGC3524	0.943	0.009	0.941	0.010	1.032	0.011	1.030	0.011	0.951	0.007	1.004	0.007	0.884	0.006	1.077	0.009	1.157	0.041	0.969	0.024	0.988	0.007
	0.325	0.031	0.486	0.024	0.549	0.021	-0.716	0.211	-4.523	0.171	0.882	0.119	-0.602	0.090	1.313	0.077	5.121	0.126	4.396	0.166	2.201	0.062

Table 3—Continued

Galaxy ID	$\frac{H\delta^a}{\lambda 4045}$	$\frac{H\delta}{\lambda 4063}$	$\frac{SrII\lambda 4077}{\lambda 4045}$	$\frac{SrII\lambda 4077}{\lambda 4063}$	$\frac{H\gamma^a}{\lambda 4325}$	$\frac{\lambda 4289}{\lambda 4271}$	$\frac{\lambda 4384}{\lambda 4352}$	p[Fe/H]	Ca II	$\frac{\lambda 3888^a}{\lambda 3859}$	$\frac{p4220}{p4209}$											
	EW(Fe)	EW(Ca)	EW(H γ)	H δ_A	H γ_A	H δ_F	H γ_F	Ca4227	G4300	Fe4383 ^b	H $\beta^{a,b}$											
	Fe5015	Mg b^b	Fe5270 ^b	CN1	CN2	Mg ₁ ^b	Mg ₂ ^b	Hn/Fe ^a	$\Delta H\beta_{emiss}^c$	$\Delta H\beta_{NSAR}^d$												
NGC3599	4.637	0.134	2.844	0.070	2.874	0.073	0.009	0.006	0.041	0.007	0.275	0.002	0.285	0.003	0.954	0.009	0.000		0.026			
	0.823	0.011	0.849	0.012	0.970	0.014	1.000	0.013	0.889	0.009	1.005	0.009	0.916	0.007	1.058	0.012	0.975	0.051	0.886	0.029	1.005	0.009
	0.231	0.039	0.374	0.031	0.599	0.027	1.425	0.218	-2.106	0.177	2.028	0.123	0.745	0.093	1.003	0.080	3.849	0.130	4.037	0.171	3.117	0.064
NGC3648	4.620	0.139	2.290	0.072	3.066	0.075	-0.017	0.003	0.024	0.003	-0.388	0.001	-0.009	0.002	0.866	0.011	0.574		-0.067			
	0.987	0.009	1.011	0.009	1.015	0.011	1.040	0.011	1.042	0.007	1.039	0.007	0.863	0.006	1.111	0.009	1.185	0.041	1.172	0.023	1.015	0.007
	0.374	0.018	0.580	0.014	0.384	0.013	-2.858	0.127	-6.489	0.103	-0.038	0.071	-2.113	0.054	1.463	0.047	5.770	0.076	5.296	0.100	1.434	0.037
NGC3731	5.005	0.081	4.374	0.042	3.330	0.044	0.114	0.001	0.159	0.002	-0.195	0.001	0.162	0.001	1.067	0.009	0.253		-0.050			
	0.969	0.036	0.989	0.038	1.034	0.043	1.050	0.042	1.027	0.029	1.016	0.028	0.870	0.023	1.135	0.037	1.223	0.162	1.208	0.092	1.037	0.027
	0.312	0.124	0.552	0.098	0.397	0.086	-2.429	0.490	-6.098	0.398	0.350	0.275	-1.818	0.208	1.291	0.179	5.781	0.292	5.308	0.385	1.526	0.143
NGC3757	4.551	0.312	3.837	0.162	2.884	0.169	0.085	0.015	0.125	0.017	-0.232	0.006	0.140	0.009	1.068	0.036	0.169		-0.056			
	0.986	0.038	1.011	0.040	1.029	0.045	1.055	0.045	1.004	0.031	1.024	0.030	0.869	0.025	1.129	0.039	1.171	0.171	1.103	0.098	1.016	0.029
	0.360	0.127	0.542	0.100	0.478	0.088	-2.315	0.567	-5.950	0.460	0.364	0.318	-1.691	0.241	1.269	0.208	5.908	0.338	4.751	0.445	1.731	0.165
NGC3818	4.737	0.361	3.869	0.187	2.903	0.195	0.052	0.013	0.097	0.015	0.180	0.006	0.288	0.008	1.031	0.038	0.000		0.006			
	0.951	0.025	0.985	0.026	1.017	0.029	1.045	0.029	1.037	0.020	1.012	0.019	0.875	0.016	1.115	0.025	1.212	0.111	1.123	0.063	1.031	0.019
	0.303	0.082	0.656	0.065	0.386	0.057	-2.841	0.315	-6.480	0.256	0.117	0.177	-1.990	0.134	1.519	0.116	5.843	0.188	5.272	0.248	1.654	0.092
NGC4283	5.029	0.201	4.103	0.104	3.173	0.109	0.115	0.011	0.160	0.013	-0.323	0.005	0.099	0.007	1.037	0.024	0.238		-0.067			
	0.978	0.012	0.999	0.013	1.023	0.014	1.045	0.014	1.012	0.010	1.038	0.010	0.844	0.008	1.135	0.013	1.175	0.055	1.141	0.031	1.008	0.009
	0.368	0.026	0.621	0.021	0.476	0.018	-2.712	0.244	-6.546	0.198	0.316	0.137	-1.749	0.104	1.619	0.090	5.745	0.146	5.624	0.192	1.844	0.071
NGC4296	5.345	0.156	3.910	0.080	3.214	0.084	0.079	0.009	0.120	0.011	-0.033	0.004	0.221	0.005	1.043	0.012	0.000		-0.025			
	0.974	0.014	1.004	0.015	1.013	0.017	1.044	0.017	1.033	0.012	1.039	0.011	0.844	0.009	1.138	0.015	1.257	0.064	1.141	0.037	0.995	0.011
	0.297	0.034	0.551	0.027	0.407	0.024	-2.459	0.208	-6.237	0.169	0.376	0.117	-1.701	0.088	1.511	0.076	5.608	0.124	5.654	0.163	1.848	0.061
NGC4308	5.390	0.132	3.961	0.068	3.269	0.072	0.100	0.002	0.143	0.002	-0.270	0.001	0.113	0.001	1.049	0.014	0.300		-0.058			
	1.000	0.047	0.940	0.049	1.052	0.055	0.984	0.054	0.917	0.037	1.019	0.036	0.861	0.030	1.075	0.047	1.093	0.209	1.035	0.119	1.026	0.035
	0.297	0.131	0.454	0.104	0.588	0.091	-2.199	0.886	-5.059	0.719	0.777	0.498	-0.806	0.376	1.221	0.325	5.406	0.528	4.819	0.696	1.931	0.258
NGC4648	4.858	0.564	3.229	0.292	2.716	0.305	0.034	0.025	0.055	0.030	0.099	0.011	0.222	0.015	0.984	0.046	0.147		0.000			
	0.915	0.057	0.910	0.059	1.035	0.067	1.030	0.066	1.006	0.045	1.001	0.044	0.856	0.037	1.143	0.058	0.858	0.253	1.050	0.144	1.027	0.043
	0.436	0.185	0.602	0.146	0.517	0.128	-1.112	1.130	-5.822	0.917	1.365	0.635	-1.645	0.480	1.217	0.414	6.224	0.673	5.209	0.888	1.527	0.330
NGC5342	5.495	0.720	4.470	0.373	3.410	0.389	0.096	0.018	0.142	0.022	-0.022	0.008	0.251	0.011	0.990	0.056	0.000		-0.028			
	0.942	0.014	0.966	0.014	1.007	0.016	1.032	0.016	1.003	0.011	1.029	0.011	0.881	0.009	1.116	0.014	1.098	0.062	1.127	0.036	1.016	0.010
	0.351	0.043	0.623	0.034	0.472	0.030	-1.883	0.275	-5.928	0.223	0.537	0.154	-1.775	0.117	1.268	0.101	5.619	0.164	4.419	0.216	1.546	0.080
NGC5370	4.861	0.175	3.975	0.091	3.009	0.095	0.087	0.010	0.129	0.012	-0.207	0.004	0.135	0.006	1.024	0.014	0.000		-0.049			
	0.947	0.013	0.973	0.014	1.019	0.015	1.047	0.015	0.999	0.010	1.000	0.010	0.871	0.008	1.108	0.013	1.174	0.058	1.048	0.033	0.994	0.010
	0.251	0.047	0.417	0.037	0.393	0.032	-1.590	0.328	-5.666	0.266	0.606	0.184	-1.307	0.139	1.199	0.120	5.488	0.196	4.965	0.258	1.946	0.096
NGC5422	4.824	0.209	3.588	0.108	3.139	0.113	0.036	0.008	0.073	0.010	0.157	0.004	0.255	0.005	0.998	0.013	0.281		0.006			
	0.985	0.022	1.022	0.023	1.036	0.026	1.063	0.025	1.030	0.017	1.036	0.017	0.864	0.014	1.115	0.022	1.185	0.097	1.118	0.056	1.018	0.016

Table 3—Continued

Galaxy ID	$\frac{H\delta^a}{\lambda 4045}$ EW(Fe) Fe5015	$\frac{H\delta}{\lambda 4063}$ EW(Ca) Mg b^b	$\frac{SrII\lambda 4077}{\lambda 4045}$ EW(H γ) Fe5270 ^b	$\frac{SrII\lambda 4077}{\lambda 4063}$ H δ_A CN1	$\frac{H\gamma^a}{\lambda 4325}$ H γ_A CN2	$\frac{\lambda 4289}{\lambda 4271}$ H δ_F Mg ₁ ^b	$\frac{\lambda 4384}{\lambda 4352}$ H γ_F Mg ₂ ^b	p[Fe/H] Ca4227 Hn/Fe ^a	Ca II G4300 $\Delta H\beta_{emiss}^c$	$\frac{\lambda 3888^a}{\lambda 3859}$ Fe4383 ^b $\Delta H\beta_{NSAR}^d$	$\frac{p4220}{p4209}$ H $\beta^{a,b}$											
NGC5424	0.301	0.065	0.588	0.052	0.387	0.045	-2.486	0.397	-6.652	0.322	0.180	0.223	-1.942	0.169	1.441	0.145	5.536	0.236	5.495	0.312	1.680	0.116
	4.901	0.253	4.089	0.131	3.176	0.137	0.090	0.029	0.126	0.034	-0.163	0.013	0.175	0.017	1.045	0.022	0.310		-0.045			
	0.941	0.014	0.944	0.015	1.008	0.017	1.010	0.017	1.007	0.012	1.018	0.011	0.875	0.009	1.091	0.015	1.134	0.065	1.168	0.037	0.995	0.011
	0.334	0.046	0.521	0.036	0.334	0.032	-1.722	0.203	-5.718	0.165	0.431	0.114	-1.501	0.086	1.304	0.074	5.300	0.121	4.886	0.159	1.482	0.059
	4.696	0.129	3.813	0.067	2.859	0.070	0.073	0.005	0.112	0.006	-0.391	0.002	0.034	0.003	1.039	0.014	0.298		-0.071			
NGC5459	0.955	0.030	0.944	0.032	1.036	0.036	1.015	0.036	0.999	0.024	1.028	0.024	0.854	0.020	1.111	0.031	1.164	0.136	1.095	0.078	0.995	0.023
	0.344	0.060	0.559	0.047	0.397	0.041	-1.727	0.387	-6.226	0.314	0.685	0.218	-1.848	0.165	1.147	0.142	5.586	0.231	4.624	0.304	1.642	0.113
	4.601	0.247	3.659	0.128	2.779	0.133	0.069	0.010	0.116	0.012	-0.653	0.004	-0.067	0.006	1.017	0.030	0.281		-0.107			
NGC5481	0.962	0.011	0.968	0.011	1.026	0.013	1.032	0.013	1.008	0.009	1.012	0.009	0.882	0.007	1.083	0.011	1.153	0.049	1.073	0.028	1.002	0.008
	0.255	0.029	0.455	0.023	0.371	0.020	-1.556	0.192	-5.812	0.156	0.600	0.108	-1.455	0.082	1.124	0.070	5.426	0.115	4.894	0.151	1.512	0.056
	4.081	0.122	3.679	0.063	2.749	0.066	0.058	0.006	0.092	0.007	-0.190	0.003	0.082	0.004	1.014	0.011	0.183		-0.035			
NGC5500	0.906	0.024	0.892	0.025	1.031	0.029	1.014	0.028	0.988	0.019	0.996	0.019	0.870	0.016	1.087	0.025	1.136	0.108	0.943	0.062	1.012	0.018
	0.389	0.052	0.458	0.041	0.484	0.036	-1.146	0.465	-4.481	0.377	1.162	0.261	-0.841	0.198	1.224	0.170	4.788	0.277	4.054	0.365	1.824	0.136
	5.209	0.296	3.247	0.153	2.407	0.160	0.020	0.007	0.064	0.008	0.080	0.003	0.206	0.004	0.946	0.024	0.000		-0.002			
NGC5576	0.947	0.007	0.961	0.007	1.027	0.008	1.042	0.008	0.995	0.006	1.008	0.005	0.874	0.005	1.114	0.007	1.189	0.032	1.063	0.018	1.004	0.005
	0.301	0.010	0.543	0.008	0.468	0.007	-1.356	0.090	-5.652	0.073	0.746	0.051	-1.257	0.038	1.283	0.033	5.507	0.054	5.098	0.071	1.927	0.026
	5.285	0.057	3.453	0.030	2.834	0.031	0.050	0.002	0.088	0.002	-0.066	0.001	0.162	0.001	1.002	0.007	0.000		-0.024			
NGC5582	0.908	0.007	0.935	0.007	0.971	0.008	0.993	0.008	1.016	0.006	1.030	0.006	0.880	0.005	1.084	0.007	1.202	0.032	1.057	0.018	1.015	0.005
	0.297	0.054	0.577	0.043	0.454	0.037	-1.842	0.241	-6.229	0.195	0.459	0.135	-1.852	0.102	1.455	0.088	5.510	0.143	4.356	0.189	1.816	0.070
	5.491	0.153	3.791	0.079	2.995	0.083	0.081	0.001	0.125	0.002	-0.165	0.001	0.163	0.001	0.993	0.007	0.193		-0.043			
NGC5590	0.978	0.015	0.985	0.015	1.029	0.017	1.033	0.017	0.995	0.012	0.983	0.012	0.880	0.010	1.100	0.015	1.137	0.066	1.068	0.038	1.037	0.011
	0.335	0.057	0.550	0.045	0.430	0.040	-1.993	0.280	-5.425	0.227	0.563	0.157	-1.398	0.119	1.228	0.102	5.663	0.167	4.711	0.220	1.747	0.082
	4.589	0.178	3.865	0.092	3.022	0.096	0.068	0.004	0.109	0.005	0.121	0.002	0.241	0.003	1.013	0.014	0.109		-0.002			
NGC5596	0.944	0.027	0.957	0.028	1.009	0.032	1.023	0.031	1.002	0.021	1.083	0.021	0.870	0.017	1.111	0.027	1.153	0.120	0.984	0.068	1.008	0.020
	0.225	0.080	0.521	0.063	0.365	0.055	-1.263	0.425	-6.024	0.345	0.660	0.239	-1.271	0.181	1.329	0.156	4.838	0.253	5.558	0.334	1.666	0.124
	4.453	0.271	3.434	0.140	2.587	0.147	0.045	0.009	0.074	0.011	-0.240	0.004	0.063	0.005	0.976	0.026	0.333		-0.044			
NGC5603	0.913	0.022	0.921	0.023	1.015	0.026	1.024	0.026	0.989	0.018	0.975	0.017	0.846	0.014	1.122	0.023	1.123	0.100	1.108	0.057	1.030	0.017
	0.321	0.056	0.503	0.044	0.392	0.039	-1.562	0.318	-6.151	0.258	0.860	0.178	-1.357	0.135	1.188	0.116	5.289	0.189	5.725	0.250	1.854	0.093
	4.396	0.203	3.861	0.105	3.165	0.109	0.095	0.009	0.131	0.010	-0.204	0.004	0.136	0.005	1.003	0.022	0.469		-0.048			
NGC5611	0.892	0.006	0.912	0.006	0.994	0.007	1.016	0.007	0.978	0.005	1.014	0.004	0.883	0.004	1.092	0.006	1.163	0.026	1.064	0.015	1.001	0.004
	0.268	0.029	0.476	0.023	0.479	0.020	-0.797	0.115	-4.920	0.093	0.970	0.064	-1.015	0.049	1.084	0.042	5.341	0.068	4.542	0.090	1.842	0.034
	4.587	0.073	3.454	0.038	2.583	0.040	0.038	0.002	0.078	0.002	0.100	0.001	0.226	0.001	0.978	0.006	0.000		-0.002			
NGC5631	0.869	0.010	0.934	0.010	0.966	0.012	1.038	0.012	0.975	0.008	0.993	0.008	0.855	0.007	1.111	0.010	1.247	0.045	1.035	0.025	1.027	0.008
	0.276	0.021	0.518	0.017	0.478	0.015	-1.430	0.128	-5.912	0.104	0.844	0.072	-1.276	0.054	1.068	0.047	5.678	0.076	4.940	0.101	2.221	0.037
	5.636	0.082	3.389	0.042	3.260	0.044	0.073	0.002	0.114	0.002	-0.250	0.001	0.101	0.001	0.960	0.010	0.514		-0.052			

Table 3—Continued

Galaxy ID	$\frac{H\delta^a}{\lambda 4045}$		$\frac{H\delta}{\lambda 4063}$		$\frac{SrII\lambda 4077}{\lambda 4045}$		$\frac{SrII\lambda 4077}{\lambda 4063}$		$\frac{H\gamma^a}{\lambda 4325}$		$\frac{\lambda 4289}{\lambda 4271}$	$\frac{\lambda 4384}{\lambda 4352}$	p[Fe/H]	Ca II	$\frac{\lambda 3888^a}{\lambda 3859}$	$\frac{p4220}{p4209}$	$H\beta^{a,b}$					
	EW(Fe)		EW(Ca)		EW(H γ)		H δ_A		H γ_A		H δ_F		H γ_F	Ca4227	G4300	Fe4383 ^b						
	Fe5015		Mg b^b		Fe5270 ^b		CN1		CN2		Mg ₁ ^b		Mg ₂ ^b	Hn/Fe ^a	$\Delta H\beta_{emiss}^c$	$\Delta H\beta_{NSAR}^d$						
NGC5770	0.914	0.009	0.918	0.009	1.002	0.011	1.006	0.010	0.972	0.007	0.994	0.007	0.883	0.006	1.089	0.009	1.168	0.040	0.992	0.023	1.008	0.007
	0.292	0.039	0.469	0.031	0.479	0.027	-0.463	0.131	-4.879	0.106	1.153	0.074	-0.876	0.056	1.092	0.048	5.264	0.078	4.331	0.103	2.127	0.038
	5.022	0.084	2.762	0.043	2.721	0.045	0.017	0.004	0.050	0.005	-0.287	0.002	0.014	0.002	0.960	0.009	0.000		-0.046			
NGC5831	0.929	0.010	0.965	0.010	0.993	0.012	1.028	0.011	1.000	0.008	1.030	0.008	0.849	0.006	1.122	0.010	1.223	0.043	1.056	0.025	1.016	0.007
	0.330	0.041	0.552	0.033	0.472	0.029	-2.035	0.167	-6.111	0.135	0.469	0.094	-1.565	0.071	1.490	0.061	5.302	0.099	5.547	0.131	1.859	0.049
	5.321	0.106	3.764	0.055	3.066	0.057	0.077	0.002	0.120	0.003	-0.141	0.001	0.146	0.002	0.995	0.010	0.087		-0.038			
NGC5845	0.941	0.010	0.952	0.010	1.027	0.012	1.037	0.011	0.996	0.008	1.000	0.008	0.863	0.006	1.142	0.010	1.209	0.044	1.219	0.025	1.021	0.007
	0.381	0.026	0.598	0.021	0.506	0.018	-2.108	0.174	-6.407	0.141	0.436	0.098	-1.782	0.074	1.288	0.064	5.777	0.104	5.416	0.137	1.681	0.051
	5.091	0.111	3.981	0.057	3.088	0.060	0.097	0.006	0.137	0.007	-0.294	0.003	0.108	0.004	1.051	0.010	0.074		-0.064			
NGC5865	0.972	0.016	0.993	0.017	1.012	0.019	1.033	0.019	1.020	0.013	1.037	0.013	0.850	0.011	1.108	0.017	1.246	0.073	1.138	0.042	1.009	0.012
	0.329	0.027	0.587	0.022	0.460	0.019	-2.105	0.234	-6.774	0.190	0.531	0.131	-1.920	0.099	1.421	0.086	5.631	0.139	5.598	0.184	1.683	0.068
	5.600	0.149	4.030	0.077	3.127	0.081	0.081	0.009	0.120	0.011	-0.086	0.004	0.183	0.005	1.044	0.016	0.034		-0.030			
NGC5966	0.902	0.018	1.000	0.018	0.994	0.021	1.065	0.020	0.963	0.014	1.073	0.014	0.861	0.011	1.132	0.018	0.945	0.078	1.127	0.045	1.002	0.013
	0.444	0.049	0.736	0.039	0.479	0.034	-3.094	0.313	-6.678	0.254	0.256	0.176	-1.859	0.133	1.451	0.115	5.746	0.186	5.200	0.246	2.256	0.091
	4.083	0.199	2.717	0.103	2.881	0.108	0.098	0.008	0.150	0.009	-0.730	0.003	-0.112	0.005	0.997	0.017	0.902		-0.118			
NGC6003	0.947	0.018	0.982	0.019	1.020	0.022	1.056	0.021	0.981	0.015	1.031	0.014	0.858	0.012	1.126	0.019	1.098	0.082	1.085	0.047	1.014	0.014
	0.292	0.073	0.567	0.057	0.470	0.050	-2.418	0.267	-6.077	0.217	0.688	0.150	-1.416	0.113	1.277	0.098	5.475	0.159	5.279	0.210	1.866	0.078
	5.335	0.170	3.336	0.088	2.730	0.092	0.102	0.015	0.141	0.018	-0.265	0.007	0.057	0.009	1.005	0.018	0.085		-0.049			
NGC6017	0.932	0.019	0.956	0.020	0.996	0.022	1.021	0.022	0.942	0.015	0.962	0.015	0.895	0.012	1.079	0.019	0.970	0.084	0.998	0.048	1.007	0.014
	0.295	0.036	0.422	0.028	0.482	0.025	-0.776	0.371	-3.888	0.301	0.860	0.208	-0.643	0.158	1.096	0.136	5.484	0.221	4.226	0.292	2.282	0.108
	4.195	0.236	2.997	0.122	3.053	0.128	0.020	0.012	0.061	0.014	-0.268	0.005	0.052	0.007	0.957	0.019	0.475		-0.050			
NGC6030	0.980	0.030	1.004	0.031	1.012	0.035	1.034	0.035	1.001	0.024	1.076	0.023	0.876	0.019	1.110	0.030	1.159	0.133	1.099	0.076	0.999	0.023
	0.386	0.120	0.576	0.095	0.476	0.083	-2.559	0.482	-5.773	0.391	0.463	0.271	-1.429	0.205	1.519	0.177	4.692	0.287	5.433	0.379	1.625	0.141
	5.026	0.307	3.572	0.159	2.697	0.166	0.102	0.008	0.137	0.009	-0.272	0.003	0.104	0.005	1.026	0.029	0.107		-0.057			
NGC6126	0.952	0.023	0.996	0.024	1.014	0.027	1.060	0.026	1.006	0.018	1.014	0.018	0.833	0.015	1.106	0.023	1.460	0.102	1.176	0.058	1.003	0.017
	0.367	0.068	0.502	0.054	0.474	0.047	-2.566	0.500	-6.413	0.406	0.386	0.281	-1.885	0.212	1.252	0.183	5.750	0.298	5.378	0.393	1.694	0.146
	5.121	0.319	4.482	0.165	3.516	0.172	0.085	0.025	0.125	0.030	0.044	0.011	0.231	0.015	1.045	0.022	0.000		-0.009			
NGC7280	0.872	0.006	0.898	0.006	0.979	0.007	1.009	0.007	0.940	0.005	0.993	0.005	0.895	0.004	1.062	0.006	1.142	0.027	1.017	0.015	1.013	0.005
	0.230	0.028	0.296	0.022	0.452	0.020	-0.091	0.195	-4.160	0.159	1.185	0.110	-0.433	0.083	1.029	0.072	5.201	0.116	4.538	0.153	2.318	0.057
	4.829	0.124	2.610	0.064	2.852	0.067	0.019	0.008	0.066	0.010	-0.236	0.004	0.066	0.005	0.943	0.006	0.204		-0.045			
NGC7391	0.949	0.019	0.975	0.019	0.988	0.022	1.015	0.022	1.032	0.015	1.015	0.015	0.886	0.012	1.081	0.019	1.140	0.084	1.183	0.048	1.013	0.014
	0.196	0.047	0.412	0.038	0.279	0.033	-2.297	0.221	-6.345	0.179	0.140	0.124	-1.920	0.094	1.294	0.081	5.766	0.132	5.216	0.174	1.507	0.064
	5.153	0.141	4.119	0.073	3.143	0.076	0.117	0.007	0.165	0.009	-0.319	0.003	0.108	0.004	1.055	0.018	0.216		-0.062			
NGC7454	0.909	0.017	0.920	0.018	0.993	0.020	1.006	0.020	0.955	0.014	1.011	0.014	0.883	0.011	1.121	0.018	1.115	0.077	1.030	0.044	1.001	0.013
	0.278	0.048	0.442	0.038	0.538	0.033	-0.791	0.236	-4.368	0.192	0.941	0.133	-0.637	0.101	1.180	0.087	4.878	0.141	4.606	0.186	2.013	0.069

Table 3—Continued

Galaxy ID	$\frac{H\delta^a}{\lambda 4045}$	$\frac{H\delta}{\lambda 4063}$	$\frac{SrII\lambda 4077}{\lambda 4045}$	$\frac{SrII\lambda 4077}{\lambda 4063}$	$\frac{H\gamma^a}{\lambda 4325}$	$\frac{\lambda 4289}{\lambda 4271}$	$\frac{\lambda 4384}{\lambda 4352}$	p[Fe/H]	Ca II	$\frac{\lambda 3888^a}{\lambda 3859}$	$\frac{p4220}{p4209}$											
	EW(Fe)	EW(Ca)	EW(H γ)	H δ_A	H γ_A	H δ_F	H γ_F	Ca4227	G4300	Fe4383 ^b	H $\beta^{a,b}$											
	Fe5015	Mg b^b	Fe5270 ^b	CN1	CN2	Mg ₁ ^b	Mg ₂ ^b	Hn/Fe ^a	$\Delta H\beta_{emiss}^c$	$\Delta H\beta_{NSAR}^d$												
NGC7461	4.371	0.151	2.816	0.078	2.515	0.082	0.026	0.006	0.065	0.007	-0.389	0.002	-0.005	0.003	0.965	0.017	0.000	-0.066				
	0.971	0.018	0.973	0.018	1.024	0.021	1.027	0.021	1.014	0.014	1.015	0.014	0.860	0.012	1.122	0.018	1.149	0.079	1.084	0.045	1.022	0.013
	0.340	0.032	0.571	0.025	0.436	0.022	-2.503	0.354	-6.136	0.288	0.358	0.199	-1.924	0.150	1.322	0.130	5.622	0.211	5.038	0.278	1.431	0.103
NGC7557	4.876	0.226	3.920	0.117	2.949	0.122	0.087	0.005	0.133	0.006	-0.380	0.002	0.021	0.003	1.023	0.017	0.000	-0.065				
	0.870	0.015	0.877	0.015	1.021	0.017	1.025	0.017	0.902	0.012	0.999	0.011	0.885	0.009	1.044	0.015	1.091	0.065	0.816	0.037	0.995	0.011
	0.262	0.046	0.395	0.037	0.557	0.032	0.994	0.291	-3.314	0.236	1.850	0.163	0.029	0.123	1.237	0.106	4.253	0.173	4.257	0.228	2.298	0.085
NGC7611	5.481	0.185	2.284	0.096	2.420	0.100	-0.029	0.009	0.008	0.010	-0.312	0.004	0.002	0.005	0.863	0.014	0.090	-0.050				
	0.891	0.010	0.923	0.010	0.991	0.011	1.024	0.011	0.969	0.008	1.035	0.007	0.868	0.006	1.118	0.010	0.980	0.043	1.007	0.025	1.022	0.007
	0.256	0.036	0.490	0.028	0.489	0.025	-0.955	0.206	-4.759	0.167	1.133	0.116	-0.948	0.087	1.225	0.075	4.863	0.123	5.058	0.162	2.078	0.060
NGC7612	5.430	0.131	3.892	0.068	2.919	0.071	0.067	0.006	0.108	0.007	-0.067	0.002	0.153	0.003	0.956	0.009	0.051	-0.021				
	0.952	0.023	0.964	0.024	1.020	0.027	1.033	0.027	0.987	0.019	1.033	0.018	0.856	0.015	1.135	0.024	1.213	0.104	1.035	0.059	0.998	0.018
	0.297	0.041	0.536	0.033	0.454	0.029	-1.915	0.200	-5.941	0.162	0.809	0.112	-1.467	0.085	1.254	0.073	5.429	0.119	5.611	0.157	1.628	0.058
NGC7623	5.364	0.128	3.863	0.066	2.958	0.069	0.062	0.005	0.098	0.006	-0.200	0.002	0.090	0.003	0.991	0.023	0.027	-0.039				
	0.949	0.009	0.971	0.009	1.007	0.011	1.029	0.010	1.010	0.007	1.028	0.007	0.860	0.006	1.114	0.009	1.146	0.040	1.083	0.023	1.020	0.007
	0.315	0.040	0.554	0.032	0.415	0.028	-2.384	0.174	-6.198	0.141	0.348	0.098	-1.758	0.074	1.407	0.064	5.565	0.104	5.316	0.137	1.669	0.051
NGC7628	5.168	0.111	3.960	0.057	2.972	0.060	0.083	0.006	0.124	0.007	-0.102	0.003	0.178	0.004	1.014	0.009	0.026	-0.033				
	0.945	0.016	0.938	0.016	1.020	0.019	1.013	0.018	0.982	0.013	1.006	0.012	0.864	0.010	1.127	0.016	1.189	0.070	1.071	0.040	1.020	0.012
	0.314	0.039	0.458	0.031	0.456	0.027	-1.639	0.278	-5.404	0.226	0.761	0.156	-1.267	0.118	1.258	0.102	5.337	0.166	4.939	0.219	2.130	0.081
NGC7698	4.915	0.177	3.753	0.092	2.812	0.096	0.056	0.005	0.095	0.006	-0.045	0.002	0.140	0.003	0.999	0.015	0.361	-0.015				
	0.951	0.016	0.969	0.016	1.015	0.019	1.033	0.018	0.996	0.013	1.002	0.012	0.884	0.010	1.106	0.016	1.144	0.070	1.128	0.040	1.008	0.012
	0.249	0.039	0.463	0.031	0.377	0.027	-1.884	0.463	-5.553	0.376	0.653	0.260	-1.369	0.197	1.280	0.170	5.379	0.276	4.930	0.364	1.947	0.135
NGC7703	4.618	0.295	3.557	0.153	3.018	0.160	0.078	0.009	0.118	0.011	-0.443	0.004	0.025	0.006	1.025	0.015	0.056	-0.075				
	0.902	0.019	0.922	0.020	0.988	0.023	1.009	0.022	0.954	0.015	1.018	0.015	0.882	0.012	1.071	0.019	1.089	0.085	0.993	0.049	1.001	0.014
	0.232	0.047	0.382	0.037	0.469	0.032	-0.586	0.380	-4.123	0.308	1.042	0.213	-0.506	0.161	1.174	0.139	4.875	0.226	4.682	0.298	1.927	0.111
NGC7707	4.777	0.242	3.227	0.125	2.698	0.131	0.018	0.010	0.065	0.012	0.089	0.004	0.212	0.006	0.950	0.019	0.040	0.000				
	0.927	0.018	0.976	0.018	0.973	0.021	1.011	0.021	1.004	0.014	1.026	0.014	0.900	0.012	1.126	0.018	1.259	0.079	1.184	0.045	1.016	0.013
	0.187	0.045	0.535	0.035	0.382	0.031	-2.260	0.351	-5.660	0.285	0.320	0.197	-1.636	0.149	1.305	0.129	5.682	0.209	4.515	0.276	1.793	0.102
NGC7711	4.534	0.224	3.825	0.116	2.998	0.121	0.102	0.011	0.143	0.013	-0.283	0.005	0.089	0.007	1.038	0.018	0.392	-0.058				
	0.927	0.012	0.959	0.012	0.999	0.014	1.032	0.014	0.994	0.010	1.007	0.009	0.887	0.008	1.084	0.012	1.135	0.054	1.052	0.031	1.014	0.009
	0.213	0.031	0.381	0.024	0.374	0.021	-1.484	0.259	-5.302	0.210	0.513	0.145	-1.210	0.110	1.238	0.095	5.492	0.154	4.849	0.203	1.963	0.075
UGC06604	4.697	0.165	3.530	0.085	3.096	0.089	0.059	0.006	0.100	0.007	-0.231	0.003	0.112	0.004	0.991	0.012	0.196	-0.046				
	0.942	0.024	0.972	0.025	1.014	0.029	1.028	0.028	1.007	0.019	1.008	0.019	0.874	0.016	1.097	0.025	1.157	0.109	1.015	0.062	1.002	0.018
	0.287	0.069	0.514	0.054	0.342	0.048	-1.673	0.497	-5.863	0.403	0.398	0.279	-1.728	0.211	1.133	0.182	5.531	0.296	4.664	0.390	1.890	0.145
UGC0887	3.995	0.317	3.290	0.164	2.704	0.171	0.046	0.017	0.081	0.020	-0.044	0.007	0.171	0.010	0.988	0.024	0.471	-0.023				
	0.985	0.018	0.988	0.019	1.047	0.022	1.050	0.021	1.017	0.015	1.017	0.014	0.876	0.012	1.119	0.019	1.199	0.082	1.124	0.047	1.029	0.014

Table 3—Continued

Galaxy ID	$\frac{H\delta^a}{\lambda 4045}$	$\frac{H\delta}{\lambda 4063}$	$\frac{SrII\lambda 4077}{\lambda 4045}$	$\frac{SrII\lambda 4077}{\lambda 4063}$	$\frac{H\gamma^a}{\lambda 4325}$	$\frac{\lambda 4289}{\lambda 4271}$	$\frac{\lambda 4384}{\lambda 4352}$	p[Fe/H]	Ca II	$\frac{\lambda 3888^a}{\lambda 3859}$	$\frac{p4220}{p4209}$											
	EW(Fe)	EW(Ca)	EW(H γ)	H δ_A	H γ_A	H δ_F	H γ_F	Ca4227	G4300	Fe4383 ^b	H $\beta^{a,b}$											
	Fe5015	Mg b^b	Fe5270 ^b	CN1	CN2	Mg ₁ ^b	Mg ₂ ^b	Hn/Fe ^a	$\Delta H\beta_{emiss}^c$	$\Delta H\beta_{NSAR}^d$												
UGC12454	0.348	0.056	0.572	0.045	0.437	0.039	-2.436	0.289	-5.932	0.234	0.460	0.162	-1.748	0.123	1.300	0.106	5.851	0.172	4.617	0.227	1.567	0.084
	4.939	0.184	3.781	0.095	2.840	0.100	0.068	0.007	0.106	0.009	-0.124	0.003	0.176	0.004	1.042	0.018	0.000		-0.038			
	0.948	0.025	0.981	0.026	1.018	0.030	1.045	0.029	1.012	0.020	1.033	0.020	0.905	0.016	1.115	0.026	1.178	0.113	1.142	0.064	0.993	0.019
	0.336	0.082	0.480	0.064	0.285	0.056	-1.314	0.680	-4.456	0.552	0.655	0.382	-1.156	0.289	1.350	0.249	4.589	0.405	4.166	0.534	2.030	0.198
UGC12472	4.576	0.433	3.003	0.224	2.654	0.234	0.009	0.027	0.044	0.032	-0.386	0.012	-0.035	0.016	1.034	0.025	0.250		-0.058			
	0.629	0.009	0.641	0.009	0.961	0.010	0.978	0.010	0.760	0.007	0.982	0.007	1.075	0.006	1.007	0.009	0.693	0.039	0.646	0.022	1.006	0.007
	0.130	0.078	0.099	0.062	0.868	0.054	6.317	0.333	3.722	0.270	4.776	0.187	3.861	0.141	0.402	0.122	0.959	0.198	1.976	0.262	4.355	0.097
	2.828	0.212	2.112	0.110	1.846	0.115	-0.119	0.004	-0.081	0.005	-0.070	0.002	0.022	0.003	0.678	0.009	0.924		-0.007			
UGC9519	0.771	0.037	0.827	0.038	0.938	0.043	1.006	0.043	0.863	0.029	0.982	0.029	0.964	0.024	1.048	0.037	1.121	0.164	0.829	0.094	1.037	0.028
	0.101	0.113	0.267	0.090	0.709	0.079	2.453	0.507	-0.450	0.412	2.436	0.285	1.604	0.215	0.884	0.186	3.275	0.302	3.321	0.398	3.376	0.148
	4.449	0.323	1.849	0.167	2.499	0.175	-0.042	0.018	-0.002	0.022	-0.525	0.008	-0.097	0.011	0.821	0.036	0.457		-0.083			
	0.922	0.032	0.978	0.033	0.975	0.038	1.008	0.037	0.971	0.025	1.003	0.025	0.870	0.021	1.094	0.032	1.072	0.143	1.104	0.081	0.993	0.024
VCC049	0.192	0.054	0.553	0.043	0.444	0.037	-2.069	0.415	-5.651	0.337	0.390	0.233	-1.472	0.176	1.382	0.152	5.199	0.247	5.210	0.326	2.345	0.121
	5.484	0.264	3.169	0.137	3.237	0.143	0.067	0.013	0.097	0.016	-0.233	0.006	0.119	0.008	0.998	0.031	0.702		-0.055			
	0.903	0.019	0.890	0.020	1.028	0.023	1.014	0.022	0.916	0.015	0.968	0.015	0.907	0.012	1.082	0.019	1.178	0.085	0.853	0.049	1.024	0.014
	0.311	0.048	0.321	0.038	0.560	0.033	0.495	0.350	-3.206	0.284	1.562	0.197	0.134	0.149	0.958	0.128	4.338	0.209	3.417	0.275	2.389	0.102
VCC218	4.338	0.223	2.198	0.116	2.300	0.121	-0.037	0.004	0.009	0.004	-0.094	0.002	0.053	0.002	0.891	0.019	0.000		0.007			
	0.725	0.031	0.760	0.033	0.931	0.037	0.975	0.037	0.854	0.025	0.975	0.025	0.944	0.020	1.034	0.032	0.795	0.140	0.716	0.080	0.970	0.024
	-0.062	0.162	0.083	0.128	0.682	0.113	2.639	1.489	1.224	1.208	2.792	0.836	1.958	0.632	0.547	0.546	1.821	0.887	2.817	1.169	3.257	0.434
	2.969	0.949	1.449	0.491	1.512	0.513	-0.064	0.034	-0.017	0.040	-0.368	0.015	-0.057	0.020	0.765	0.031	0.632		-0.056			
VCC389	0.813	0.023	0.850	0.024	0.932	0.027	0.970	0.027	0.933	0.019	0.989	0.018	0.919	0.015	1.037	0.024	1.105	0.104	0.951	0.059	0.979	0.018
	0.111	0.082	0.315	0.064	0.485	0.056	1.208	0.569	-3.040	0.462	1.573	0.319	0.078	0.242	0.866	0.208	4.081	0.339	3.537	0.447	2.532	0.166
	4.167	0.363	2.206	0.188	2.566	0.196	-0.049	0.017	-0.025	0.020	-0.394	0.007	-0.038	0.010	0.898	0.023	0.124		-0.065			
	0.794	0.014	0.820	0.014	0.921	0.016	0.951	0.016	0.863	0.011	0.975	0.010	0.921	0.009	1.061	0.014	0.999	0.060	0.822	0.034	0.983	0.010
VCC523	0.188	0.077	0.359	0.061	0.630	0.053	1.747	0.383	-1.936	0.311	2.102	0.215	0.941	0.163	1.152	0.140	4.174	0.228	3.297	0.301	2.767	0.112
	5.251	0.244	2.065	0.126	2.641	0.132	-0.012	0.016	0.027	0.019	-0.409	0.007	-0.041	0.009	0.827	0.013	0.033		-0.066			
	0.833	0.057	0.842	0.059	1.042	0.067	1.046	0.066	0.942	0.045	1.065	0.045	0.994	0.037	1.071	0.058	1.156	0.255	0.875	0.145	0.966	0.043
	0.206	0.116	0.273	0.092	0.414	0.081	1.026	1.045	-2.955	0.848	1.591	0.587	-0.062	0.444	1.099	0.383	3.335	0.623	2.686	0.821	2.785	0.305
VCC634	3.481	0.666	1.931	0.345	2.283	0.360	-0.039	0.022	0.001	0.026	-0.219	0.010	0.040	0.013	0.883	0.056	0.199		-0.038			
	1.029	0.182	1.080	0.189	1.029	0.215	1.058	0.212	0.890	0.145	0.975	0.142	0.850	0.118	1.206	0.185	1.121	0.813	0.682	0.464	1.075	0.138
	-0.203	0.286	0.450	0.226	0.571	0.199	-3.252	2.869	-4.784	2.329	0.382	1.612	-1.276	1.219	1.035	1.052	4.785	1.710	3.333	2.254	3.395	0.837
	3.763	1.829	1.458	0.946	1.774	0.989	0.007	0.048	0.003	0.057	0.065	0.021	0.146	0.028	0.867	0.179	0.606		0.000			
VCC685	0.961	0.010	0.981	0.010	1.046	0.012	1.068	0.012	1.046	0.008	1.057	0.008	0.862	0.006	1.143	0.010	1.172	0.044	1.184	0.025	1.024	0.007
	0.396	0.016	0.697	0.013	0.462	0.011	-2.741	0.155	-6.324	0.126	0.379	0.087	-1.891	0.066	1.508	0.057	5.574	0.093	5.572	0.122	1.436	0.045
	5.679	0.099	4.404	0.051	3.348	0.054	0.125	0.003	0.171	0.003	-0.213	0.001	0.174	0.002	1.064	0.010	0.000		-0.055			

Table 3—Continued

Galaxy ID	$\frac{H\delta^a}{\lambda 4045}$		$\frac{H\delta}{\lambda 4063}$		$\frac{SrII\lambda 4077}{\lambda 4045}$		$\frac{SrII\lambda 4077}{\lambda 4063}$		$\frac{H\gamma^a}{\lambda 4325}$		$\frac{\lambda 4289}{\lambda 4271}$	$\frac{\lambda 4384}{\lambda 4352}$	p[Fe/H]		Ca II		$\frac{\lambda 3888^a}{\lambda 3859}$	$\frac{p4220}{p4209}$				
	EW(Fe)		EW(Ca)		EW(H γ)		H δ_A		H γ_A		H δ_F	H γ_F	Ca4227	G4300	Fe4383 ^b							
	Fe5015	Mg b^b			Fe5270 ^b		CN1		CN2		Mg ₁ ^b	Mg ₂ ^b	Hn/Fe ^a	$\Delta H\beta_{emiss}^c$	$\Delta H\beta_{NSAR}^d$							
VCC698	0.924	0.034	0.931	0.036	0.991	0.040	0.997	0.040	0.952	0.027	0.992	0.027	0.880	0.022	1.088	0.035	1.168	0.153	0.973	0.087	1.000	0.026
	0.228	0.072	0.412	0.056	0.416	0.050	-0.725	0.459	-4.948	0.373	0.923	0.258	-0.805	0.195	1.356	0.168	5.035	0.273	4.517	0.361	2.182	0.134
	4.826	0.292	2.915	0.151	2.933	0.158	-0.003	0.024	0.028	0.029	-0.083	0.011	0.150	0.014	0.949	0.034	0.081		-0.027			
VCC751	0.889	0.048	0.872	0.050	1.026	0.057	1.006	0.056	0.991	0.038	1.058	0.038	0.854	0.031	0.992	0.049	1.197	0.214	0.835	0.122	0.985	0.036
	0.415	0.128	0.459	0.101	0.532	0.089	0.140	0.803	-4.969	0.651	1.393	0.451	-0.964	0.341	1.138	0.294	4.170	0.478	4.375	0.631	2.224	0.234
	4.249	0.512	2.379	0.265	2.579	0.277	-0.024	0.019	0.007	0.022	0.067	0.008	0.189	0.011	0.905	0.047	0.000		0.000			
VCC758	0.909	0.081	0.939	0.084	1.020	0.096	1.054	0.095	0.991	0.065	0.971	0.064	0.879	0.053	0.989	0.083	1.248	0.364	1.075	0.207	1.009	0.062
	0.237	0.242	0.377	0.191	0.423	0.168	-0.146	2.084	-5.021	1.691	1.686	1.171	-1.082	0.885	1.416	0.764	5.150	1.242	4.554	1.637	2.305	0.608
	4.255	1.328	3.120	0.687	3.158	0.718	-0.004	0.044	0.031	0.052	-0.383	0.019	0.030	0.026	0.992	0.080	1.031		-0.067			
VCC781	0.838	0.044	0.827	0.045	0.965	0.052	0.952	0.051	0.785	0.035	1.008	0.034	1.084	0.029	0.962	0.045	0.863	0.196	0.494	0.112	1.012	0.033
	0.244	0.188	0.286	0.149	0.769	0.131	3.670	1.077	2.457	0.874	2.886	0.605	2.846	0.458	1.029	0.395	1.941	0.642	0.700	0.846	3.513	0.314
	2.133	0.687	1.785	0.355	2.352	0.371	-0.108	0.028	-0.070	0.033	0.032	0.012	0.089	0.016	0.706	0.043	0.647		0.000			
VCC784	0.908	0.010	0.941	0.010	1.004	0.012	1.034	0.011	1.033	0.008	1.030	0.008	0.878	0.006	1.069	0.010	1.136	0.044	1.153	0.025	1.020	0.007
	0.321	0.029	0.567	0.023	0.394	0.020	-1.413	0.215	-6.535	0.174	0.514	0.121	-2.202	0.091	1.337	0.079	5.648	0.128	4.377	0.169	1.725	0.063
	4.587	0.137	3.322	0.071	2.517	0.074	0.057	0.007	0.098	0.008	-0.177	0.003	0.138	0.004	1.032	0.010	0.189		-0.062			
VCC828	0.966	0.022	0.988	0.023	1.038	0.026	1.059	0.026	1.000	0.018	1.020	0.017	0.875	0.014	1.137	0.022	1.200	0.098	1.086	0.056	1.001	0.017
	0.311	0.038	0.556	0.030	0.449	0.026	-1.908	0.308	-5.605	0.250	0.664	0.173	-1.458	0.131	1.401	0.113	5.470	0.184	4.385	0.242	1.695	0.090
	4.922	0.196	3.738	0.102	2.816	0.106	0.031	0.007	0.066	0.008	-0.016	0.003	0.196	0.004	1.017	0.022	0.075		-0.047			
VCC856	0.947	0.077	1.017	0.080	1.092	0.091	1.172	0.090	0.813	0.062	0.986	0.060	1.042	0.050	1.243	0.079	1.270	0.346	0.844	0.197	0.992	0.058
	0.093	0.215	0.441	0.170	0.647	0.149	-0.276	1.356	-0.016	1.100	1.144	0.762	2.202	0.576	1.204	0.497	3.360	0.808	2.874	1.065	1.370	0.396
	3.904	0.864	1.578	0.447	1.595	0.467	-0.020	0.031	0.029	0.036	-0.254	0.013	0.009	0.018	0.868	0.076	0.000		-0.046			
VCC929	0.897	0.052	0.891	0.054	0.995	0.061	0.989	0.060	0.964	0.041	0.996	0.041	0.914	0.034	1.053	0.053	1.341	0.232	0.972	0.132	1.024	0.039
	0.198	0.122	0.466	0.096	0.450	0.085	0.253	0.938	-3.935	0.761	1.460	0.526	-0.440	0.398	1.096	0.344	4.380	0.559	3.954	0.736	1.576	0.273
	3.983	0.597	2.812	0.309	2.101	0.323	-0.023	0.013	-0.004	0.015	-0.020	0.006	0.170	0.008	0.944	0.051	0.000		-0.017			
VCC944	0.977	0.015	1.022	0.015	1.023	0.018	1.070	0.017	1.011	0.012	1.027	0.012	0.870	0.010	1.131	0.015	1.163	0.067	1.116	0.038	1.015	0.011
	0.332	0.028	0.577	0.022	0.468	0.020	-2.191	0.179	-6.010	0.145	0.253	0.101	-1.628	0.076	1.372	0.066	5.704	0.107	5.125	0.140	1.628	0.052
	4.944	0.114	3.837	0.059	2.927	0.062	0.058	0.009	0.097	0.010	-0.035	0.004	0.202	0.005	1.034	0.015	0.000		-0.022			
VCC966	0.880	0.009	0.922	0.010	0.968	0.011	1.013	0.011	0.953	0.007	1.017	0.007	0.859	0.006	1.138	0.010	1.083	0.042	1.069	0.024	1.024	0.007
	0.242	0.018	0.490	0.014	0.566	0.012	-1.144	0.201	-4.860	0.163	1.082	0.113	-0.701	0.085	1.302	0.074	5.027	0.120	5.209	0.158	2.363	0.059
	5.658	0.128	3.062	0.066	3.163	0.069	0.047	0.006	0.086	0.007	-0.316	0.003	0.058	0.004	0.967	0.009	0.044		-0.058			
VCC1010	0.981	0.038	0.965	0.040	1.041	0.045	1.024	0.045	0.934	0.031	1.001	0.030	0.898	0.025	1.067	0.039	1.259	0.171	0.936	0.097	0.966	0.029
	0.322	0.066	0.401	0.052	0.554	0.045	-0.556	0.970	-3.985	0.787	1.043	0.544	-0.501	0.412	1.118	0.355	4.632	0.578	3.717	0.762	2.030	0.283
	4.984	0.618	2.888	0.320	2.563	0.334	-0.010	0.017	0.025	0.021	-0.059	0.007	0.106	0.010	0.950	0.038	0.000		-0.017			
VCC1025	0.932	0.019	0.951	0.020	1.008	0.023	1.028	0.023	1.008	0.015	1.030	0.015	0.868	0.013	1.118	0.020	1.123	0.087	1.045	0.049	1.024	0.015
	0.293	0.041	0.550	0.033	0.466	0.029	-1.472	0.266	-5.892	0.216	0.661	0.149	-1.589	0.113	1.377	0.098	5.405	0.159	4.807	0.209	1.784	0.078

Table 3—Continued

Galaxy ID	$\frac{H\delta^a}{\lambda 4045}$	$\frac{H\delta}{\lambda 4063}$	$\frac{SrII\lambda 4077}{\lambda 4045}$	$\frac{SrII\lambda 4077}{\lambda 4063}$	$\frac{H\gamma^a}{\lambda 4325}$	$\frac{\lambda 4289}{\lambda 4271}$	$\frac{\lambda 4384}{\lambda 4352}$	p[Fe/H]	Ca II	$\frac{\lambda 3888^a}{\lambda 3859}$	$\frac{p4220}{p4209}$											
	EW(Fe)	EW(Ca)	EW(H γ)	H δ_A	H γ_A	H δ_F	H γ_F	Ca4227	G4300	Fe4383 ^b	H $\beta^{a,b}$											
	Fe5015	Mg b^b	Fe5270 ^b	CN1	CN2	Mg ₁ ^b	Mg ₂ ^b	Hn/Fe ^a	$\Delta H\beta_{emiss}^c$	$\Delta H\beta_{NSAR}^d$												
VCC1030	5.269	0.170	3.742	0.088	2.796	0.092	0.056	0.005	0.095	0.006	-0.045	0.002	0.188	0.003	0.995	0.019	0.031	-0.023				
	0.924	0.009	0.939	0.009	1.023	0.011	1.035	0.010	0.991	0.007	1.027	0.007	0.885	0.006	1.127	0.009	1.065	0.040	1.019	0.023	1.020	0.007
	0.322	0.026	0.576	0.021	0.497	0.018	-0.831	0.179	-4.530	0.146	1.218	0.101	-0.844	0.076	1.270	0.066	4.883	0.107	4.973	0.141	1.832	0.052
VCC1036	5.059	0.114	3.823	0.059	3.015	0.062	0.046	0.003	0.086	0.003	-0.043	0.001	0.204	0.002	0.978	0.009	0.120	-0.025				
	0.900	0.038	0.924	0.040	1.011	0.045	1.038	0.044	0.894	0.030	0.967	0.030	0.913	0.025	1.094	0.039	1.161	0.170	0.924	0.097	0.996	0.029
	0.234	0.112	0.523	0.089	0.586	0.078	-0.143	0.488	-3.771	0.396	1.210	0.274	0.172	0.207	1.157	0.179	5.170	0.291	3.422	0.384	1.964	0.142
VCC1062	4.554	0.311	2.736	0.161	2.420	0.168	-0.014	0.022	0.016	0.026	0.084	0.010	0.173	0.013	0.906	0.038	0.020	0.004				
	0.983	0.009	1.000	0.010	1.029	0.011	1.047	0.011	1.041	0.007	1.053	0.007	0.858	0.006	1.135	0.009	1.174	0.041	1.202	0.024	1.034	0.007
	0.361	0.026	0.635	0.020	0.435	0.018	-2.837	0.101	-6.692	0.082	0.200	0.057	-2.034	0.043	1.498	0.037	5.685	0.060	5.549	0.079	1.254	0.029
VCC1073	5.312	0.064	4.323	0.033	3.297	0.035	0.125	0.004	0.170	0.005	-0.232	0.002	0.167	0.002	1.075	0.009	0.000	-0.058				
	0.957	0.126	0.971	0.131	0.950	0.149	0.957	0.147	1.050	0.101	0.862	0.099	0.904	0.082	1.046	0.128	0.967	0.564	0.816	0.322	0.900	0.095
	0.519	0.125	0.405	0.098	0.311	0.086	-2.405	2.129	-4.847	1.728	0.806	1.196	-0.552	0.904	1.482	0.780	5.408	1.269	4.313	1.673	2.219	0.621
VCC1125	5.544	1.357	3.096	0.702	3.068	0.734	0.045	0.031	0.059	0.037	0.162	0.013	0.272	0.018	0.941	0.124	0.221	0.004				
	0.951	0.042	0.970	0.043	1.039	0.049	1.061	0.049	0.976	0.033	1.007	0.033	0.862	0.027	1.117	0.043	1.138	0.187	1.012	0.107	0.985	0.032
	0.291	0.084	0.493	0.067	0.501	0.058	-1.430	0.567	-5.131	0.460	0.660	0.318	-1.010	0.241	1.356	0.208	5.359	0.338	4.856	0.445	1.786	0.165
VCC1146	4.566	0.361	3.592	0.187	2.699	0.195	0.017	0.010	0.049	0.012	0.197	0.004	0.267	0.006	0.980	0.041	0.000	0.014				
	0.945	0.013	0.965	0.014	1.020	0.015	1.040	0.015	0.996	0.010	1.020	0.010	0.890	0.009	1.107	0.013	1.217	0.058	1.058	0.033	1.023	0.010
	0.288	0.037	0.523	0.029	0.463	0.026	-1.490	0.308	-5.231	0.250	0.540	0.173	-1.197	0.131	1.373	0.113	5.191	0.183	4.298	0.242	1.661	0.090
VCC1178	4.727	0.196	3.467	0.101	2.614	0.106	0.048	0.007	0.080	0.008	-0.151	0.003	0.115	0.004	1.000	0.013	0.026	-0.033				
	0.946	0.020	0.964	0.021	0.996	0.024	1.016	0.023	1.010	0.016	1.014	0.016	0.875	0.013	1.103	0.020	1.069	0.089	1.168	0.051	1.015	0.015
	0.319	0.031	0.540	0.024	0.434	0.021	-1.947	0.306	-5.773	0.249	0.467	0.172	-1.456	0.130	1.235	0.112	5.521	0.183	4.653	0.241	1.534	0.089
VCC1183	5.182	0.195	3.560	0.101	2.653	0.106	0.074	0.026	0.115	0.031	-0.176	0.012	0.143	0.016	1.041	0.020	0.000	-0.044				
	0.871	0.043	0.905	0.045	0.972	0.051	1.006	0.050	0.959	0.034	0.962	0.034	0.907	0.028	1.104	0.044	1.375	0.193	0.851	0.110	0.996	0.033
	0.195	0.149	0.374	0.118	0.462	0.103	0.905	0.918	-3.054	0.745	1.397	0.516	0.067	0.390	0.818	0.337	4.430	0.547	3.100	0.721	2.549	0.268
VCC1199	4.513	0.585	2.148	0.303	2.478	0.317	-0.023	0.009	0.022	0.010	-0.062	0.004	0.103	0.005	0.893	0.042	0.098	-0.014				
	0.957	0.151	1.124	0.157	1.087	0.178	1.276	0.176	0.980	0.120	1.096	0.118	0.830	0.098	1.183	0.154	1.077	0.674	1.782	0.385	0.974	0.114
	0.378	0.306	0.598	0.242	0.549	0.212	-0.699	1.592	-6.912	1.292	0.238	0.894	-1.250	0.676	2.044	0.583	5.128	0.949	5.991	1.251	1.855	0.464
VCC1231	6.523	1.015	3.834	0.525	3.159	0.549	0.029	0.044	0.078	0.052	-0.197	0.019	0.153	0.026	1.240	0.149	0.000	-0.049				
	0.945	0.008	0.979	0.008	1.010	0.009	1.044	0.009	1.029	0.006	1.026	0.006	0.864	0.005	1.126	0.008	1.155	0.034	1.169	0.019	1.022	0.006
	0.332	0.027	0.593	0.021	0.477	0.019	-2.462	0.062	-6.694	0.051	0.244	0.035	-1.987	0.027	1.269	0.023	5.758	0.037	5.396	0.049	1.620	0.018
VCC1242	5.782	0.040	4.243	0.021	3.256	0.022	0.102	0.005	0.146	0.005	-0.009	0.002	0.271	0.003	1.048	0.007	0.056	-0.031				
	0.947	0.016	0.952	0.017	1.035	0.020	1.037	0.019	0.979	0.013	1.024	0.013	0.875	0.011	1.108	0.017	1.168	0.074	1.055	0.042	1.000	0.013
	0.323	0.046	0.546	0.036	0.488	0.032	-1.254	0.496	-5.178	0.403	0.946	0.279	-1.029	0.211	1.435	0.182	5.176	0.296	4.849	0.390	2.054	0.145
VCC1250	4.739	0.316	3.642	0.164	2.720	0.171	0.017	0.007	0.059	0.008	-0.155	0.003	0.113	0.004	0.994	0.016	0.085	-0.034				
	0.802	0.011	0.827	0.011	0.954	0.013	0.984	0.012	0.876	0.009	0.987	0.008	0.945	0.007	1.047	0.011	1.011	0.047	0.860	0.027	1.002	0.008

Table 3—Continued

Galaxy ID	$\frac{H\delta^a}{\lambda 4045}$	$\frac{H\delta}{\lambda 4063}$	$\frac{SrII\lambda 4077}{\lambda 4045}$	$\frac{SrII\lambda 4077}{\lambda 4063}$	$\frac{H\gamma^a}{\lambda 4325}$	$\frac{\lambda 4289}{\lambda 4271}$	$\frac{\lambda 4384}{\lambda 4352}$	p[Fe/H]	Ca II	$\frac{\lambda 3888^a}{\lambda 3859}$	$\frac{p4220}{p4209}$											
	EW(Fe)	EW(Ca)	EW(H γ)	H δ_A	H γ_A	H δ_F	H γ_F	Ca4227	G4300	Fe4383 ^b	H $\beta^{a,b}$											
	Fe5015	Mg δ^b	Fe5270 ^b	CN1	CN2	Mg1 ^b	Mg2 ^b	Hn/Fe ^a	$\Delta H\beta_{emiss}^c$	$\Delta H\beta_{NSAR}^d$												
VCC1279	0.204	0.045	0.347	0.036	0.600	0.032	1.530	0.252	-1.804	0.204	1.953	0.141	0.899	0.107	1.040	0.092	3.952	0.150	3.335	0.198	2.709	0.073
	4.592	0.161	2.115	0.083	2.542	0.087	-0.027	0.003	0.013	0.004	-0.296	0.001	0.005	0.002	0.846	0.010	0.725		-0.050			
	0.914	0.005	0.936	0.005	0.998	0.006	1.015	0.006	0.978	0.004	1.012	0.004	0.875	0.003	1.113	0.005	1.139	0.021	1.087	0.012	1.011	0.004
	0.316	0.021	0.553	0.016	0.452	0.014	-1.679	0.085	-5.630	0.069	0.611	0.048	-1.355	0.036	1.329	0.031	5.469	0.051	4.964	0.067	1.940	0.025
VCC1283	4.951	0.054	3.533	0.028	2.947	0.029	0.063	0.005	0.103	0.006	-0.347	0.002	0.061	0.003	0.993	0.005	0.221		-0.065			
	0.873	0.044	0.908	0.046	0.977	0.052	1.013	0.051	0.982	0.035	0.983	0.034	0.894	0.029	1.112	0.045	1.214	0.196	1.108	0.112	0.997	0.033
	0.111	0.096	0.525	0.076	0.486	0.066	-1.275	0.750	-4.524	0.609	1.055	0.421	-0.992	0.319	1.298	0.275	4.884	0.447	4.884	0.589	1.555	0.219
	4.692	0.478	3.497	0.248	2.620	0.259	0.024	0.017	0.064	0.021	0.235	0.007	0.282	0.010	0.987	0.043	0.097		0.019			
VCC1297	0.933	0.015	0.941	0.016	0.991	0.018	1.000	0.018	1.027	0.012	1.028	0.012	0.866	0.010	1.124	0.015	1.168	0.067	1.233	0.038	1.010	0.011
	0.352	0.044	0.612	0.035	0.419	0.031	-2.541	0.239	-6.270	0.194	0.380	0.134	-1.814	0.102	1.394	0.088	5.591	0.143	5.147	0.188	1.353	0.070
	5.279	0.153	3.958	0.079	2.975	0.082	0.134	0.009	0.183	0.011	-0.555	0.004	0.028	0.005	1.064	0.015	0.022		-0.104			
	0.970	0.016	0.999	0.017	1.019	0.019	1.049	0.019	0.970	0.013	1.040	0.013	0.857	0.011	1.115	0.017	1.206	0.073	1.067	0.042	0.988	0.012
VCC1303	0.395	0.024	0.575	0.019	0.521	0.017	-2.034	0.255	-6.783	0.207	0.278	0.143	-1.693	0.108	1.347	0.094	5.878	0.152	4.823	0.200	1.785	0.074
	5.752	0.163	3.958	0.084	3.133	0.088	0.053	0.009	0.090	0.011	0.082	0.004	0.259	0.005	1.002	0.016	0.000		-0.007			
	0.838	0.018	0.839	0.019	0.980	0.021	0.981	0.021	0.886	0.014	0.987	0.014	0.955	0.012	1.062	0.018	0.917	0.079	0.759	0.045	1.004	0.014
	0.176	0.064	0.423	0.051	0.642	0.045	1.613	0.599	-1.327	0.486	1.979	0.336	1.116	0.255	1.140	0.220	3.766	0.357	3.281	0.471	2.925	0.175
VCC1321	4.698	0.382	2.256	0.198	2.801	0.206	-0.033	0.009	-0.004	0.011	-0.330	0.004	-0.003	0.005	0.828	0.018	0.000		-0.055			
	0.889	0.008	0.928	0.009	1.005	0.010	1.046	0.010	0.926	0.007	1.032	0.007	0.872	0.005	1.111	0.009	1.126	0.037	1.028	0.021	1.016	0.006
	0.282	0.035	0.514	0.028	0.541	0.024	-0.720	0.389	-4.734	0.316	0.993	0.219	-0.608	0.165	1.124	0.143	5.072	0.232	4.223	0.306	2.211	0.114
	5.267	0.248	2.872	0.128	2.926	0.134	0.025	0.016	0.064	0.020	-0.136	0.007	0.128	0.010	0.948	0.008	0.105		-0.032			
VCC1422	0.863	0.031	0.866	0.031	0.952	0.035	0.953	0.034	0.900	0.024	0.965	0.023	0.917	0.019	1.064	0.030	1.122	0.233	0.900	0.080	0.982	0.022
	0.144	0.235	0.372	0.068	0.522	0.063	0.155	0.656	-3.387	0.511	1.069	0.382	-0.135	0.275	1.025	0.241	4.725	0.398	3.098	0.505	2.273	0.195
	4.018	0.434	2.251	0.207	2.306	0.232	0.127	0.018	0.012	0.022	-0.223	0.008	0.036	0.011	0.888	0.031	0.122		-0.082			
	0.814	0.040	0.811	0.042	0.965	0.048	0.963	0.047	0.914	0.032	0.996	0.032	0.925	0.026	1.095	0.041	1.084	0.181	0.899	0.103	0.976	0.031
VCC1440	0.200	0.114	0.414	0.090	0.509	0.079	0.162	0.472	-3.404	0.383	1.981	0.265	-0.247	0.200	1.550	0.173	4.900	0.281	2.914	0.371	1.676	0.138
	4.052	0.301	2.492	0.156	1.872	0.163	-0.003	0.025	0.046	0.030	0.079	0.011	0.151	0.015	0.875	0.040	0.000		0.004			
	0.916	0.010	0.934	0.011	1.006	0.012	1.021	0.012	0.964	0.008	1.001	0.008	0.884	0.007	1.091	0.011	1.185	0.046	1.044	0.026	0.997	0.008
	0.300	0.026	0.477	0.021	0.469	0.018	-1.329	0.176	-4.882	0.143	0.708	0.099	-1.093	0.075	1.147	0.064	5.350	0.105	4.183	0.138	1.931	0.051
VCC1479	4.248	0.112	2.948	0.058	2.538	0.060	0.030	0.004	0.065	0.005	-0.231	0.002	0.072	0.002	0.974	0.010	0.130		-0.044			
	0.932	0.032	0.942	0.033	1.047	0.038	1.034	0.038	0.878	0.026	1.029	0.025	0.905	0.021	1.113	0.033	1.075	0.144	1.008	0.082	0.994	0.024
	0.324	0.099	0.398	0.078	0.646	0.068	-0.909	0.923	-4.459	0.749	0.873	0.518	-0.431	0.392	1.043	0.338	5.177	0.550	4.357	0.725	3.041	0.269
	4.861	0.588	3.557	0.304	2.649	0.318	0.010	0.020	0.038	0.023	-0.610	0.009	-0.096	0.012	0.939	0.032	0.646		-0.098			
VCC1488	0.610	0.030	0.629	0.031	0.873	0.035	0.889	0.034	0.745	0.023	1.031	0.023	1.121	0.019	0.975	0.030	0.757	0.132	0.658	0.075	0.990	0.022
	0.143	0.121	0.286	0.096	0.831	0.084	6.129	0.931	2.943	0.756	4.402	0.523	3.559	0.396	0.767	0.341	1.129	0.555	0.806	0.731	3.974	0.272
	2.030	0.593	1.569	0.307	1.887	0.321	-0.118	0.016	-0.063	0.019	-0.410	0.007	-0.072	0.009	0.671	0.029	0.225		-0.061			

Table 3—Continued

Galaxy ID	$\frac{H\delta^a}{\lambda 4045}$		$\frac{H\delta}{\lambda 4063}$		$\frac{SrII\lambda 4077}{\lambda 4045}$		$\frac{SrII\lambda 4077}{\lambda 4063}$		$\frac{H\gamma^a}{\lambda 4325}$		$\frac{\lambda 4289}{\lambda 4271}$	$\frac{\lambda 4384}{\lambda 4352}$	p[Fe/H]		Ca II	$\frac{\lambda 3888^a}{\lambda 3859}$	$\frac{p4220}{p4209}$					
	EW(Fe)		EW(Ca)		EW(H γ)		H δ_A		H γ_A		H δ_F	H γ_F	Ca4227	G4300	Fe4383 ^b	$\Delta H\beta_{emiss}^c$	$\Delta H\beta_{NSAR}^d$					
	Fe5015		Mg b^b		Fe5270 ^b		CN1		CN2		Mg ₁ ^b	Mg ₂ ^b	Hn/Fe ^a									
VCC1521	0.930	0.027	0.943	0.028	1.016	0.032	1.030	0.032	0.968	0.022	1.011	0.021	0.886	0.018	1.073	0.027	1.084	0.121	0.960	0.069	0.997	0.020
	0.318	0.073	0.485	0.058	0.442	0.051	-1.036	0.352	-4.652	0.285	0.874	0.197	-0.821	0.149	1.246	0.129	5.017	0.209	4.348	0.276	1.862	0.102
	4.298	0.224	3.133	0.116	2.612	0.121	-0.001	0.008	0.029	0.010	0.064	0.004	0.199	0.005	0.952	0.027	0.047	-0.008				
VCC1537	0.958	0.008	0.959	0.008	1.032	0.009	1.033	0.009	0.975	0.006	1.012	0.006	0.878	0.005	1.108	0.008	1.169	0.035	1.030	0.020	1.001	0.006
	0.314	0.042	0.497	0.033	0.507	0.029	-1.320	0.184	-5.200	0.149	0.876	0.103	-1.042	0.078	1.201	0.067	5.514	0.109	4.762	0.144	1.940	0.054
	4.788	0.117	3.259	0.061	2.705	0.063	0.022	0.004	0.059	0.005	0.078	0.002	0.237	0.003	0.988	0.008	0.000	0.013				
VCC1545	0.964	0.108	0.900	0.113	1.067	0.128	0.997	0.127	0.941	0.087	0.961	0.085	0.871	0.071	1.051	0.111	1.907	0.485	0.778	0.277	0.981	0.082
	0.287	0.192	0.459	0.152	0.556	0.133	-1.686	1.115	-4.353	0.905	0.645	0.626	-0.913	0.474	1.400	0.409	4.617	0.665	4.176	0.876	1.808	0.325
	4.068	0.711	3.067	0.368	2.339	0.384	0.004	0.042	0.059	0.050	0.134	0.018	0.199	0.025	0.894	0.107	0.000	0.011				
VCC1614	0.772	0.021	0.789	0.022	0.951	0.025	0.971	0.025	0.822	0.017	0.982	0.016	1.031	0.014	1.011	0.022	0.854	0.094	0.728	0.054	0.983	0.016
	0.119	0.097	0.200	0.076	0.717	0.067	3.678	0.526	0.840	0.427	2.856	0.295	2.182	0.223	0.990	0.193	2.754	0.313	1.957	0.413	3.180	0.154
	3.588	0.335	1.701	0.174	1.944	0.181	-0.088	0.011	-0.045	0.014	-0.079	0.005	0.038	0.007	0.774	0.021	0.421	-0.010				
VCC1630	0.955	0.011	0.950	0.011	1.015	0.013	1.010	0.013	1.015	0.009	1.032	0.009	0.862	0.007	1.116	0.011	1.232	0.049	1.001	0.028	1.023	0.008
	0.366	0.032	0.591	0.025	0.456	0.022	-1.893	0.275	-5.769	0.223	0.582	0.154	-1.386	0.117	1.585	0.101	5.167	0.164	5.400	0.216	1.636	0.080
	5.462	0.175	3.659	0.090	2.770	0.095	0.051	0.007	0.093	0.008	-0.145	0.003	0.168	0.004	0.990	0.011	0.000	-0.042				
VCC1827	0.850	0.023	0.869	0.023	0.946	0.027	0.964	0.026	0.910	0.018	1.001	0.018	0.905	0.015	1.090	0.023	1.056	0.101	0.866	0.058	1.009	0.017
	0.176	0.078	0.387	0.062	0.579	0.054	0.329	0.505	-3.211	0.410	1.408	0.284	0.141	0.214	1.114	0.185	4.349	0.301	3.855	0.397	2.577	0.147
	5.187	0.322	2.342	0.167	2.781	0.174	-0.028	0.018	0.012	0.022	-0.259	0.008	0.033	0.011	0.876	0.022	0.086	-0.044				
VCC1871	0.921	0.043	0.888	0.045	1.038	0.052	0.993	0.051	0.981	0.035	1.045	0.034	0.810	0.028	1.096	0.044	1.278	0.195	1.102	0.111	1.001	0.033
	0.388	0.101	0.531	0.080	0.597	0.070	-1.607	0.415	-6.122	0.336	0.791	0.233	-1.630	0.176	1.415	0.152	4.903	0.247	5.130	0.326	2.101	0.121
	5.394	0.264	2.909	0.137	2.743	0.143	0.019	0.009	0.065	0.010	-0.104	0.004	0.157	0.005	1.001	0.043	0.232	-0.029				
VCC1903	0.935	0.012	0.988	0.013	1.003	0.015	1.060	0.014	1.016	0.010	1.032	0.010	0.867	0.008	1.166	0.013	1.126	0.055	1.265	0.032	1.039	0.009
	0.396	0.048	0.634	0.038	0.449	0.033	-2.876	0.144	-6.462	0.117	0.158	0.081	-1.892	0.061	1.434	0.053	5.590	0.086	5.132	0.113	1.548	0.042
	5.707	0.092	4.450	0.048	3.397	0.050	0.156	0.006	0.208	0.007	-0.290	0.003	0.157	0.004	1.072	0.012	0.003	-0.062				
VCC1912	0.738	0.018	0.749	0.019	0.956	0.022	0.970	0.022	0.789	0.015	0.984	0.014	1.047	0.012	1.023	0.019	0.965	0.082	0.659	0.047	0.988	0.014
	0.142	0.068	0.229	0.054	0.805	0.047	3.933	0.542	1.521	0.440	3.282	0.305	2.841	0.230	0.754	0.199	2.268	0.323	2.146	0.426	3.302	0.158
	3.721	0.345	1.534	0.179	1.820	0.187	-0.082	0.013	-0.041	0.015	-0.051	0.005	0.071	0.007	0.729	0.018	0.000	-0.010				
VCC1938	0.959	0.010	0.973	0.010	1.018	0.012	1.033	0.011	1.011	0.008	1.049	0.008	0.841	0.006	1.140	0.010	1.140	0.043	1.152	0.025	1.009	0.007
	0.363	0.035	0.580	0.027	0.502	0.024	-2.169	0.159	-5.887	0.129	0.461	0.090	-1.341	0.068	1.363	0.058	5.249	0.095	5.696	0.125	2.050	0.047
	5.787	0.101	4.130	0.052	3.143	0.055	0.087	0.004	0.127	0.005	-0.016	0.002	0.216	0.002	1.041	0.010	0.000	-0.019				
VCC1939	0.976	0.013	0.994	0.013	1.017	0.015	1.023	0.015	1.024	0.010	1.033	0.010	0.859	0.008	1.136	0.013	1.185	0.056	1.160	0.032	1.039	0.009
	0.336	0.057	0.573	0.045	0.383	0.040	-2.510	0.354	-6.516	0.287	0.315	0.199	-2.011	0.150	1.266	0.130	5.619	0.211	5.388	0.278	1.327	0.103
	5.286	0.225	4.259	0.117	3.239	0.122	0.115	0.008	0.161	0.010	-0.399	0.004	0.102	0.005	1.053	0.012	0.348	-0.082				
VCC2000	0.947	0.004	0.965	0.004	1.005	0.005	1.025	0.005	1.033	0.003	1.027	0.003	0.866	0.003	1.128	0.004	1.172	0.018	1.256	0.010	1.039	0.003
	0.315	0.010	0.613	0.008	0.424	0.007	-2.620	0.141	-6.561	0.115	0.327	0.079	-1.859	0.060	1.318	0.052	5.836	0.084	5.363	0.111	1.465	0.041

Table 3—Continued

Galaxy ID	$\frac{H\delta^a}{\lambda 4045}$		$\frac{H\delta}{\lambda 4063}$		$\frac{SrII\lambda 4077}{\lambda 4045}$		$\frac{SrII\lambda 4077}{\lambda 4063}$		$\frac{H\gamma^a}{\lambda 4325}$		$\frac{\lambda 4289}{\lambda 4271}$		$\frac{\lambda 4384}{\lambda 4352}$		p[Fe/H]		Ca II		$\frac{\lambda 3888^a}{\lambda 3859}$		$\frac{p4220}{p4209}$	
	EW(Fe)		EW(Ca)		EW(H γ)		H δ_A		H γ_A		H δ_F		H γ_F		Ca4227		G4300		Fe4383 ^b		H $\beta^{a,b}$	
	Fe5015		Mg b^b		Fe5270 ^b		CN1		CN2		Mg ₁ ^b		Mg ₂ ^b		Hn/Fe ^a		$\Delta H\beta_{emiss}^c$		$\Delta H\beta_{NSAR}^d$			
VCC2048	5.309	0.090	4.045	0.047	3.048	0.049	0.123	0.005	0.167	0.006	-0.266	0.002	0.120	0.003	1.079	0.004	0.000		-0.058			
	0.817	0.036	0.832	0.037	0.972	0.042	0.985	0.042	0.916	0.029	0.977	0.028	0.939	0.023	1.034	0.036	1.122	0.160	0.901	0.091	0.982	0.027
	0.186	0.105	0.385	0.083	0.526	0.073	0.589	0.608	-1.977	0.493	1.621	0.341	0.694	0.258	1.002	0.223	3.705	0.362	3.346	0.477	2.285	0.177
	4.175	0.387	1.891	0.200	1.910	0.209	-0.032	0.024	-0.001	0.029	0.081	0.011	0.144	0.014	0.878	0.035	0.103		0.006			

^aCorrected for emission^bCorrected for non-solar abundance ratios (NSAR)^cCorrection to the Lick H β index due to emission^dCorrection to the Lick H β index due to NSAR